RAPID COMPRESSION MACHINE MEASUREMENTS OF IGNITION DELAYS FOR PRIMARY REFERENCE FUELS

by

PYONGWAN PARK

S.M., Seoul National University
(1984)

S.B., Seoul National University
(1982)

SUBMITTED TO THE DEPARTMENT OF
MECHANICAL ENGINEERING
IN PARTIAL FULFILLMENT OF THE REQUIREMENTS
FOR THE DEGREE OF

DOCTOR OF PHILOSOPHY

at the

MASSACHUSETTS INSTITUTE OF TECHNOLOGY

April, 1990

Signature of Author____
Department of Mechanical Engineering
April 3, 1990

Certified by__
James C. Keck
hesis Supervisor

Accepted by_____
Ain A. Sonin
Chairperson, Department Graduate Committee

RAPID COMPRESSION MACHINE MEASUREMENTS OF IGNITION DELAYS FOR PRIMARY REFERENCE FUELS

by

PYONGWAN PARK

Submitted to the Department of Mechanical Engineering
on 3 April 1990 in Partial Fulfillment of the
Requirements for the Degree of Doctor of Philosophy

ABSTRACT

A rapid compression machine (RCM) for chemical kinetic studies has been developed. The design objectives of the machine were to obtain: 1) uniform well-defined core gas; 2) heat transfer reduction; 3) containment of vortex formed from the side wall boundary layer; 4) pre-reaction minimization; and, 5) minimum dynamic stress. A crevice volume on the piston head was incorporated to achieve the side wall vortex containment, and the basic dimensions of the machine were determined from the above design objectives.

Preliminary tests with inert gases were conducted to check the performance of the RCM and to determine its heat transfer characteristic. Gas pressure was recorded without much mechanical vibration, and the performance of the machine was repeatable. For the piston with the crevice, the measured post-compression pressure matched with the pressure calculated assuming flow is laminar and the pressure drop rate after compression was slower than that for the piston without the crevice, indicating that the gas condition in the test chamber for the piston with the crevice is consistent with the expectation based on laminar theory.

Hydrocarbon absorption into O-ring material and purging procedure were carefully studied to ensure repeatable and reliable ignition delay measurements. O-rings with the least absorptivity were selected for the test chamber, and the time to reach the absorption saturation was determined from the measured absorption process of the test chamber. The repeatability of ignition delay measurements was achieved by using a dummy O_2 run between measurement runs, and the measured ignition delays were repeatable within 5 % of each other.

Measurements of ignition delays for homogeneous primary reference fuel (PRF)/O_2/N_2/Ar mixture in the rapid compression machine have been made with five primary reference fuels (octane number 100, 90, 75, 50, and 0) at an equivalence ratio of 1, a diluent/oxygen ratio of 3.77, and two initial pressures of 500 torr and 1000 torr. Post-compression temperatures were varied by blending Ar and N_2 in different ratios. It was found that the ignition delays were not a linear function of the octane number of the fuel. Within the experimental range covered, the first-stage ignition delays decreased rapidly as the temperature increased, whereas the second-stage ignition delays stayed unchanged as the temperature increased. Comparison with existing data showed that the ignition delay measurements made in other RCM's should be carefully re-evaluated partially due to their high heat transfer characteristics and partially due to their improper mixture preparation procedures.

Thesis Supervisor : Professor James C. Keck
Title : Ford Professor of Engineering

ACKNOWLEDGEMENTS

There are many acknowledgements that go to many people, and too many to list all in here, which are all very important.

I would like first thank my advisor, Prof. James C. Keck, and my thesis committee members, Prof. John B. Heywood, Prof. Jack P. Longwell, and Dr. David P. Hoult. A special thank you to Prof. Keck for his excellent education and guidance. Working for him has been a great learning period and pleasure.

I need to thank several MIT staff members including Don Fitzgerald, Howard Lunn, Brian Corkum, and Pat Condon for their unprecedented help in the lab. Special mention goes to Don for his superb technical help.

Thanks also go to my colleagues at the Sloan Lab for the many helpful discussions which we have had and for not shutting their doors as often as they had the right to. What can I say that is fit to print about wonderful guys like Kwangmin Chun, Mark Sztenderowicz, Andy Gerrick, Rob Chang, Ray Stanten, Jim Cowart, and Evan Hurlburt? To all the people in the Sloan Lab whose names I have not mentioned, may your life prosperous.

Of course, a special thank you to my parents and parents-in-law for their never-ending support and encouragement. My aspirations have been possible because of them.

And most of all, I dedicate this work to my loving and patient wife, Sungwon, and my lovely son, Jongkyu, who make my life worthwhile. I love them very much.

Pyongwan Park
April 1990

The major part of this work was sponsored by the U.S. Department of Energy, the Office of Energy Utilization Research, the Energy Conversion and Utilization Technology Program under contract number DE-SG04-87AL44875.

TABLE OF CONTENTS

LIST OF TABLES

LIST OF FIGURES

Figure page

3.6 Comparison of Inert Gas Pressure Traces for Piston Head with and without Crevice : Initial Temperature=298 K, Crevice Volume=0.527 cm^3, Stroke=7.74 cm, Clearance Height=0.60 cm, Driving Pressure=2.07 MPa, Speed Control Orifice Area=6.81 cm^2, Time 0 Shifted to Steepest Slope 81

GAS : N2	W/O Crevice	W/ Crevice
Isentropic Pressure	(1)3.69 MPa	(2)3.53 MPa
Isothermal Pressure	(3)1.32 MPa	(4)1.27 MPa
Initial Pressure	(5)95 KPa	
Peak Pressure	3.16 MPa	3.10 MPa
Compression Ratio	13.9	13.4

(6) Isentropic Pressure assuming Laminar Boundary Layer for Piston without Crevice=3.56 MPa, (7) Isentropic Pressure assuming Isothermal Crevice for Piston with Crevice=3.22 MPa, (8) Isentropic Pressure assuming Isothermal Crevice and Laminar Boundary Layer for Piston with Crevice=3.11 MPa

3.7 Comparison of Measured Post-compression Pressure with Calculated Post-compression Pressure from Laminar Theory : Gas=N_2, Clearance Height=0.6 cm, Speed Control Orifice Area=6.81 cm^2 82

3.8 Raw Pressure and Filtered Pressure : FIR Optimal Low Pass Filter, Pass Band Cut-off Frequency=0.5 KHz, Stop Band Cut-off Frequency=1.0 KHz, Filter Length=51, Band Error=62.5 dB, Gas=N_2, P_I=720 torr, T_I=303 K, Driving Pressure=2.07 MPa, Stroke=7.84 cm, Clearance Height=0.6 cm, Speed Control Orifice Opening Area=6.81 cm^2, Piston Head with Crevice, Time 0 Shifted to Start of Compression 83

3.9 Thermal Displacement Thickness : Gas=N_2, P_I=720 torr, T_I=303 K, Driving Pressure=2.07 MPa, Stroke=7.84 cm, Clearance Height=0.6 cm, Speed Control Orifice Opening Area=6.81 cm^2, Piston Head with Crevice, α_o=2.253x10^{-5} m^2/s, Time 0 Shifted to Start of Compression 84

3.10 Piston Displacement Obtained from Heat Transfer Analysis : Gas=N_2, P_I=720 torr, T_I=303 K, Driving Pressure=2.07 MPa, Stroke=7.84 cm, Clearance Height=0.6 cm, Speed Control Orifice Opening Area=6.81 cm^2, Piston Head with Crevice, Time 0 Shifted to Start of Compression 85

CHAPTER 1

INTRODUCTION

Spark ignition engine knock is known to be a result of the autoignition of an adiabatically compressed portion of the unburned fuel-air mixture ahead of the advancing flame front [1,2,3] and obtaining an understanding of this process has been one of the major goals of combustion research [4,5]. In engine studies, primary reference fuels (blends of normal-heptane and iso-octane) are used to establish the octane rating scale, but only limited research on these fuels has been carried out under controlled conditions.

To isolate the autoignition process from the complex in-cylinder engine flow conditions, experimental investigators of knock have used various experimental apparatuses, such as a rapid compression machine, a shock tube, and a combustion bomb [1,6,7,8]. In such devices the autoignition of primary reference fuels has been observed to be either a single- or a two-stage event depending on the physical conditions and the fuel.

An excellent apparatus for observing the two-stage ignition event under engine like conditions is the rapid compression machine (RCM). Unfortunately data obtained in different rapid compression machines operating under similar conditions often disagree [6,7]. The probable reasons for this disagreement are the difficulty of determining the effective temperature of the gas in the presence of turbulent boundary layers and the side wall vortex rolled up by the piston [9], and the run-to-run interference of active species adsorbed on the test chamber walls from previous runs.

Since chemistry is very sensitive to the temperature, it is the highest temperature, which occurs in the adiabatic core gas, that controls the reaction rates

[1]. It is, therefore, important to have a well-defined core temperature region in this type of experiment. It is also important to have accurate pressure measurements since these are used to determine the core temperature. In some rapid compression machines pressure traces were so masked by mechanical vibrations that obtaining accurate pressure data from these traces was practically impossible [10].

To help solve these problems a new rapid compression machine has been developed in which heat transfer and vibration have been reduced to a minimum and the wall vortex has been captured in a crevice. The performance of the machine was tested with inert gases. Pressure traces were recorded with little mechanical vibration, and the performance of the machine was repeatable. The measured post-compression pressure agreed with the pressure calculated assuming flow is laminar and the cooling rate of the charge after compression was reduced, indicating that the corner vortex was successfully captured in the crevice.

Autoignition studies for primary reference fuels were conducted under carefully controlled conditions. The results were repeatable with the proper purging procedures described in Chapter 4. It was found that current measured ignition delays agreed with existing data qualitatively, but not quantitatively. The heat transfer characteristics of other rapid compression machines and the purging procedures used were carefully examined. Some of these rapid compression machines were found to have high heat transfer characteristics.

The current measurements of autoignition are believed to be the most accurate since low heat transfer characteristic and little mechanical vibration allowed accurate core temperature determination from the measured pressure trace, and the filling and purging procedures were carefully chosen for repeatability.

CHAPTER 2

DESIGN AND OPERATION OF RCM

2.1 Review of Previous RCM's

Recent RCM's were reviewed in Table 2.1 to determine the basic structure of the current RCM such as driving mechanism, stopping mechanism, test chamber bore, clearance height, and average piston speed. RCM's have been used mainly for the study of in-cylinder flow and auto-ignition process. These phenomena have been studied both from an engine and from a chemical standpoint, therefore RCM's can be divided into two classes as shown in the last column of Table 2.1: engine-biased and chemistry-biased. The former are designed to simulate the conditions inside the combustion chamber of an engine, and tends to follow engine practice in having constant, rather short stroke, test chamber with large surface/volume ratio, and rather low deceleration for the piston stopping. Such design is characterized by high heat transfer due to the high surface/volume ratio of the test chamber and flow conditions such as turbulence and a corner vortex. This high heat transfer characteristics makes engine-biased RCM's unsuitable for chemical studies. On the other hand, the latter are designed to study chemical kinetics of various fuels, and are characterized by low surface/volume ratio of the test chamber and usually by laminar flow condition to have a uniform well-defined core temperature region since chemistry is sensitive to temperature.

The most important design consideration was how to drive and stop the piston. In previous RCM's, the impact of a falling weight or a pneumatic driving by high pressure gas were used for the driving mechanism. The pneumatic driving system was chosen for the present machine since it gives a continuous driving force. The

stopping mechanisms used in previous RCM's were as follows along with typical decelerations of the piston:

1) plastic deformation of metal [11] $a \sim 10^6$ m/s^2

2) air cushion chamber [6] $a \sim 10^3$ m/s^2

3) hydraulic system

snubbing chamber [17] $a \sim 10^4$ m/s^2

hydraulic pin and groove [16] $a \sim 10^5$ m/s^2

The piston should be stopped as rapidly as possible without any damage to the RCM. An excellent choice is the hydraulic pin and groove system for the stopping mechanism.

Important parameters that affect heat transfer characteristic of an RCM were examined. Temperature variation due to sound waves induced by piston motion was obtained from the relation:

$$\frac{\Delta T}{T} = \frac{\gamma-1}{2\gamma}\frac{u_p^2}{RT} = \frac{\gamma-1}{2}Ma^2 \qquad (2.1)$$

$$= \frac{\gamma-1}{2\gamma}\frac{u_p^2}{RT_i CR^{\gamma-1}} = \frac{\gamma-1}{2\gamma}\frac{u_p^2}{RT_i(1+S/h)^{\gamma-1}}$$

where u_p is the piston speed, CR is the compression ration, S is the stroke, h is the clearance height, γ is the specific heat ratio, and Ma is Mach number.

The thermal boundary layer thickness δ_T for gas undergoing pressure change was investigated by J.C. Keck [22], and is proportional to the square root of characteristic heating time (see Appendix A.2 for the definition of the characteristic heating time):

$$\delta_T = \sqrt{\alpha \tau_{ch}} = \sqrt{\alpha h/(\gamma-1)u_p} \qquad (2.2)$$

where τ_{ch} is the characteristic heating time, and the thermal diffusivity, α, is typically $5x10^{-6}$ m^2/s at typical knock temperature and pressure. Measured and calculated cooling times are defined as the reciprocal of logarithmic pressure drop rate at the end of compression, and are given by the relations (A2.7) and (A2.8) in the Appendix A.2 respectively.

Using the elementary entrainment theory [23], the relation for the corner vortex diameter d_v was derived in Appendix A.1 and is given by:

$$d_v = 4 \kappa CR^{(-\gamma+1)/2}(CR^{1/2}-1) h \qquad (2.3)$$

where $\kappa = 0.1$ is a constant determined from experiments with water [9].

In Table 2.2, the numbers calculated from the relations (2.1), (2.2), (2.3), (A2.7), and (A2.8) are summarized for chemistry-biased RCM's [6,16,18,21]. It is observed that a machine with higher ratio of corner vortex diameter to bore has lower ratio of measured cooling time to calculated cooling time, signifying that corner vortex plays an important role in heat transfer. It is also observed that current machine has the longest measured cooling time among recent chemistry-biased RCM's. In the design of previous chemistry-biased RCM's, the corner vortex has not been explicitly taken into account. The bore to clearance height ratios of the previous RCM's test chambers were of the order of 1 [16], and for a compression ratio CR of 10 and a specific heat ration γ of 1.4, the following relation is obtained from (2.3):

$$2d_v/b \sim h/b \sim 1$$

which shows that the corner vortex filled the almost entire test chamber of previous RCM's. This raises a serious question about the existence of a uniform core gas in previous machines.

2.2 Ideal RCM

The fundamental objective of a rapid compression machine is to heat a test gas as rapidly as possible to high temperature and pressure with as little heat and mass loss as possible. In an ideal machine of this type the temperature T and pressure P of the test gas are related to the compression ratio CR = V_i/V and specific heat ratio $\gamma = C_p/C_v$ by the equations:

$$\ln CR = \int_{T_i}^{T} (1/(\gamma-1))\, d\ln T \qquad (2.4)$$

and

$$\ln P/P_i = \int_{T_i}^{T} (\gamma/(\gamma-1))\, d\ln T \qquad (2.5)$$

In the derivation of (2.4) and (2.5) it has been assumed that there is no heat or mass loss and the test gas obeys the ideal gas relation of state:

$$P\,V = (m_g/W_g)\,R\,T \qquad (2.6)$$

where R is the universal gas constant and V, m_g and W_g are the volume, mass and mean molecular weight of the test gas.

Typical plots of γ as a function of temperature for i-$C_8H_{18}/O_2/N_2$/Ar mixtures with various N_2/Ar ratios are shown in Fig. 2.1 [24,25]. Also shown are corresponding plots of the pressure ratio as a function of the compression ratio and the temperature as a function of the pressure ratio. It can be seen from these plots that to achieve temperature and pressure in the range of 700 to 1000 K and 10 to 100 atm of interest for the study of autoignition in automobile engines, a compression ratio CR higher than 10 is required for an initial temperature of 300 K and an initial pressure of 1 atm. This is the most basic requirement placed on the design of the present machine.

2.3 Design criteria of the current RCM

The most important design objective for a chemistry-biased RCM is to have a uniform well-defined core temperature region, because the reaction rate is highly sensitive to temperature[1]. To obtain the uniform well-defined core temperature region in the test chamber, heat transfer should be reduced and temperature should be uniform. It is also important that any pre-reaction during the compression should be minimized. Dynamic stress consideration is also an important part of the design in addition to the design criteria imposed by aerodynamics and thermodynamics since some of previous RCM's suffered from vibrational problem [10] as shown Fig. 2.2. Vibration should be minimized to determine core temperature accurately since it is calculated from the measured pressure trace. The following conditions were imposed as design criteria for the present machine:

1) heat transfer reduction;

2) corner vortex containment;

3) temperature uniformity;

4) pre-reaction minimization;

5) dynamic stress consideration.

Even though the corner vortex containment is a part of heat transfer reduction, it is addressed here separately since it has not been explicitly considered in the design of previous RCM's.

2.3.1) heat transfer reduction

To reduce heat transfer, a) the flow should be laminar; b) the thermal boundary layer thickness should be small compared to the clearance height; c) the laminar cooling time should be large compared to the typical ignition delay time of interest; and d) the ratio of laminar cooling to characteristic heating time should be as large as possible. enough. In a piston-cylinder machine of the type designed and

constructed, the laminar flow condition requires that the Reynolds number Re = $u_p S/\nu$ based on the stroke S and the piston speed u_p, be less than critical Reynolds number, $Re_{crit} = 2.5 \times 10^5$:

$$Re = \frac{u_p S}{\nu} = \frac{u_p (CR-1) h}{\nu} < Re_{crit} \qquad (2.7)$$

where the kinematic viscosity, ν, is typically 5×10^{-6} m^2/s at the end of compression. Under laminar condition, thermal boundary layer thickness for the gas subject to pressure change was investigated by J.C. Keck [22], and is proportional to the square root of characteristic heating time:

$$\delta_T = \sqrt{\alpha \tau_{ch}}$$

where τ_{ch} is the characteristic heating time defined as $(\gamma-1)u_p/h$ in Appendix A.2, and α is the thermal diffusivity of the gas, which is typically around 5×10^{-6} m^2/s. For a well-defined adiabatic core, the ratio of thermal boundary layer δ_T to clearance height h should be less than ~ 0.1:

$$h > 10\delta_T$$

$$u_p h > 100 \frac{\alpha}{\gamma-1} \qquad (2.8)$$

The order of the longest ignition delay time reported is typically 100 msec or less, therefore the laminar cooling time should be greater than 100 msec. For the present design purpose, it is chosen to be 1 sec. With the laminar cooling time defined as $h^2/4\alpha$ in Appendix A.2, the following relation is obtained:

$$\tau_{lc} \sim \frac{h^2}{4\alpha} > 1 sec \qquad (2.9)$$

Large ratio of laminar cooling to characteristic heating time is also necessary since the gas should cool down at a much slower rate than it was heated up. This ratio is chosen to be 1000 to ensure slow cooling.

$$\frac{\tau_{lc}}{\tau_{ch}} > 1000$$

$$\frac{h u_p (\gamma - 1)}{4\alpha} > 1000 \qquad (2.10)$$

2.3.2) corner vortex containment

The corner vortex is a vigorous rotational flow created by a moving piston (see Appendix A.1), and enhances heat transfer significantly. consequently. As shown earlier in Table 2.2, the corner vortex is responsible for high heat transfer characteristics of the earlier RCM's. One technique for dealing with the corner vortex is to introduce a crevice volume at the perimeter of the piston head in which it can be contained. The entrance to this crevice must be sufficiently wide to permit the boundary layer to enter and its cross-sectional area must be big enough that it engulfs all the boundary layer scraped by a moving piston. The upper bound of gas swallowed in the crevice is calculated in the following manner:

$$\frac{m_{ubs}}{m_i} = \frac{A_s \delta \rho_i}{V_i \rho_i} = \frac{4\pi b S \sqrt{\nu S / u_p} \rho_i}{\pi b^2 (h+S) \rho_i}$$

$$= 4 \frac{h}{b} \frac{(CR-1)^2}{CR} \sqrt{\frac{\nu}{u_p (CR-1) h}} \qquad (2.11)$$

where A_s is the cylinder wall area swept by the piston, δ is the boundary layer thickness, m_{ubs} is the upper bound of the mass swallowed in the crevice, and m_i is the total initial gas mass. Based on the above relation, the volume of the vortex containment crevice is calculated as follow assuming that the gas in the crevice is at wall temperature:

$$\frac{V_{cr}}{V_f} = \frac{V_{cr}}{V_i / CR} = CR \frac{m_{ubs}}{m_i} \frac{\rho_i}{\rho_v} = CR \frac{m_{ubs}}{m_i} \frac{P_i}{P_f}$$

$$\sim \frac{4(CR-1)^2}{CR^\gamma} \frac{h}{b} \sqrt{\frac{\nu}{u_p (CR-1) h}} \qquad (2.12)$$

where V_{cr} is the volume of the vortex containment crevice (or the piston head crevice volume) and ρ_v is the density of the gas in the crevice. The calculated vortex containment volume using (2.12) is 0.527 cm^3, and its detailed shape is shown in Fig. 2.3. The effect of the vortex containment volume on post-compression states can be estimated assuming isentropic compression of the core gas in the following manner:

$$P_f = P_i\left(\frac{\rho_f}{\rho_i}\right)^{\gamma} = P_i\left[\left(\frac{m_i - m_{ubs}}{\pi b^2 h/4}\right)/\left(\frac{m_i}{\pi b^2 CR\ h/4}\right)\right]^{\gamma}$$

$$= P_i CR^{\gamma}\left(1 - \frac{4h(CR-1)^2}{b\ CR}\sqrt{\frac{\nu}{u_p(CR-1)h}}\right)^{\gamma} \qquad (2.13)$$

$$T_f = T_i\left(\frac{\rho_f}{\rho_i}\right)^{\gamma-1}$$

$$= T_i CR^{\gamma-1}\left(1 - \frac{4h(CR-1)^2}{b\ CR}\sqrt{\frac{\nu}{u_p(CR-1)h}}\right)^{\gamma-1}$$

The above post-compression states should not be very different from what would be achieved if there were no crevice. Therefore, the quantity in the parentheses of (2.13) should be close to unity. If a number $\geq .98$ is chosen for the quantity in the parentheses of (2.13), the following relation is obtained:

$$\frac{4h(CR-1)^2}{b\ CR}\sqrt{\frac{\nu}{u_p(CR-1)h}} < 1/50$$

$$b > \frac{200h(CR-1)^{3/2}}{CR}\sqrt{\frac{\nu}{u_p h}} \qquad (2.14)$$

2.3.3) temperature uniformity

To obtain uniform temperature in the core temperature region, the temperature variation produced by sound waves induced by the piston motion should not be

high. An estimate of this variation is derived in (2.1) by assuming that the local velocity fluctuation is of the order of piston speed, and for $\Delta T < 1$ K and T ~ 1000 K, the following relation is obtained:

$$\frac{(\gamma-1)u_p^2}{\gamma RT} < 1/1000 \qquad (2.15)$$

2.3.4) pre-reaction minimization

The ideal RCM compresses gas instantaneously so that the step change in temperature and pressure can be achieved, whereas the real one takes a certain amount of time to compress gas. However, the real RCM can be made close to the ideal one by minimizing pre-reaction during the compression and by compressing the gas as rapidly as possible within the stress limitation of material. Characteristic pre-reaction time τ_{pr}, which is a measure how much reaction has taken place during the compression, is defined in Appendix A.2 as follows:

$$\tau_{pr} = I/R_f \sim \left(\frac{u_p}{a} + \frac{h}{(\gamma-1)\beta_f \theta u_p}\right) \qquad (A2.5)$$

where β_f is the reciprocal of absolute temperature at the end of compression, and θ is the activation energy. The above expression has the minimum value for given values of a and h when:

$$u_p = (ha/(\gamma-1)\beta_f\theta)^{1/2} \qquad (2.16)$$

where θ is around 10^4 K for the typical knock reaction.

2.3.5) dynamic stress consideration

To compress the gas, the piston is accelerated to a certain speed from rest and then is decelerated back to rest at the end of the compression. For the characteristic compression time (see Appendix A.2) of the order of 10 msec, the stress level in the

piston is high. The stress is the highest during the piston stopping because of the short mechanical stopping time (see Appendix A.2) of the order of 1 msec. The stress consideration in the plane (a) of Fig. 2.4 determines the length L as follows:

$$\rho\pi b^2 La/4 = \pi b^2 Y/4n$$

$$L = \frac{Y}{\rho an} \qquad (2.17)$$

where a is the piston deceleration, Y is the yield strength of material, ρ is the density of material, and n is the safety factor, which is taken to be 5 since the stress concentration factor at the corner is between 2 and 3. The length L should be long enough to have a compression ratio of 10, which was determined in the previous section. An excellent choice of material for the piston is an aluminum alloy since it has the highest Y/ρ ratio ($5x10^4$ m^2/s^2) among readily available materials. The shear stress consideration in the plane (b) of Fig. 2.4 also determines the length l as follows:

$$\rho\pi b^2 (L+l)a/4 = 4\pi b l \frac{Y}{2n}$$

$$l = \frac{b}{2} \frac{2Y/\rho anb}{2Y/\rho anb - 1} \qquad (2.18)$$

The piston is stopped by the oil pressure developed in the hydraulic pin and groove system, of which the stopping area is of the order of $3\pi b^2/4$ (see Fig. A.4 for details). Since this high oil pressure should not exceed the yield strength of material, the upper bound of the piston bore b is obtained from (2.17) and (2.18) as follows:

$$\rho(\pi b^2 L + 4\pi b^2 l)a/4 < \frac{3\pi b^2}{4} \frac{Y}{n}$$

$$b < \frac{4}{3} \frac{Y}{\rho an} \qquad (2.19)$$

2.3.6) operation and design map

Eight conditions (i.e. one equation 2.16 and seven inequalities 2.7, 2.8, 2.9, 2.10, 2.14, 2.15, and 2.19) have been found for the design criteria, and three important design parameters were identified; they are the piston speed u_p, the piston bore b, and the clearance height h. Eight design criteria form two important maps from which the design parameters of the current RCM is chosen: the operation map (u_p vs h map), and the design map (b vs h map).

The relations (2.7), (2.8), (2.9), (2.10), (2.15), and (2.16) establish a region in a piston speed vs clearance height plot within which the current RCM should be operated as shown in Fig. 2.5. The conditions (2.8) and (2.15) are not shown explicitly in the figure since the former is embraced by the condition (2.10) and the latter is beyond the window area of the figure. As shown in the operation map of Fig. 2.5, the piston speed should on one of the minimum pre-reaction lines bounded by the other criteria. The maximum allowable compression ratio can also be obtained by combining (2.7) and (2.10), and is 19.

The relations (2.14), (2.16), and (2.19) establish a region in a clearance height vs piston bore plot as shown in Fig. 2.6. This plot served as a guideline to determine the piston bore b, and it was chosen to be two inches for a standard size.

Basic dimensions chosen for the present machine are summarized in Table 2.3. They are remarkably close to those of the M.I.T. machine designed and operated in the 1950's by Taylor et. al. [6]

2.4 Basic configuration of the current RCM

An overall schematic of the machine is shown in Fig. 2.7. The basic design of the piston motion control was adapted from the Thornton rapid compression machine [16], i.e. high pressure gas drive, hydraulic speed control, and pin and groove stopping mechanism. The stationary parts were made from cold-rolled mild steel, whereas the

two moving parts, the piston and fast-acting-valve, were made from 6061 aluminum to reduce dynamic stress. Special attention was given to the piston which was made hollow to reduce its mass and to have uniformly distributed stress throughout the body.

To cover a wide range of experimental conditions, the rapid compression machine was designed with easily adjustable stroke, clearance height, piston speed, and initial charge temperature. The stroke can be varied by turning the stroke adjustment screw; the clearance height by changing the clearance height adjustment shim shown in Fig. 2.8; the piston speed by changing the speed control orifice area and the driving pressure; and the initial charge temperature using an oil bath in the heating jacket.

The clearance height is measured using a depth gauge with the accuracy of 1/1000 inch through the gas pressure transducer hole when the piston is at its lowest position by turning the stroke adjustment screw all the way down. The desired stroke is set accurately by turning the stroke adjustment screw counterclockwise, and each turn of the stroke adjustment screw gives 1/12 inch of stroke since the its threads are 1.5-12UNF. The angle of the stroke adjustment screw turned is measured using a protractor attached to the stroke adjustment screw knob. The stroke is checked again against the depth gauge measurement after the piston is moved to its uppermost position.

The driving chamber volume is made large enough that the driving pressure does not drop 5 % of the initial driving pressure when the gas in the driving chamber expands by the piston motion. The maximum driving pressure is limited to 3.45 MPa by material stress consideration.

A detailed drawing of the test chamber and the gas handling system used to prepare fuel, oxygen, and diluent mixtures is shown in Fig. 2.8. In the test

chamber, Teflon O-rings were used for all the static seals, and a Viton O-ring with a Teflon back-up ring was used for the piston dynamic seal. The piston head was machined separately from the piston body so that piston heads with the crevice and without the crevice could be easily interchanged. As explained earlier, the clearance height could also be changed easily by changing the clearance height adjustment shim. To eliminate dead volume, a spring loaded poppet valve was used to seal the test chamber.

Liquid fuel was injected into the machine using a syringe through a rubber septum of the type used in gas chromatographs. A 300 cc plenum was added to the filling line so that gas in the filling line was divided equally between the test chamber and the plenum when new gas was added from the manifold. This helped to reduce the uncertainty in the mixture composition due to back diffusion of gases from the test chamber into the filling line. The measured filling line volume was 45 cm^3 and the gas handling system line volume was 626 cm^3.

2.5 Instrumentation

To calculate the initial mixture compositions, static pressures up to 1000 torr were measured with an MKS 122A diaphragm absolute pressure gauge with an accuracy equal to 1 % of the reading. This absolute pressure gauge was calibrated periodically against a thermocouple vacuum gauge after evacuating the system less than 100 millitorr.

Dynamic pressures were measured using two Kistler 613 piezoelectric transducers located as shown in Fig. 2.7. One of these was used to monitor the oil pressure in the speed control chamber and provided information about the piston motion especially the starting and stopping time. The other which was coated with RTV to

reduce thermal sensitivity was used to measure the gas pressure in the test chamber. This pressure transducer is out of plane in Fig. 2.8.

All dynamic pressure transducers were calibrated against a dead weight tester and checked at periodic intervals. Fig. 2.9 shows a typical pressure transducer calibration curve. Charge amplifier output voltages were recorded as weights were added until the charge amplifier was saturated and as weights were removed until pressure became back to zero gauge pressure. The measured voltages were curve-fitted to a first order polynomial. The characteristic of the piezoelectric pressure transducer was linear as shown in the top plot of Fig. 2.9, and the departure from this linear fit was less than 0.1 % as shown in the bottom curve of the figure. This linear fit was used to convert charge amplifier output voltages to pressures. Periodic calibrations of the pressure transducers showed that the characteristic of the pressure transducer does not change with time.

The initial charge temperature was measured using a thermocouple located 1 mm below the test chamber as shown in Fig. 2.8. The oil temperature in the heating jacket is also measured to check the initial temperature uniformity of the test gas.

All data were recorded using a Transiac 2815 12-bit digitizer controlled by a DSP 4012 controller connected via Camac Crate to a VAX 11/750 host computer system, and the data were processed by a VAX 11/750 computer.

Time available for the measurement was usually of the order of 100 msec, and the synchronization of the data acquisition system and the RCM operation was critical to record the pressure rise in the test chamber with the limited memory capacity on the data acquisition system. The general layout of the timing circuit that synchronizes the start of data acquisition and the opening of the solenoid valve which starts the piston is shown in Fig. 2.10. Since the solenoid valve with a

1000 psi working pressure only operates on an alternating current, the 120 volt sinusoidal wave was converted to a TTL square wave and fed into the logic circuit so that the opening of the solenoid valve can be initiated at the same location on a 120V sinusoidal wave. The relay enable signal (RENABL) from the logic circuit was then sent to the relay circuit, which drives the solenoid valve to start the piston motion in RCM. The DHI signal from the timing circuit was also sent to the stop-trigger of the DSP 4012 controller in the data acquisition system to start the data record. The relay enable signal (RENABL) was delayed relative to the DHI signal by an amount set by the external clock rate (CLK) and the DCI 324 counter front panel settings so that the opening of the solenoid valve could be varied relative to the start of the data record. The detailed circuit diagrams for the timing circuit components are given in Appendix A.6.

2.6 Plumbing and operating sequence

All the oil lines of the current RCM's plumbing are shown in Fig. 2.11. The high pressure oils were supplied to the machine from the high pressure oil tank of 200 cm^3. To heat up the initial test gas, hot oil heated by the oil heater and controlled by a temperature controller was circulated through the heating jacket. Maximum oil temperature (or equivalently maximum initial test gas temperature) was limited to 100^o C due to the temperature resistance of O-ring materials. The valve-locking high pressure oil was relieved by the solenoid valve to the oil tank to start the operation of the RCM. Also shown in Fig. 2.12 are all the gas lines of the current machine's plumbing. Driving gas was prepared using a high-pressure air compressor, and other high pressure gases were supplied from 3000 psi N_2 bottles through a series of pressure regulators. High pressure gases were vented down to atmospheric pressure through the muffler to the trench, then the RCM was pumped

out by a vacuum pump through the oil trap to avoid any harmful effect of the hydraulic oil to the vacuum pump. The selection between the vent and the vacuum was made using the three-way valves.

The basic operating sequence of the machine is shown in Fig. 2.13 as follows (numbers in the parenthesis correspond to numbers in the figure):

(1) from the previous run, the piston is down and the valve is up;

(2) move the piston and the fast-acting-valve up by pressurizing the oil reservoir with 50 psi N_2;

(3) move the fast-acting-valve down by pressurizing the gas chamber above it with 100 psi N_2;

(4) lock the fast-acting-valve in position with the valve-locking high pressure oil;

(5) lock the piston in position by pressurizing the speed control chamber with the piston-locking high pressure oil;

(6) pressurize the driving chamber with a high pressure air;

(7) vent the oil reservoir and the gas chamber above the fast-acting-valve;

(8) fire the machine by opening the solenoid valve to relieve the fast-acting-valve locking pressure.

After this sequence, the fast-acting-valve is driven up by the piston locking pressure and the piston is driven down by the driving pressure. Toward the end of the stroke, the piston is slowed down by the stopping pin and groove mechanism [16]. In Table 2.4, the relation among the driving pressure, the piston-locking pressure, and the valve-locking pressure are given. The above sequence does not include mixture preparation which will be explained later in detail in conjunction with primary reference fuel experiments.

2.7 Simulation of RCM dynamics and optimal stopping pin shapes

The dynamics of the piston and the fast-acting-valve were simulated using a one-dimensional inviscid fluid model. Even though the equations derived in Appendix A.3 include lumped viscous effects using discharge coefficients and loss coefficients, they were set to ideal values, i.e., 1's and 0's for the present calculation since they were unknown. For the stroke of 7.84 cm, the clearance height of 0.6 cm, the speed control orifice area of 6.91 cm^2, and the driving pressure of 2.07 MPa, the displacements of the piston and the fast-acting-valve are shown in the top graph of Fig. 2.14. Also shown in the bottom graph of Fig. 2.14 are the corresponding speeds as a function of time. The bottom graph shows that the piston is accelerated in 2 msec; it maintains almost constant speed for the most part of the compression stroke; and it stops in 0.5 msec by the stopping pin and groove mechanism. The compression time was calculated to be around 8 msec, but as will be seen later in Chapter 3, the measured compression time is around 15 msec at the same operating conditions due to the viscous behavior of the hydraulic fluid. In Chapter 3, the discharge coefficients and loss coefficients will be adjusted to non-ideal values to accommodate this non-ideal behavior of the hydraulic fluid so that the calculated compression time matches with the measured one.

To obtain minimum stresses in moving parts, constant decelerations were required during their stopping. The optimal shape of the piston stopping pin which gives a constant deceleration was calculated using (A3.17) and (A3.20) as shown in Fig. 2.15 (see Fig. A.4 for the definition of r(Z) and Z). The same pin and groove stopping mechanism was used for the fast-acting-valve stopping, and the optimal shape of the valve stopping pin was also calculated using (A3.14) and (A3.16) as shown in Fig. 2.16 (see Fig. A.3 for the definition of r(Z) and Z). These pin shapes were machined carefully with precision, and used in actual RCM operation.

CHAPTER 3

RCM PERFORMANCE TEST WITH INERT GASES

Preliminary tests were conducted with inert gases to check the performance of the RCM and to determine its heat transfer characteristic. Clean gas pressure traces were recorded with little mechanical vibration. It was found that the oil pressure measurement from the speed control chamber provided an easy way to detect the piston motion. For the piston head with the corner vortex crevice, measured post-compression pressure agreed with pressure calculated assuming flow is laminar and the cooling rate of the test gas after compression was reduced, indicating that the corner vortex was successfully captured in the piston head crevice volume. The discharge coefficients and the loss coefficients of the RCM dynamic simulation model derived in Appendix A.3 were adjusted so that predicted compression times agree with measured ones. Laminar heat transfer model was developed to calculate the piston motion from the measured gas pressure, and the piston motions from two models, i.e., from the RCM dynamic simulation and from the heat transfer analysis agreed well.

These inert gas tests provide evidence that the RCM is operating properly and that the gas condition in the test chamber is consistent with expectation based on laminar theory.

3.1 Typical Pressure Traces

Fig. 3.1 shows the gas pressure of the test chamber and the oil pressure of the speed control chamber measured simultaneously. Using the oil pressure record, the information about the piston motion was obtained. At the point (1) of the figure, the valve-locking pressure was relieved by opening the solenoid valve. The oil

pressure of the speed control chamber (the piston-locking pressure) dropped slowly until the point (2) of the figure, at which the force acting on the piston by the oil pressure became the same as that acting by the driving pressure. After the point (2), the forces acting on the piston became unbalanced and the piston started to move by the high pressure driving force. Just before the point (3), the piston began to be decelerated by the stopping pin and groove mechanism. The piston came to rest at the point (3), which exactly matches with the peak pressure location of the gas pressure record. The fast-acting-valve motion can not be described directly from the measured oil pressure, and will be explained later in Fig. 3.4.

During the compression, the oil pressure oscillates at a frequency of 500 Hz. This oscillation can be explained by the spring effect of the hydraulic oil, and the detailed observation of this oil pressure oscillation is given in Appendix A.5.

Two small-amplitude oscillations were added to the gas pressure at the location (4) and (5) of Fig. 3.1 with frequencies of around 4 KHz. The vibrational signal of the same frequency recorded from the gas pressure transducer when the RCM was hit by a hammer is shown in the bottom graph of Fig. 3.2. Also shown in top graphs of Fig. 3.2 are the magnified views of (4) and (5) in Fig. 3.1. Since all three have the same frequencies of 4 KHz, the oscillations added to the gas pressure record are believed to be mechanical vibrations. It is also believed that the first one was due to the fast-acting-valve stopping; the second one was due to the piston stopping. The delay of around 5 msec of the second vibration from the peak pressure location of the gas pressure (or equivalently the piston stopping) in Fig. 3.1 would be too long if the RCM body were 100 % pure metal since the delay of 5 msec requires a length scale of 25 m. An explanation for this long delay is that gaskets and O-rings between parts of the RCM slowed down the transmission of vibrational signals.

3.2 Compression Time and Mean Piston Speed

Fig. 3.3 shows an overlay of two pressure traces from consecutive runs with pure N_2 at the same operating conditions. Time '0' was set to be the inflection point (or the steepest slope point) during the compression stroke since it is well-defined. This time shift is useful in measuring ignition delay times as will be seen in Chapter IV. The machine's performance was repeatable since the two pressure traces followed each other exactly. The compression time, τ_c, is defined to be the time between the piston start and the piston stop, and is measured to be 16 msec from the oil pressure record. The effective compression time, τ_{ec}, is defined as the time between the peak pressure location τ_p and the intersection of the steepest slope line with initial pressure, and is 3 msec. Since the temperature rises most rapidly at the end of compression, the effective compression time should be compared with the ignition delay time, and is of the same order as the shortest total ignition delay time measured.

To check the performance of the RCM, the compression times τ_c were measured by varying the stroke, the driving pressure, and the speed control orifice area. It is observed that the compression time is a function of the stroke S, the driving pressure P_d, and the speed control orifice opening area A_o as shown in Table 3.1. The dependence of the compression time on these three variables is consistent with expectation (see the bottom of Table 3.1) from the design consideration; the compression time is shorter with the shorter stroke, the higher driving pressure, and the the larger speed control orifice area. The mean piston speed u_p is defined as the ratio of stroke to compression time, and is given in the last column of Table 3.1. It is also observed that the mean piston speed is a function of the same dependence. The dependence of the mean piston speed on stroke is found to be weak, indicating that the acceleration and the deceleration of the piston occupy a

small fraction of the total compression time and that the piston travels at a constant speed for most part of compression stroke.

The discharge coefficients and the loss coefficients in the RCM dynamic model developed in Appendix A.3 (see also Fig. A.2 for the definitions of C_d's and k's) were adjusted by trial and error so that predicted compression times agree with measured ones. A set of discharge coefficients and loss coefficients which gives a reasonable agreement between the measured and the predicted compression times is as follows:

$C_{d3} = 0.65$ $\quad$ $C_{d4} = 0.75$

$k_1 = 150$ $\quad$ $k_2 = 0.8 \times 10^{-3}$ $\quad$ $k_3 = 50$

A typical piston and fast-acting-valve motion calculated using the above numbers is shown in Fig. 3.4. Comparison of this figure with Fig. 2.14 which was made with ideal values for C_d's and k's shows that the compression time is doubled due to viscous effect of the hydraulic oil. The compression times for various operating conditions were calculated using the above C_d's and k's and compared with the measured ones in Fig. 3.5. The points are close to a 45° line showing that the current RCM dynamic model predicts the compression time well.

3.3 Effect of Piston Head Crevice on Heat Transfer

The upper part of Fig. 3.6 shows two pressure traces for piston heads with and without the crevice with all other operating conditions kept same. Due to the crevice volume, the peak pressure for the piston head without the crevice is slightly higher than that for the piston head with the crevice, but the pressure drop rate after compression is faster. Isentropic pressures for both cases were calculated using geometric compression ratios, and are shown by lines (1) and (2) in the figure. The corresponding isothermal pressures defined as P_i x CR are shown by line (3) and (4)

and the initial pressure by lines (5). It can be seen that the measured post-compression pressures are significantly less than the ideal isentropic pressures and that the percentage discrepancy is less for the piston with the crevice. As will be seen below these departure can be attributed to the effects of boundary layers and the corner vortex.

Peak pressures are compared with various calculated pressures on a shorter time scale in the lower part of Fig. 3.6. Line (6) shows the isentropic pressure for the piston without the crevice corrected for the effect of the wall boundary layers using the displacement thickness calculated from the measured pressure traces assuming laminar flow [22]. It can be seen that the calculated pressure is still much higher than the measured peak pressure and the difference is attributed to the effect of the corner vortex. Line (7) shows the pressure calculated for the piston head with the crevice neglecting the boundary layers but assuming that the gas in the crevice is compressed isothermally while that in the test chamber is compressed isentropically. Finally line (8) shows the pressure calculated again assuming isothermal crevice but including the effect of the wall boundary layers in the test chamber. This matches the measured peak pressure almost exactly indicating that for the piston head with the crevice the flow was laminar and the corner vortex was successfully captured in the crevice. The slower pressure drop rate after compression for the piston head with the crevice also indicates that the crevice was successful in reducing heat transfer by suppressing the growth of the corner vortex.

Fig. 3.7 shows the measured peak pressures at various operating conditions and the corresponding predicted peak pressures from the laminar theory. The predicted peak pressures for the piston with the crevice were calculated the same way as the line (8) of Fig. 3.6; those for the piston head without the crevice were the same way as the line (6) of Fig. 3.6. The measured peak pressures for the piston head

with the crevice match well with the predicted peak pressure from the laminar theory, while those for the piston without the crevice are lower than the predicted ones. This observation re-assures that for the piston head with the crevice the flow was laminar and the corner vortex was successfully captured in the crevice. This also agrees qualitatively with Lyford-Pike's experimental observation that a bigger piston head crevice in an engine delays the onset of corner vortex formation during the compression stroke [26].

In the above discussion, the effect of O-ring pack dead volume shown in Fig. 3.15 was not taken into account. The gas flow into the O-ring pack dead volume during the compression and out of it after the compression is also important, but due to the uncertainties in estimating the dead volume its effect was not explicitly included in the discussion. The detailed discussion of the O-ring pack will be given later in section 3.5.

3.4 Piston Motion Calculation from Gas Pressure Record

The laminar heat transfer model for the piston with the crevice was developed in Appendix A.4, which yields the piston displacement and the amount of heat transfer to the surroundings from the measured gas pressure. Since the model involves differentiation of the pressure as in (A4.1), the measured pressure was first filtered and fed into the model. The filtered pressure using a finite impulse response (FIR) equi-ripple optimal low pass filter [27] and the raw measured pressure are shown in Fig. 3.8. The effect of filtering was to remove the vibration and the general shape of pressure trace was not changed. Using this filtered pressure, the thermal displacement thickness was calculated as shown in Fig. 3.9. It can be seen that the thermal displacement thickness decreases near the end of compression due to high pressure rise rate, and that it increases again when pressure rise rate drops due

to the piston stopping. An application of (A4.3) gives the piston displacement as shown in Fig. 3.10, and the piston displacement matches with the stroke at the end of compression. In Fig. 3.11, the volume ratio calculated from the piston displacement was compared with the effective compression ratio calculated from the measured pressure, where the effective compression ratio was defined as:

$$CR_{ef} = \exp\left[\int_{P_i}^{P} \frac{1}{\gamma} \frac{dP}{P} \right] \qquad (3.1)$$

where CR_{ef} is the effective compression ratio, and γ is the specific heat ratio. When γ is a constant, the above equation can be simplified as:

$$CR_{ef} = (P/P_i)^{1/\gamma} \qquad (3.2)$$

The difference of two curves in Fig. 3.11 is due to the heat losses of the test gas to the surroundings. The accumulated heat losses calculated using (A4.4) are shown in Fig. 3.12. When the core gas temperature was relatively low ,i.e., when the mass of gas in the crevice volume is small compared to that in the test chamber, the heat loss through the boundary layer was bigger than that through the crevice. Toward the end of compression when the mass of gas in the crevice volume is large compared to that in the test chamber, the heat loss through boundary layer became smaller than that through the crevice.

The piston motion calculated using the heat transfer model was compared with that from the RCM dynamic simulation. In Fig. 3.13, the piston motions calculated from both models were superimposed on each other, and they are close to each other except that the piston speed calculated from the heat transfer model shows oscillation. The cause of this oscillation will be discussed in Appendix A.5, and is found to be the spring effect of the hydraulic oil. The isentropic pressure based on the piston displacement calculated from the RCM dynamic simulation was compared with the measured pressure as shown in the top graph Fig. 3.14. Also the volume

ratio calculated the same way as in Fig. 3.11 are shown in the bottom graph of Fig. 3.14. Once again the differences among curves in Fig. 3.14 can be attributed to the heat losses as explained earlier in conjunction with Fig. 3.11.

3.5 O-ring Pack and Dead Volume

The O-ring pack dead volume is estimated assuming that the cross-sectional area of the O-ring remains the same when it is squeezed between the groove and the liner and that the cross-section of the O-ring becomes an ellipse when it is squeezed as shown in Fig. 3.15. The dead volume of O-ring pack is estimated around the half of the piston head crevice volume, and the gas flow into and out of the O-ring pack dead volume, therefore, can be important for the detailed flow calculation.

The O-ring floats inside the groove depending the pressure forces acting on it. When the pressure in the test chamber is higher than that on the the other side of the O-ring at the end of compression, the O-ring is pushed away from the test chamber to form a dead volume for the gas as shown in Fig. 3.15, which was initially '0' when the oil pressure in the speed control chamber is higher than the gas pressure in the test chamber.

The thermal displacement thickness shown in Fig. 3.9 is the same order of magnitude as the clearance gap between the piston and the liner (around 1/10 mm). Instead of forming a corner vortex by the moving piston, the boundary layer can be sucked into this dead volume during the compression. It is also suggested that the temperature of the gas in the piston head crevice is higher than the wall temperature to explain small post-compression pressure differences for the piston head with and without crevice as shown in Fig. 3.6; and that the shape of the piston head crevice volume acts as a barrier when the cold gas comes out of the O-ring

pack dead volume to explain faster pressure drop rate for the piston without a crevice.

To explore these possibilities, the measurement of the O-ring pack dead volume should be first carried out using a transparent liner. The possible solution to reduce the dead volume can be either to reduce the width of the O-ring groove so that O-ring does not float in the groove; or to use a rectangular metallic ring made out of soft material.

CHAPTER 4

IGNITION DELAY MESUREMENTS FOR PRIMARY REFERENCE FUELS

Throughout the primary reference fuel experiments, the piston head with the crevice was used to reduce heat transfer. The other operating conditions which were kept constant are as follows:

stroke : 9.51 cm

clearance height : 0.615 cm

driving pressure : 2.07 MPa

speed control orifice area : 10.58 cm^2

Before attempting to measure ignition delay times, careful studies were made to ensure reliable and repeatable results. O-ring with the least absorptivity for hydrocarbons was selected and the time to reach saturation was measured. Filling and purging procedures were developed to eliminate carry-over of combustion products from previous runs which were found to affect the delay time measurements. Finally a well-defined set of definitions was introduced for the ignition delay times.

4.1 O-ring Absorption Studies

It is known that many O-ring materials absorb hydrocarbons, therefore Teflon O-rings were used for all seals on the test chamber since it was found that Teflon has the least absorptivity for hydrocarbons. There were places, however, where Teflon O-ring could not be installed due to its stiffness, and Viton O-rings covered with Teflon back-up rings were used in these places as shown in Fig. 2.8. The O-ring material "Kalrez" by Du-Pont was claimed to be as elastic as Viton and as chemical-resistant as Teflon, but there was not enough information about the

absorptivity and Kalrez O-ring was too costly (usually $100 for a small piece of O-ring) at the time of the experiment.

Fig. 4.1 shows the test chamber pressures as a function of time after filling with various gases. For inorganic gases like N_2 and O_2, the pressure remained constant for 20 minutes indicating that there was neither leakage nor absorption. For fuels such as normal-heptane and iso-octane, however, the pressure dropped exponentially with a time constant of approximately 5 minutes to an asymptote where the O-rings are believed to be saturated with hydrocarbons. No significant change in pressure was observed after 10 minutes. Therefore, ten minutes, was determined to be a suitable waiting period for O-ring absorption saturation. As can be seen in Fig. 4.1, the pressure curves for normal-heptane and iso-octane are almost identical and the difference in peak pressures of two pressure traces is the same as that in the pressure asymptotes after 20 minutes. This is consistent with the fact that the absorption of homologous hydrocarbons such as Alkanes is the same.

It is also important to check that the vapor pressure of liquid fuel is high enough at the temperature the fuel is injected to ensure all the liquid is evaporated. For example, at an initial pressure of 1000 torr, an equivalence ratio of 1, and a diluent/O_2 ratio of 3.77, the partial pressures needed for iso-octane and normal-heptane are 16.8 torr and 19.0 torr respectively, and their vapor pressures at 300 K are 54.3 torr and 50.6 torr [28].

4.2 Filling and Purging Procedures

Initial mixture homogeneity and quiescence in the rapid compression machine must be achieved to ensure reliable and repeatable results. Any species left from the previous run should be purged so that an experiment is independent of the previous run.

The following steps were performed for each run:

(1) evacuate the system to a pressure less than 100 millitorr;

(2) inject fuel through the injection septum, and wait for 10 minutes for O-ring absorption saturation;

(3) feed O_2 and diluents, and wait another 10 minutes for mixture homogeneity;

(4) fire the rapid compression machine;

(5) reset the rapid compression machine;

(6) evacuate the system;

(7) purge the system with O_2, and evacuate the system;

(8) purge the system with N_2, and evacuate the system;

(9) feed the system with air, wait 10 minutes for any remaining species to diffuse into the air, and evacuate the system;

(10) prepare for the next run, i.e. go to step (2).

The steps (1) to (4) in the above sequence are graphically shown in Fig. 4.2. To minimize temperature overshoot and avoid any pre-reactions when various gases were admitted to the test chamber in step (3), they were fed in very slowly by slightly opening the valve connecting the test chamber and the gas manifold. The gas manifold pressure, before admitting gas into the test chamber, was set so that the pressure in the test chamber had the desired value when the two pressures equilibrated at the end of the feeding procedure for each gas.

The order of feeding O_2 and diluents was changed to see if the initial mixture homogeneity was achieved, and it was found that the change of feeding order did not have any effect on the experimental results as long as the 10-minute waiting period for the mixture homogeneity was observed.

The repeatability of primary reference fuel experiments was checked with the above filling sequence to ensure reliable data since it is known that the repeatability of ignition delay measurements in previous rapid compression machines has been poor. Three consecutive runs at the same operating conditions are shown in the top graph of Fig. 4.3. It can be seen that the post-compression pressures are identical but that the ignition delays decreased with increasing run number. This indicates that even though the system was purged three times after each run, there were still species left in the test chamber from the previous run.

To reduce the residual species from the previous run, a new purging procedure was added which involved making a dummy run with pure O_2 before each measurement run. The bottom graph of Fig. 4.3 shows three consecutive runs made at the same operating conditions after making runs with pure O_2 before each run. The measured ignition delays are no longer ordered and are within 5 % of each other. Also the average value is the same as that for the first run in the top graph. To check whether the effect of the O_2 run is to dilute or to burn up active species left in the test chamber from the previous run, O_2 was substituted with N_2 and the ignition delays were measured as a function of the run number. It was found that the ignition delays decreased as the run number increased with the N_2 run between measurement run. It is believed that the effect of the O_2 run before each primary reference fuel experiment is to burn up active species adsorbed on the test chamber walls.

4.3 IGNITION DELAY MEASUREMENTS

All the experiments were conducted at an equivalence ratio of 1.0. A mixture of N_2 and Argon was used for the diluents to change the post-compression temperature, and the diluent to O_2 ratio was 3.77. The initial charges were at

room temperature (23° ~ 27° C). Five primary reference fuels (ON = 100, 90, 75, 50, and 0) were investigated at two initial pressures (500 torr and 1000 torr) and at three N_2/diluent ratios (0.5, 0.7, and 1.0).

Pressure records for different primary reference fuels are superimposed on each other at three different N_2/diluent ratios in Fig. 4.4 through Fig. 4.6 for the initial pressure of 500 torr. Also shown in Fig. 4.7 through Fig. 4.9 are pressure records for the initial pressure of 1000 torr. The core temperatures were calculated in two ways, and are given on the right ordinate of the figures. Before there is appreciable heat release by reactions, as in the region marked $\Delta s=0$ in the figure, isentropic relations based on measured pressure ratios were used to calculate core temperature. Even though a variable specific heat ratio was used for the core temperature calculations, average specific heat ratios are also given in the figures for reader's convenience. When there is appreciable chemical heat release as in the region marked $\Delta v=0$, it is assumed that the boundary layer heat loss is sufficiently small so that a constant volume condition can be used to calculate core temperatures.

The curves in Fig. 4.4 through Fig. 4.9 show the well known two stage ignition typical of hydrocarbon oxidation in the temperature and pressure range investigated. They can be used to provide a critical test of kinetic models [1,29] of this process.

The definitions of ignition delay times have been unclear and inconsistent in the previous literature. The definitions used in the present study are as follows:

(1) first-stage ignition delay (τ_1):

time between the intersection of the steepest slope with the post-compression pressure and the inflection point in the pressure step during first-stage ignition;

(2) second-stage ignition delay (τ_2):

time between the inflection point in the pressure step and the point during explosion where core temperature is 1100 K;

(3) total ignition delay (τ_t): sum of τ_1 and τ_2;

The above definitions are shown in Fig. 4.4. The rational for choosing 1100 K as the explosion temperature was that the slope of the pressure was so steep during explosion that there were no differences in ignition delay time measurements when any higher temperatures were used.

The measured total ignition delay times τ_t defined above are shown on an Arrhenius plot in Fig. 4.10. It is clearly seen that the total ignition delay increases with increasing octane number. It is also seen that ignition delay is not a linear function of octane number and that most of change in ignition delay occurs in the range from octane number 100 to 50. The temperature effect on total ignition delay is monotonic for the experimental range covered and the total ignition delay decreases with increasing temperature. The total ignition delay decreases as the initial pressure increases even though it is not completely rigorous to compared ignition delays at slightly different post-compression temperatures since the post-compression temperature at 500 torr initial pressure is slightly lower than that at higher initial pressure at the same N_2/diluent ratio.

The total ignition delay times normalized by those of iso-octane (ON = 100) are shown as a function of the octane number in Fig. 4.11. The normalized ignition delay times fall most rapidly between ON = 100 and 50 as observed in the discussion of Fig. 4.10. The total spread from ON = 0 to 100 increases as the initial pressure (or density) decreases and decreases as the temperature decreases.

The measured second-stage ignition delay times, τ_2, are shown in Fig. 4.12. Only values larger than 10^{-1} msec are shown because smaller values could not be measured accurately. For the second-stage ignition delay times less than 10^{-1} msec,

the pressure step between the first-stage and the second stage ignition was so masked by the pressure waves due to high heat release as shown in Fig. 4.13 that a question about the existence of two-stage ignition was raised. Based on the measurable second-stage ignition delay times, it can be seen that the second-stage delay time is a weak function of temperature but increases as the octane number increases and decreases as the initial pressure (density) increases. It can also be seen from a comparison of Figs. 4.11 and 4.12 that for the temperature and pressure range investigated, the second-stage delay time is small compared to the total delay time so that most of the delay is due to the first-stage reactions.

The pressure rise during the first-stage ignition, ΔP is defined as the difference between the minimum pressure after compression and the pressure at the inflection point in the pressure step as shown in Fig. 4.5. The pressure rises were measured only when the second-stage ignition delays could be measured as explained above, and are shown in Fig. 4.14. It can be seen that the pressure rise is lower for the lower initial pressure and for the higher octane number. It can be also seen that the total spread of the pressure rise increases slightly as the temperature increases, indicating that the temperature dependence on the pressure rise is weak.

4.4 Comparison with Existing Data

Current measured ignition delays were compared with existing data. For iso-octane, data have been reported by Halstead et. al. [7] and Taylor. et. al. [6]. For normal-heptane, the data available were by Taylor et. al. [6] and Rogener's correlation [15].

In their original paper, Halstead et. al. used average temperatures, and they were converted to core temperatures by Hu and Keck [1] using the pressure data provided by original investigators. There were, however, no original pressure data available

for Taylor's data, and isentropic temperatures were calculated based on geometric compression ratios provided in the paper. For Rogener's correlation, it was not explicitly stated in the paper how the post-compression pressure and temperature were measured to make the correlation.

In Fig. 4.15, current iso-octane data along with Halstead's and Taylor's data are shown on an Arrhenius plot. Even though Halstead's data were taken at an equivalence ratio of 0.9, they are included since it was reported by Taylor et. al. that the effect of equivalence ratio on ignition delay in the vicinity of equivalence ratio 1 was weak for iso-octane. Halstead's data show that the ignition delay time increases as the initial pressure increases, agreeing qualitatively with current data. The quantitative comparison, however, shows that the temperature dependence does not match. Taylor's data taken at equivalence ratio 1 with varying compression ratio would match well with the current data if the temperature were true core temperature. The discrepancies can probably be attributed to the difficulty of determining the core temperature in the previous experiments from the available data. As shown earlier in Table 2.1, the Thornton RCM for taking Halstead's data was characterized by high heat transfer due to large corner vortex size, yet their measured post-compression pressures were very close to ideal isentropic pressures or sometimes higher. It is believed that their pressure measurements were unable to determine core temperature due to high mechanical vibration as shown in Fig. 2.1.

Fig. 4.16 shows the current normal-heptane data along with Taylor's data and Rogener's correlation. All three sets of data show the same temperature dependence but the curves are shifted relative to one another. Once again this can probably be attributed to errors in determining the core temperature.

The data taken from the current RCM when the purging with O_2 preceding run was not known are shown in Fig. 4.17, and this set of data match quite well

with the Rogener's correlation both qualitatively and quantitatively. This fact raise a question about proper purging procedures in measuring some of existing data.

The most likely source of error in previous works is the failure to take into account the effects of the corner vortex which was unknown at the time the work was done. Another source of error is the failure to use adequate purging procedures to eliminate run-to-run interference. The uncertainties in core temperature give the horizontal shift of curves on an Arrhenius plot like Fig. 4.16, and the run-to-run interference of active species gives the vertical shift of curves on an Arrhenius plot. The quantitative disagreement of three sets of data in Fig. 4.16 can be explained by the combined effect of these horizontal and vertical shift.

Since the design objective of having a well-defined uniform core gas region was achieved by incorporating the piston head crevice volume as explained in Chapter III; the O-ring absorption study allowed the accurate determination of initial charge compositions; and the O_2 dummy run between measurement runs made the ignition delay measurements repeatable, it can be said that the current ignition delay measurements are the most accurate. The previous ignition delay measurements should be carefully re-evaluated due to difficulties in determining core temperature and possible run-to-run interference of active species adsorbed on the wall.

CHAPTER 5

SUMMARY AND CONCLUSION

A rapid compression machine designed for the study of chemical kinetics has been developed. Tests with inert gases show that the flow was laminar and the corner vortex was captured in the piston head crevice. They also strongly suggest the existence of a well-defined adiabatic core gas the temperature of which can be accurately determined from the pressure records. Using this facility, ignition delay measurements have been made with homogeneous fuel/oxygen/diluent mixtures for five different normal-heptane/iso-octane mixtures with octane numbers of 100, 90, 75, 50, and 0 at two initial pressures.

On the basis of the observations, the following conclusions can be drawn for the experimental range covered:

(1) Incorporation of a piston crevice volume helps to suppress the wall vortex and reduce cooling rates;

(2) The O-ring absorption study allowed the accurate determination of initial charge compositions;

(3) The repeatability of primary reference fuel experiments was achieved by using a dummy O_2 run between measurement runs, and measured ignition delays were repeatable within 5 percent;

(4) Ignition delays are a nonlinear function of octane number showing little change from 0 to 50 and most change from 50 to 100;

(5) The first-stage ignition delay is a strong function of temperature, but the second-stage ignition delay is a weak function of temperature;

(6) At lower initial pressure, the ignition delays are longer and more widely spread with octane numbers;

(7) The current rapid compression machine is a reliable tool for the study of autoignition under well defined conditions;

(8) The present results should be valuable for critical testing of kinetic models of hydrocarbon oxidation.

Knocking in an SI engine typically occurs around 1000 K, and further studies at higher temperatures are needed to draw any general conclusions about ignition delay behavior of primary reference fuels.

REFERENCE

[1] Hu, H. and Keck, J., "Autoignition of Adiabatically Compressed Combustible Gas Mixture," SAE 872110 (1987)

[2] Taylor, C.F., "The Internal Combustion Engine in Theory and Practice," M.I.T. Press, Cambridge, MA (1984)

[3] Obert, E.F., "Internal Combustion Engines and Air Pollution," Harper & Row Publishers, New York (1973)

[4] Lewis, B. and von Elbe, G., "Combustion, Flames and Explosions of Gases," Academic Press, New York (1987)

[5] Pollard, R.T., "Comprehensive Chemical Kinetics," v.17, C.H. Bamford and C.F.H. Tipper, Eds., Elsevier, Amsterdam (1977)

[6] Taylor, C.F., Taylor, E.S., Livengood, J.C., Russell, W.A., and Leary, W.A., "Ignition of Fuels by Rapid Compression," SAE Quarterly Transaction, v.4, No.2, pp.232 (1950)

[7] Halstead, M.P., Kirsh, L.J., and Quinn, C.P., "The Autoignition of Hydrocarbon Fuels at High Temperatures and Pressures - Fitting of a Mathematical Model," v.30, pp.45 (1977)

[8] Behrens, H., Lehr, H., Struth, W., and Wecken, F., "Shock-Induced Combustion by High Speed Shots in Explosive Gas Mixtures," Dtshc.-Fr. Forschungsinst. Rep. 4/67, Saint-Louis, France (1967)

[9] Tabaczynski, R.J., Hoult, D.P., and Keck, J.C., "High Reynolds Number Flow in a Moving Corner," J. Fluid Mech., v.42, pp.249 (1970)

[10] Halstead, M.P., Kirsh, L.J., Prothero, A., Quinn, C.P., "A Mathematical Model for Hydrocarbon Autoignition at High Pressure," Proc. Roy. Soc., A346, pp.515 (1975)

[11] Schmidt, F.A.F., "The Internal Combustion Engine," Chapman and Hall, London (1965)

[12] Hee Lum Ng., "An Investigation of the Ignition of Hydrocarbon-Air Mixtures in an Adiabatic Compression Machine," Ph.D. Thesis, Dept. of Chemical Engineering, Imperial College, University of London (1963)

[13] Jost, W., "Knock Reaction," 11th Int. Symp. Combust. (1963)

[14] Voinov, A.N., Skorodelov, D.I., and Sokolov, F.P., "Temperature and Pressure Dependence of Retarded Ignition of Hydrocarbon-Air Mixtures during Adiabatic Compression," Kinetika i Kataliz, v.5, No.3, pp.388 (1964)

[15] Rogener, V.H., "Entzundung von Kohlenwasserstoff-Luft-Gemiischen durch adiabatische Verdichtung," Z. Electrochemie, v.53, pp.389 (1949)

[16] Affleck, W.S., and Thomas, A., "An Opposed Piston Rapid Compression Machine for Preflame Reaction Studies," Proc. Inst. Mech. Engrs., v.183, No,18, pp.365 (1969)

[17] Rogowski, A.R., "New Machine for Studying Combustion of Fuel Sprays with Controlled Air Motion," SAE Preprint 436F (1963)

[18] Beeley, P., Gray, P., and Griffiths, J.F., "Shock Sensitivity of Liquid Propellants : The Exothermic Decomposition of Isopropyl Nitrate under Rapid Compression," 17th Int. Symp. Combust. (1979)

[19] Ikegami, M., Miwa, K., and Inada M., "A Study of Ignition and Combustion of a Diesel Spray by Means of a Rapid Compression Machine," Bulletin of JSME, v.24, No.195, pp.1608 (1981)

[20] Hayashi, T., Taki, M., Kojima, S, and Kondo, T., "Photographic Observation of Knock with a Rapid Compression and Expansion Machine," SAE 841336 (1984)

[21] Ohta, Y., Hayashi, A.K., Takahashi, H., and Fujiwara, T., "Consequence of Temperature-Pressure-Time History for Autoignition," to be printed

[22] Keck, J.C., "Thermal Boundary Layer in a Gas Subject to a Time Dependent Pressure," Letters in Heat and Mass Transfer, v.8, pp.313 (1981)

[23] Hoult, D.P., Fay, J.A., and Forney, L.J., "A Theory of Plume Rise Compared with Field Observation," J. Air Pollution Control Assoc., v.19, No.8, pp.585 (1969)

[24] Reynolds, W.C., "Thermodynamic Properties in SI : Graphs, Tables and Computational Equations for 40 Substances," Dept. of Mech. Eng., Stanford Univ. (1979)

[25] Stull. D.R., Westrum, E.F., and Sinke, G.C., "The Chemical Thermodynamics of Organic Compounds," John Wiley & Sons, Inc., New York (1969)

[26] Lyford-Pike, E.J., "Measurement and Analysis of Thermal Boundary Layer Thickness in the Cylinder of a Spark Ignition Engine," M.S. Thesis, M.I.T. (1979)

[27] Oppenheim, A.V., and Schafer, R.W., "Digital Signal Processing," Prentice-Hall, Englewood Cliffs, NJ (1975)

[28] American Petroleum Institute, Project 44 "Selected Values of Physical Properties of Hydrocarbons and Related Compounds," (1953)

[29] Westbrook, C.K., Warnatz, J., and Pitz, W.J., "A Detailed Chemical Kinetic Reaction Mechanism for the Oxidation of Iso-octane and N-heptane over an Extended Temperature Range and Its Application to Analysis of Engine Knock," 22th International Symposium of Combustion, (1988)

[30] Metgahlchi, M., "Laminar Burning Velocity of Mixtures at High Temperature Mixtures of Air with Indolene, Isooctane, Methanol and Propane," Sc.D. Thesis, M.I.T. (1980)

[31] Baumeister, T., Avallone, E.A., and Baumeister III, T., "Marks' Standard Handbook for Mechanical Engineers," 8th Eds, McGraw-Hill, NY (1978)

Table 2.1 Review of Recent RCM's

reference	piston speed max (m/s)	compression ratio and adjustment	bore	driving mechanism	stopping mechanism	catagory
Taylor, C.F.(MIT) [6]	15	impact ring thickness change	2"	pneumatic	gas cushion chamber	c
Schmidt, F.A.F.[11]	60	*	3.15"	pneumatic	plastic deform	c
Hee Lum Ng [12]	*	*	*	pneumatic	same as above	c
Jost, W. [13]	*	*	*	pneumatic	recoil mass	c
Voinov, A.N. [14]	25	cylinder head change	101.6 mm	pneumatic	hydraulic pin and cross bar	c
Rogener, V.H. [15]	10	max 15:1	*	pneumatic	recoil mass	c
Affleck, W.S. [16]	17	7:1 - 10:1	3.81 cm	pneumatic	hydraulic pin	c
Rogowski, A.R. (MIT) [17]	20	head plate change	4"	pneumatic	snubbing chamber	e
Beeley, P. [18]	10	11.4	1.86 cm	pneumatic	hydraulic pin	c
Ikegami, M. [19]	100	6	5cm	pneumatic	plastic deform	e
Hayashi, T. [20]	2.3	7.5	8.5 cm	electrohydraulic servo system		e
Ohta, A.K. [21]	5.6	6	6.5 cm	pneumatic	mechanical impact	c
current RCM	10	5:1 - 17:1	2"	pneumatic	hydraulic pin	c

e : engine-biased RCM
c : chemistry-biased RCM
* : information unavailable

Table 2.2 Heat Transfer Characteristics of Chemistry-biased RCM's

RCM'S	Taylor,C. F. [6]	Affleck, W.S. [16]	Beeley, P. [18]	Ohta, A.K. [21]	current RCM
date	1950	1969	1979	1983	1988
number of cylinder	1	2	1	1	1
driving mechanism	pneumatic	pneumatic	pneumatic	pneumatic	pneumatic
speed control	inertia	hydraulic	hydraulic	inertia	hydraulic
stopping mechanism	gas cushion chamber	hydraulic pin	hydraulic pin	mechni-cal impact	hydraulic pin
compression time (ms)	5	6-10	20	25	15-18
bore (cm)	5.08	3.81	4.5	6.5	5.08
clearance height (cm)	.5-1.3	3.81	1.86	2.8	0.6-2
stroke (cm)	7.62	11-17	19.4	14	5-10
compression ratio	7-16	7-10	11.4	6	3-17
avg piston speed (m/s)	15	17	10	5.6	7
temperature variation	2.6E-4	4.4E-4	1.5E-4	0.5E-4	0.5E-4
thermal boundary layer thickness (mm)	0.07	0.12	0.15	0.25	0.08
measured cooling time (ms)	200	100	100	*	300
calculated cooling time (ms)	590	900	870	1130	360
measured cooling time /calculate cooling time	0.34	0.11	0.12	*	0.83
corner vortex diameter (cm)	0.65	0.79	0.84	1.13	suppre-ssed
2 * corner vortex diameter / bore	0.26	0.41	0.37	0.35	suppre-ssed
operational	no	yes	yes	yes	yes

Table 2.3 Design Parameters for Current RCM

test chamber bore	5.08 cm	b
driving chamber diameter	10.16 cm	B
piston length	17.21 cm	L_p
piston mass	0.969 Kg	M_p
stopping pin length	0.127 cm	l_{sp}
corner vortex crevice volume	0.527 cm^3	V_{cr}
clearance height	0.6 - 2 cm	h
maximum stroke	10.92 cm	S
maximum driving pressure	3.45 MPa	P_d
max speed control orfice area	14.19 cm^2	A_o
maximum piston speed	10 m/s	u_p

Table 2.4 Driving Pressures and Oil Pressures
: Unit = psi (MPa)

Driving Pressure	Piston-locking Oil Pressure	Valve-locking Oil Pressure
100 (0.69)	150 (1.03)	250 (1.72)
200 (1.38)	300 (2.07)	450 (3.10)
300 (2.07)	450 (3.10)	650 (4.48)
400 (2.76)	600 (4.14)	900 (6.21)
500 (3.45)	700 (4.83)	1000 (6.89)

Table 3.1 Measured Compression Time and Mean Piston Speed : Gas=N_2, P_i=720 torr, T_i=302±1 K, clearance height=0.6 cm, Piston Head with Crevice

stroke, (cm) S	driving pressure, (MPa) P_d	speed control orfice opening angle, (deg) θ	τ_c (msec)	mean piston speed, (m/s) u_p
7.84	2.07	11.0	28.4	2.76
7.84	2.07	19.2	18.8	4.17
7.84	2.76	19.2	16.3	4.81
7.84	2.07	29.8	9.9	7.02
5.28	2.07	11.0	19.0	2.78
5.28	2.07	19.2	13.2	4.00
5.28	2.76	19.2	11.6	4.55

$$\tau_c = fn(S, P_d, A_o) \sim S/A_o/\sqrt{P_d}$$

$$u_p = S/\tau_c = fn(S, P_d, A_o) \sim A_o\sqrt{P_d}$$

where $A_o = 0.1129\pi\theta$ in cm^2

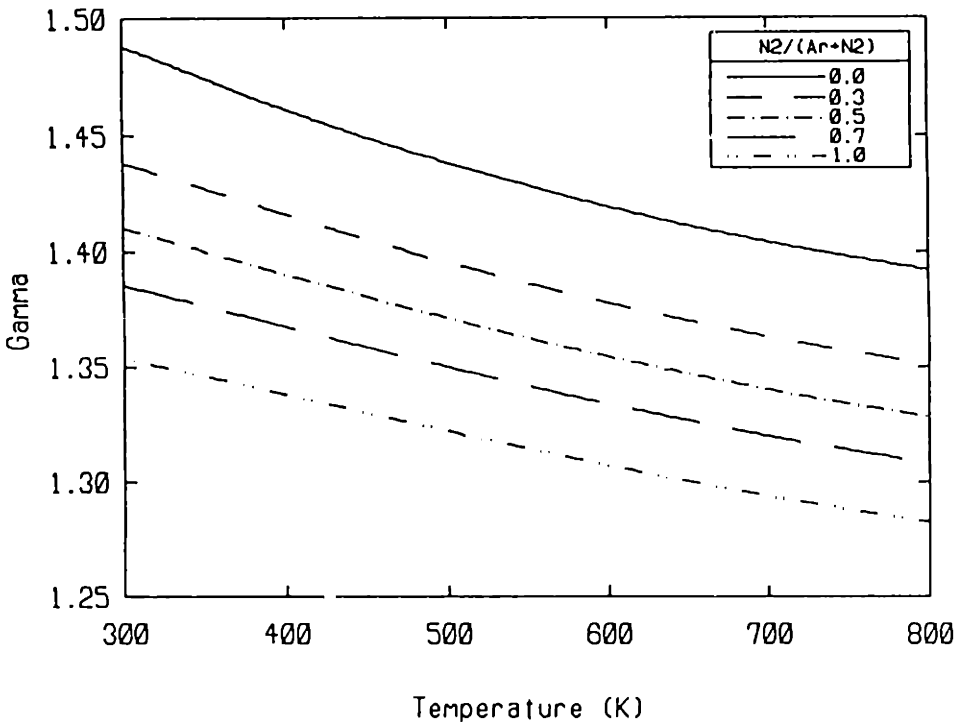

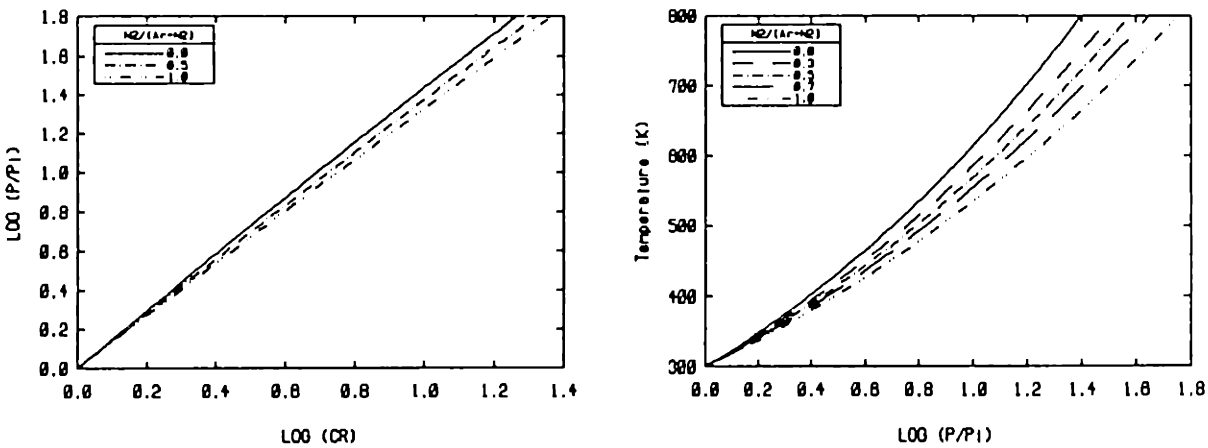

Figure 2.1 Specific Heat Ratio, and P-T-CR Relation for Isentropic Compression of i-C_8H_{18}/O_2/N_2/Ar Mixture : Equivalence Ratio=1, (N_2+Ar)/O_2=3.77, and T_i=300 K

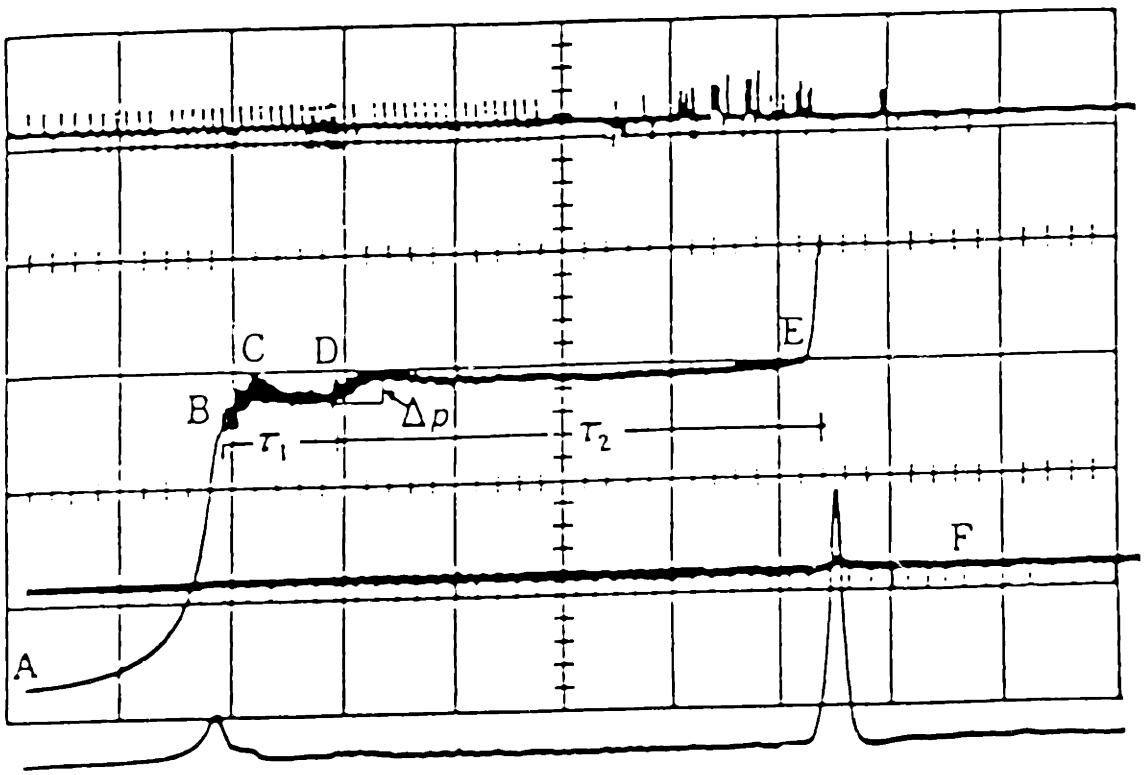

Figure 2.2 Pressure Record Taken from Thornton RCM

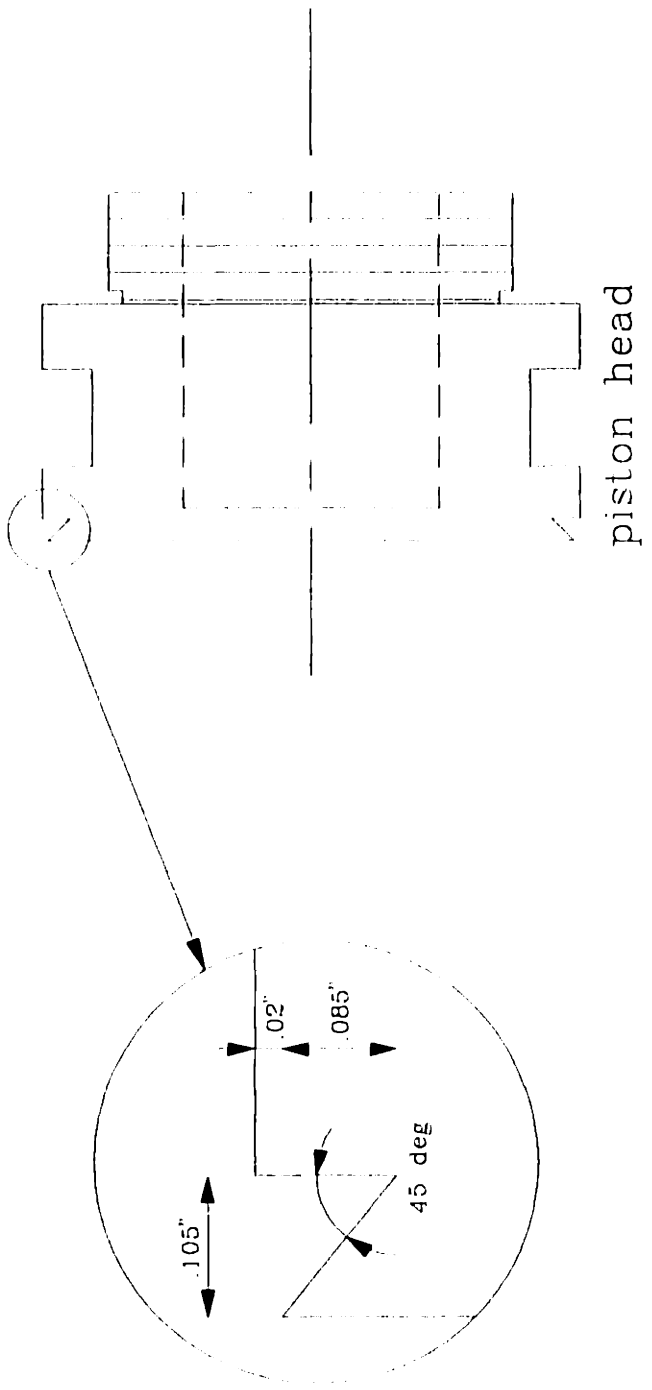

Figure 2.3 Shape of Corner Vortex Containment Crevice : Crevice Volume=0.527cc

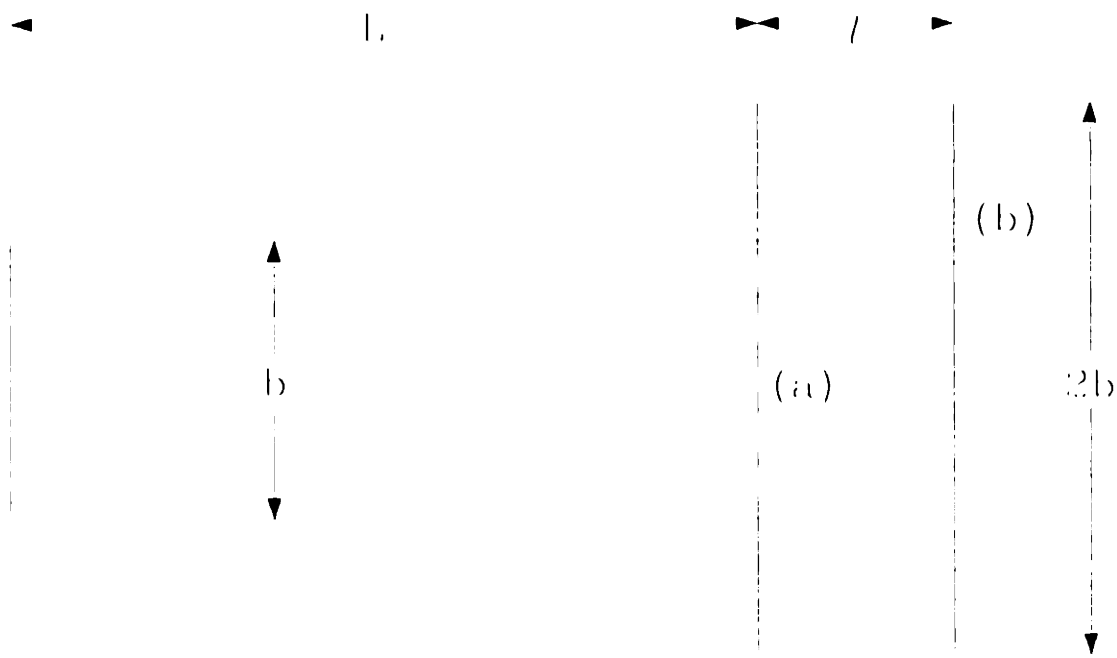

Figure 2.4 Stress Consideration for Piston : Ratio of Test Chamber Bore to Driving Chamber Bore=0.5

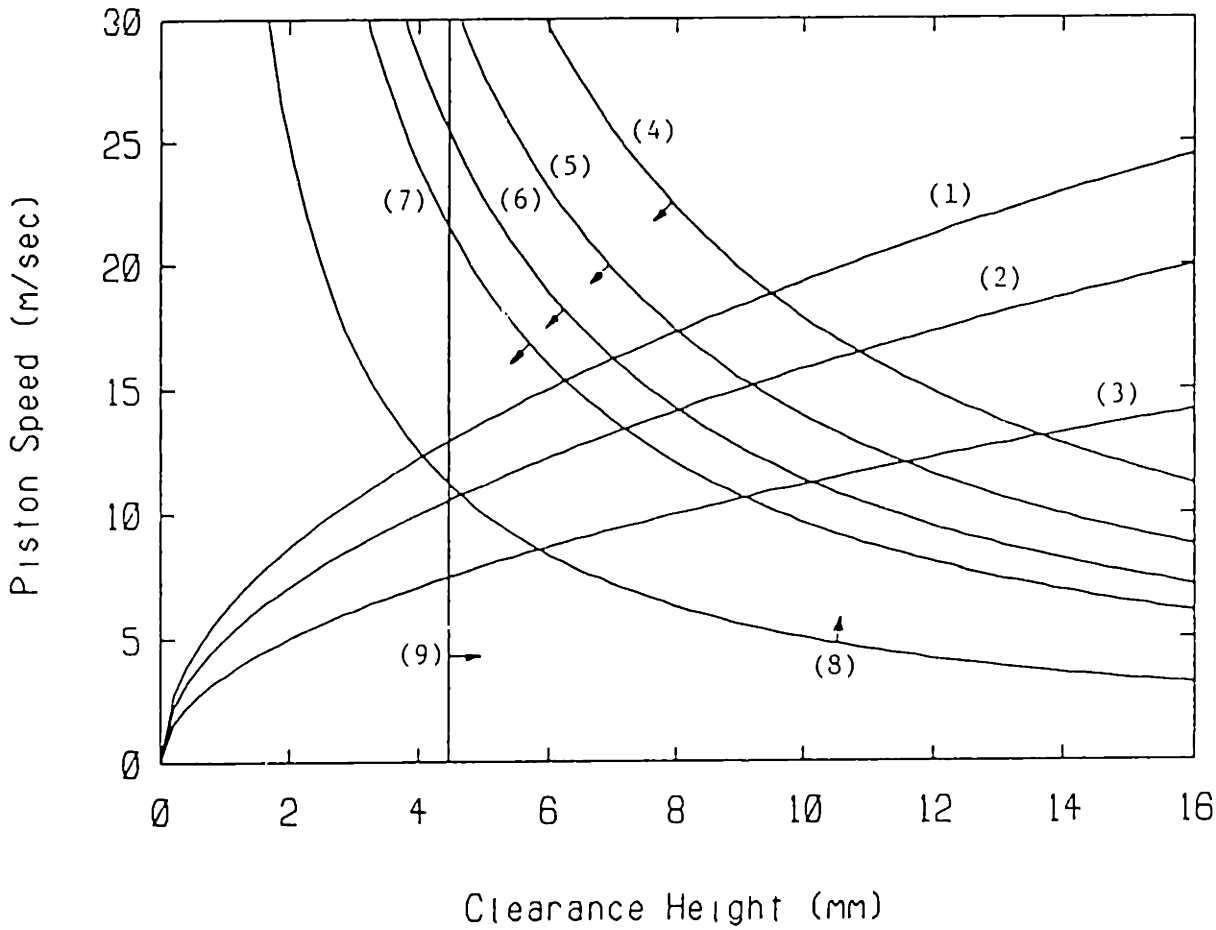

Figure 2.5 Operation Map of Current RCM : (1) Minimum Pre-reaction for $a=1.5\times10^{5}$ m/sec^2, (2) Minimum Pre-reaction for $a=10^{5}$ m/sec^2, (3) Minimum Pre-reaction for $a=0.5\times10^{5}$ m/sec^2, (4) Laminar Condition for CR=8, (5) Laminar Condition for CR=10, (6) Laminar Condition for CR=12, (7) Laminar Condition for CR=14, (8) Ratio of Laminar Cooling to Characteristic Heating Time > 1000, (9) Laminar Cooling Time > 1 sec, R=287 J/Kg/K, $T_f=1/\beta_f=1000$ K, $Re_{crit}=2.5\times10^{5}$, $\nu=5\times10^{-6}$ m^2/sec, $\alpha=5\times10^{-6}$ m^2/sec, $\gamma=1.4$, $\theta=10^{4}$ K

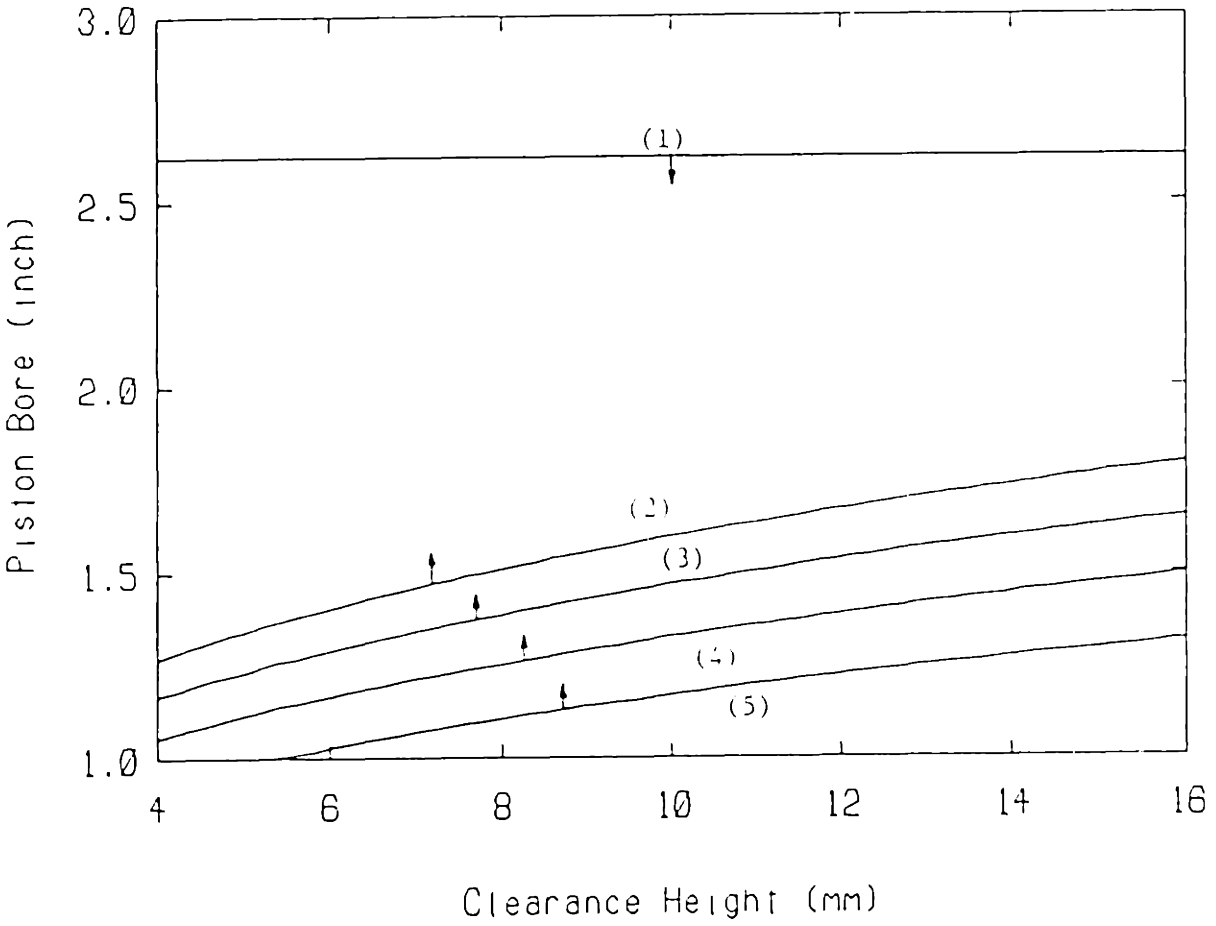

Figure 2.6 Design Map of Current RCM : (1) Dynamic Stress Consideration, (2) Corner Vortex Containment Volume Effect for CR=14, (3) Corner Vortex Containment Volume Effect for CR=12, (4) Corner Vortex Containment Volume Effect for CR=10, (5) Corner Vortex Containment Volume Effect for CR=8, $T_f=1/\beta_f=1000$ K, $\nu=5\times10^{-6}$ m^2/sec, $\gamma=1.4$, $\theta=10^4$ K, $Y/\rho=5\times10^4$ m^2/s^2, $n=5$

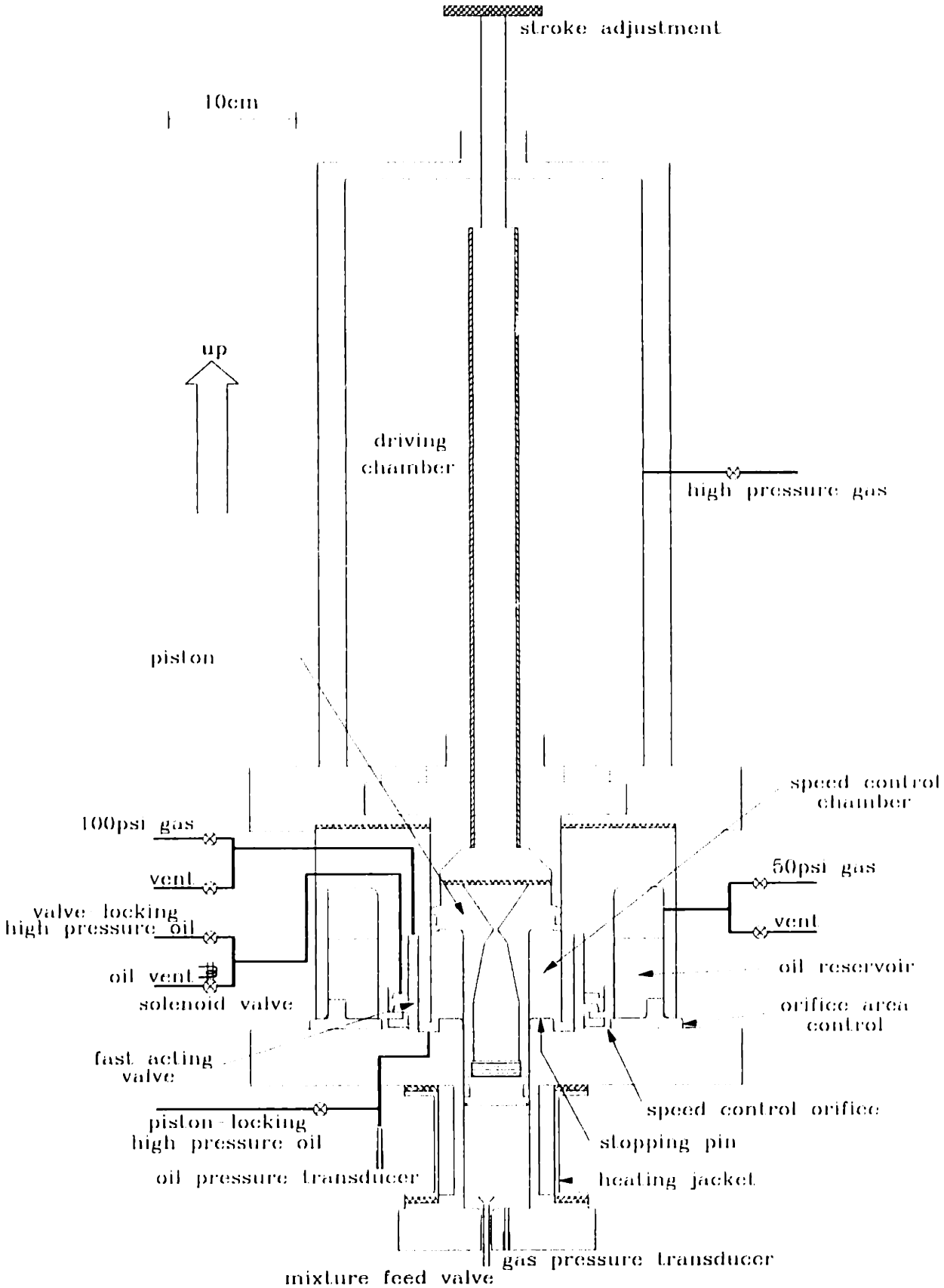

Figure 2.7 Sectional View of RCM Assembly

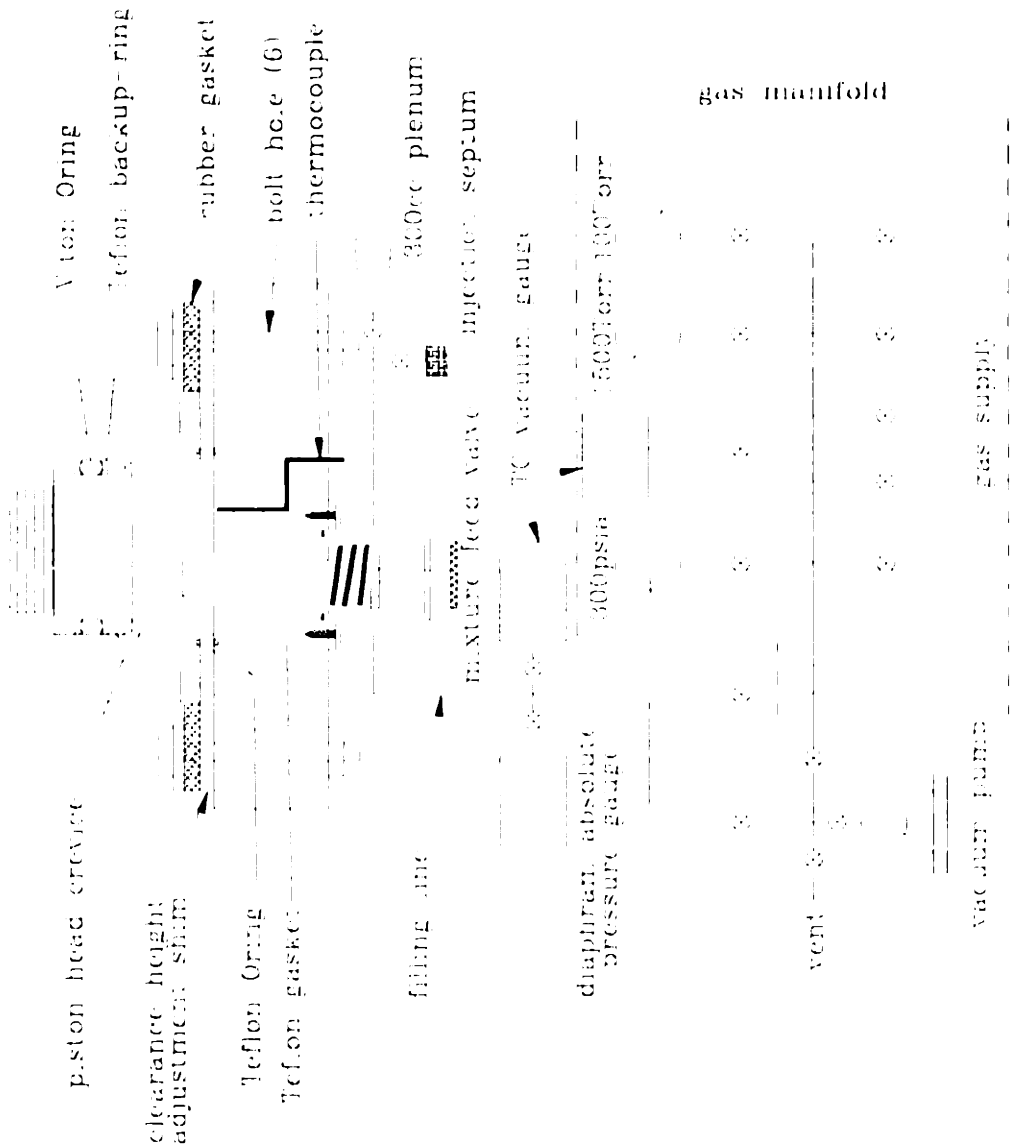

Figure 2.8 Test Chamber and Gas Handling System

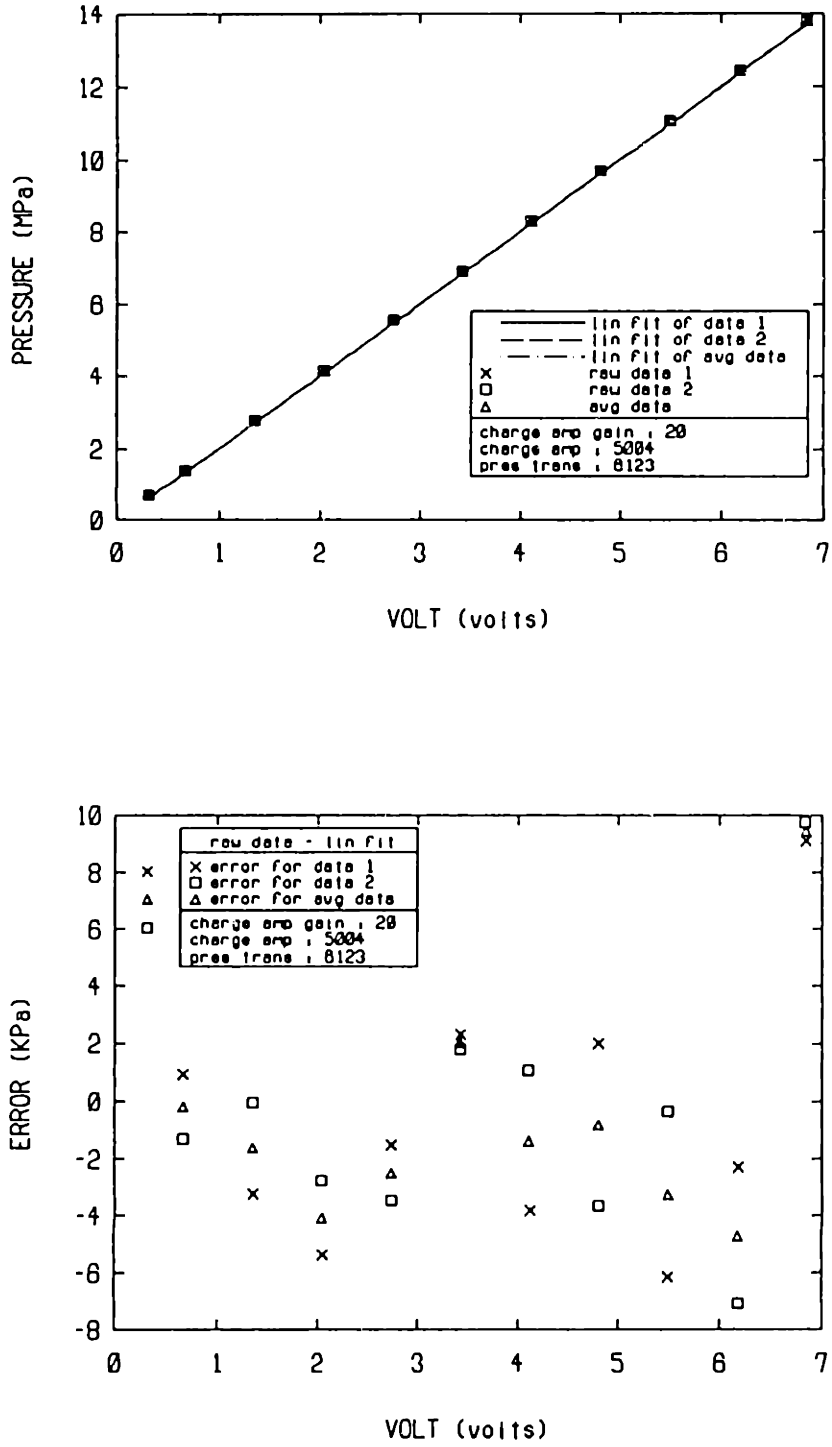

Figure 2.9 Dynamic Pressure Transducer Calibration

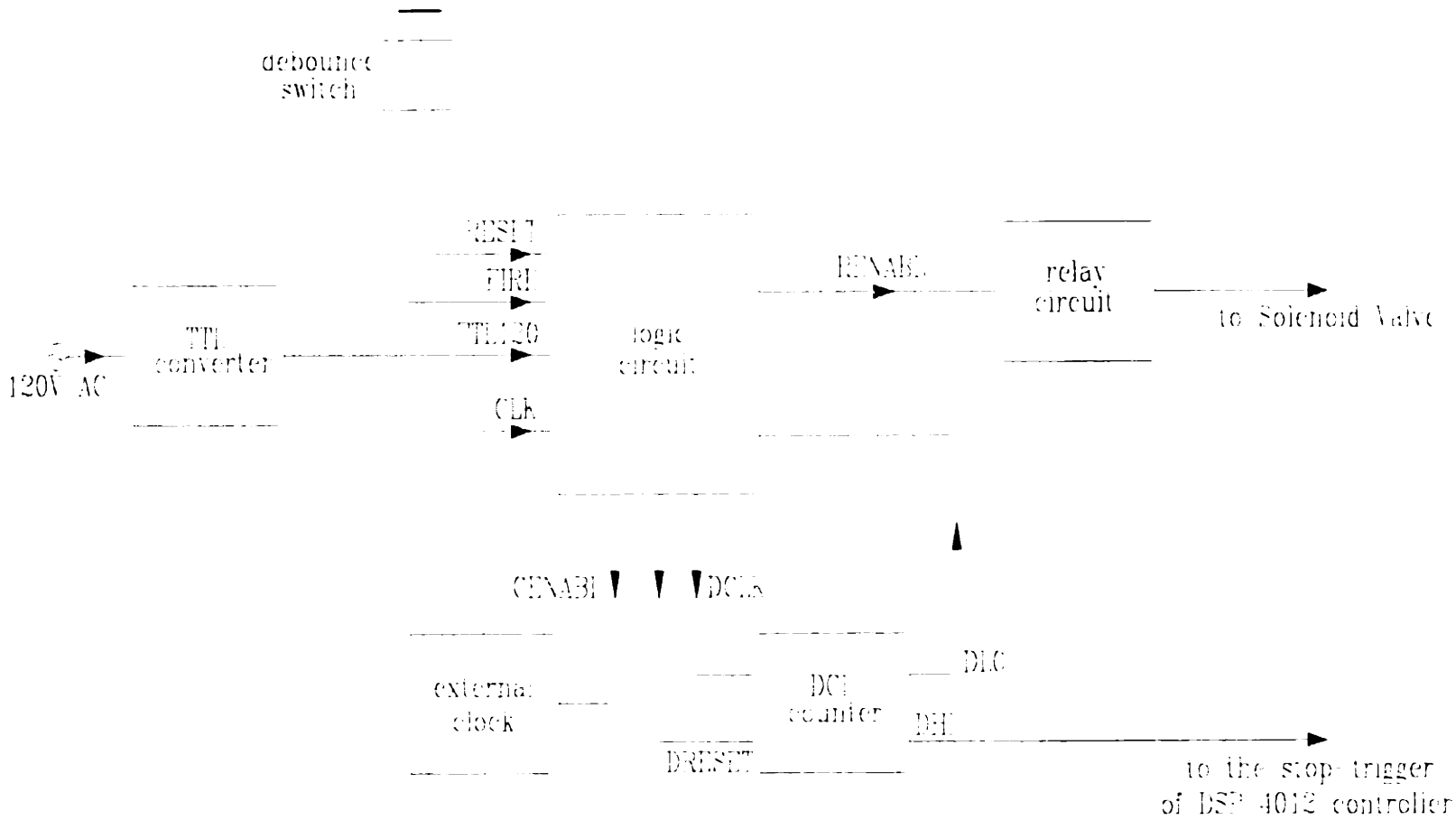

Figure 2.10 General Layout of Timing Circuit

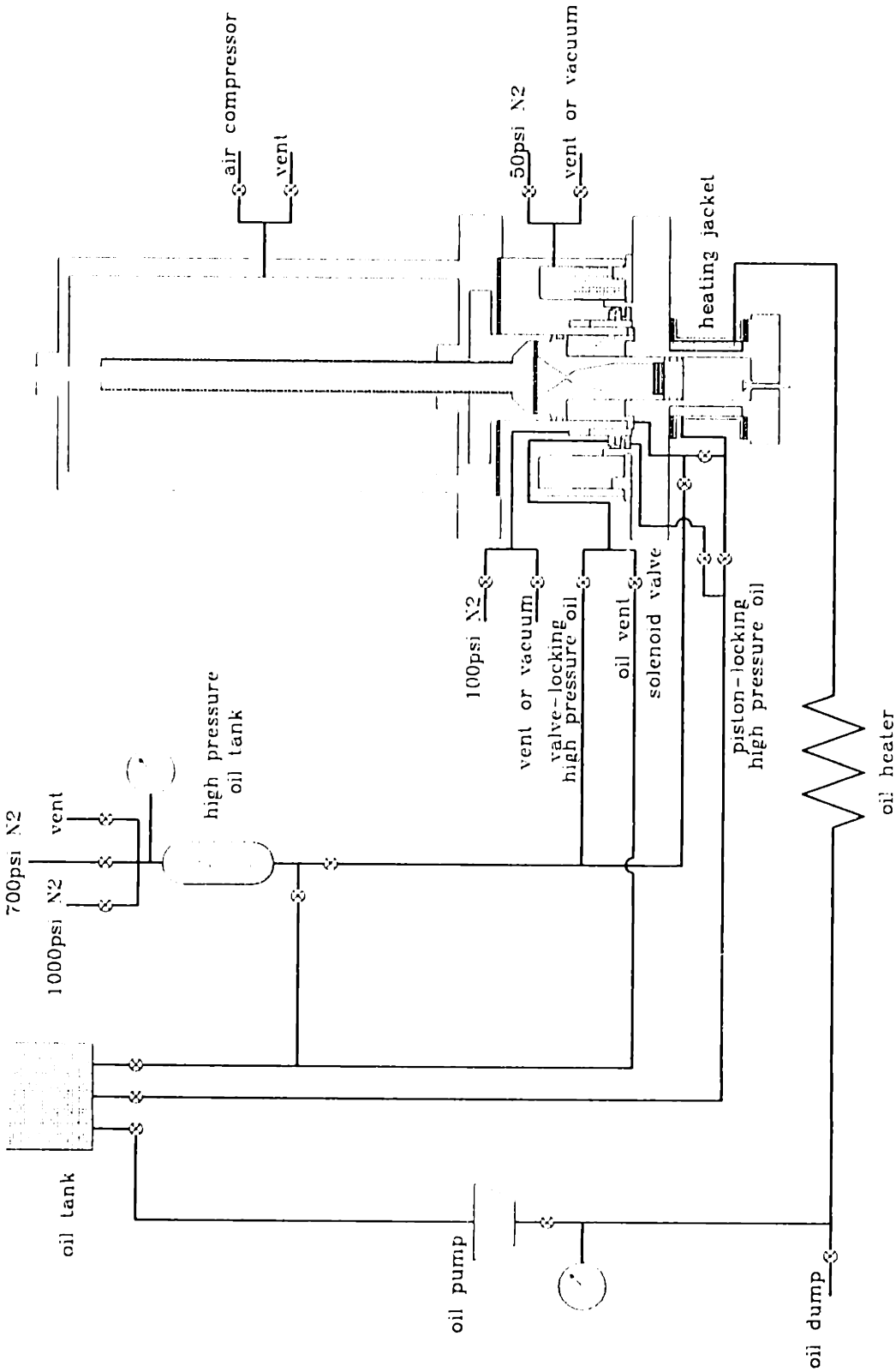

Figure 2.11 Oil Lines of RCM Plumbing

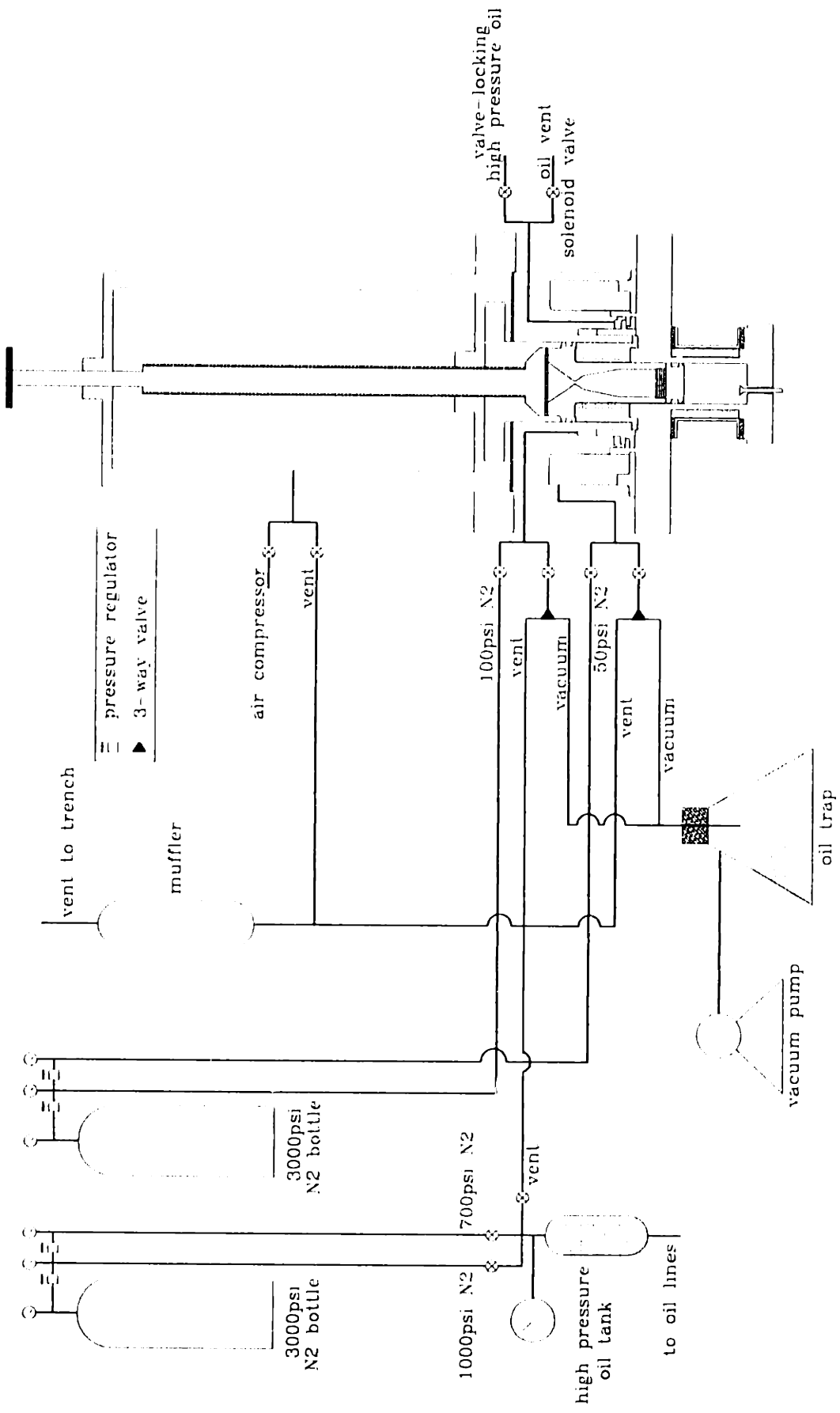

Figure 2.12 Gas Lines of RCM Plumbing

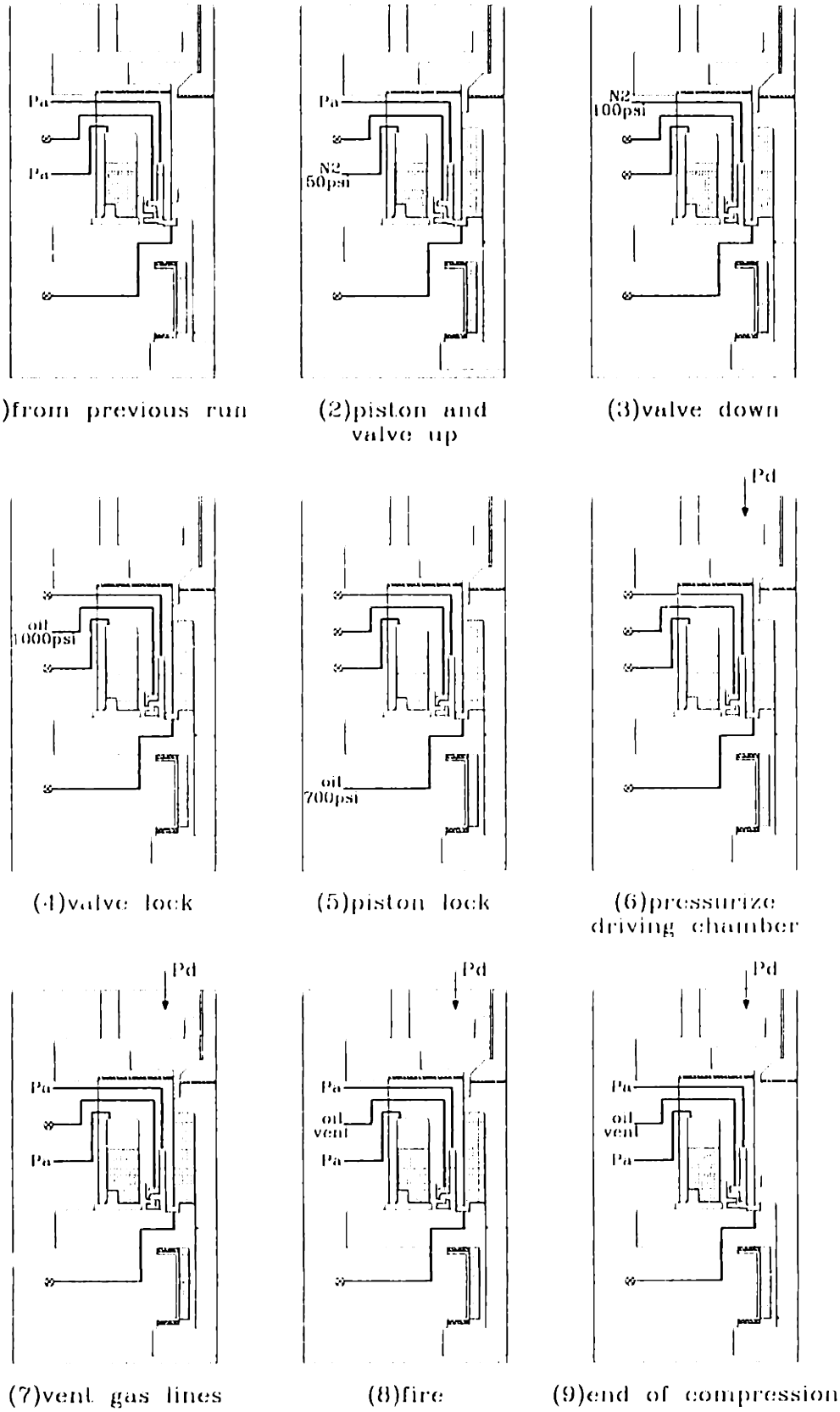

Figure 2.13 Operation Sequence of Current RCM

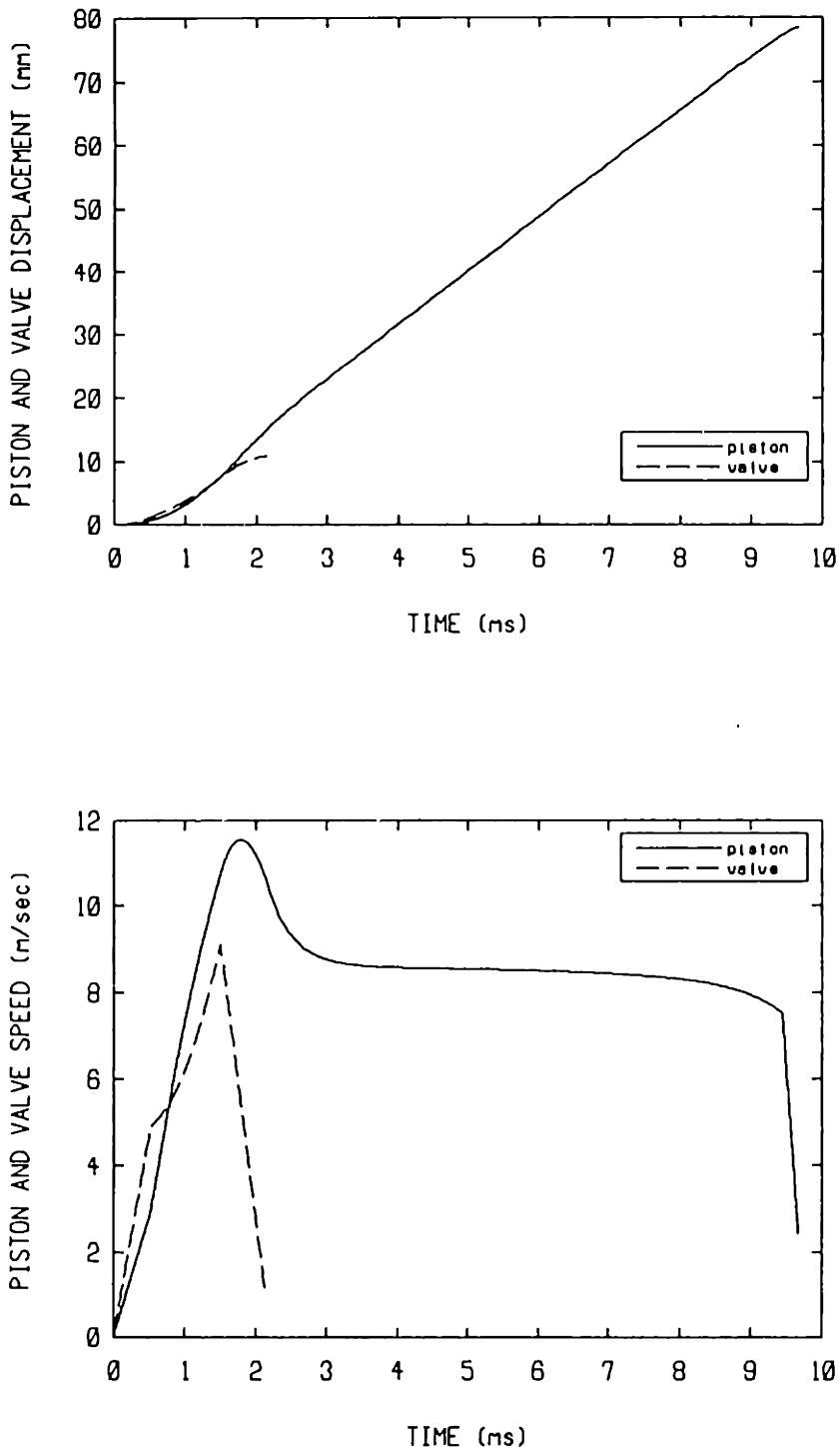

Figure 2.14 Simulation of Piston and Fast-acting-valve Dynamics : Driving Pressure=2.07 MPa, Stroke=7.84 cm, Clearance Height=0.6 cm, Speed Control Orifice Opening Area=6.81 cm^2, Piston Head with Crevice, C_{d3}=1, C_{d4}=1, k_1=0, k_2=0, k_3=0, Time 0 Shifted to Start of Compression

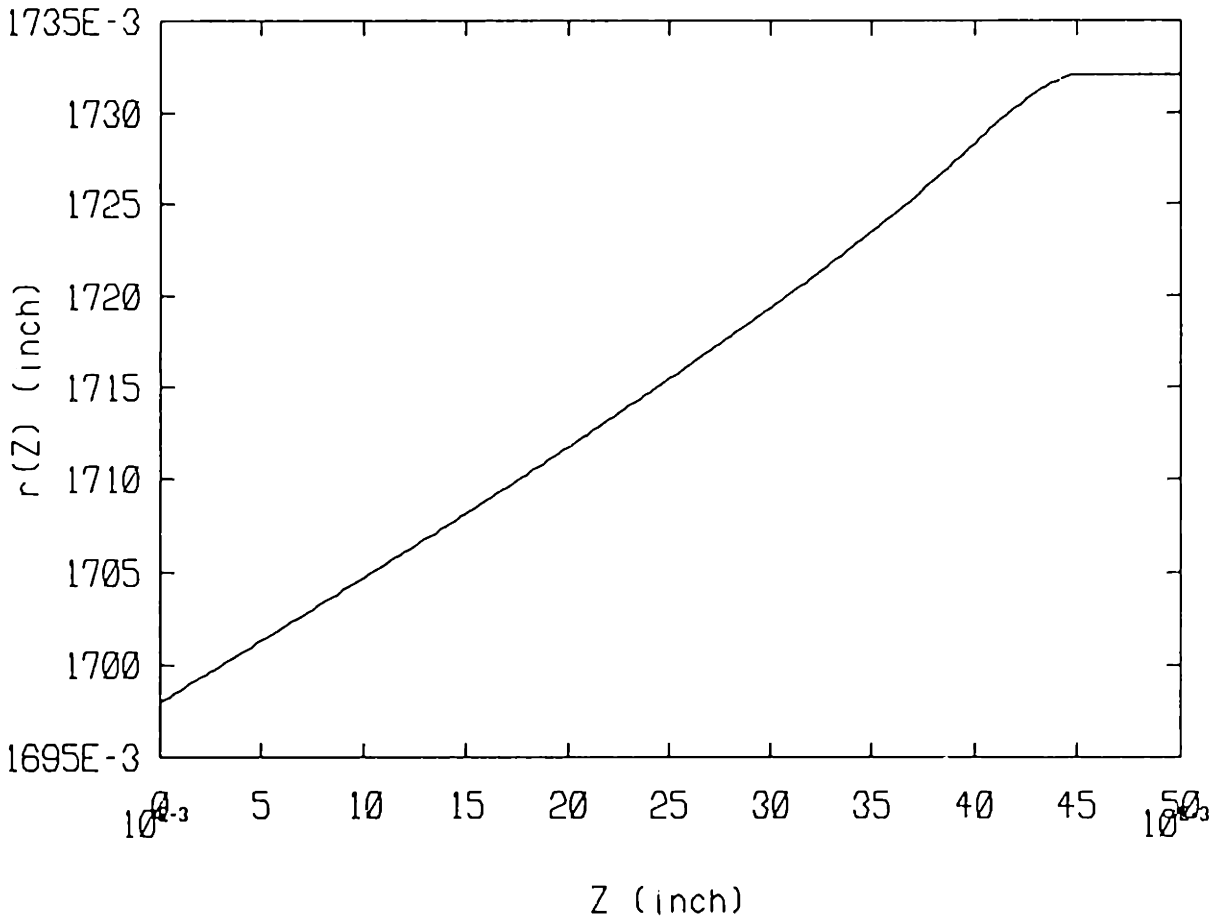

Figure 2.15 Optimal Piston Pin Shape : Z Measured from Pin Face, r Measured from RCM Center Line, lsp=0.05 inch=0.13 cm

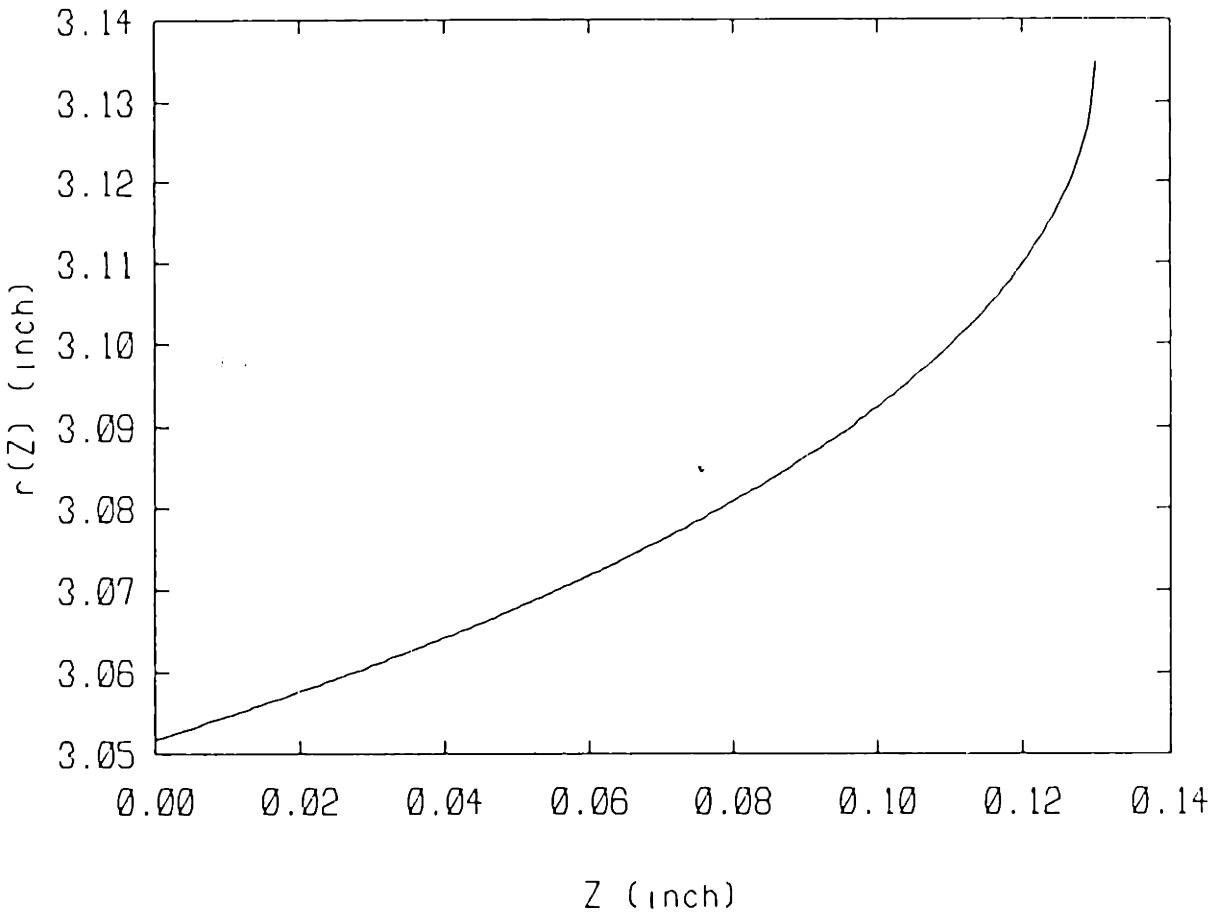

Figure 2.16 Optimal Valve Pin Shape : Z Measured from Pin Face, r Measured from RCM Center Line, lsv=0.13 inch

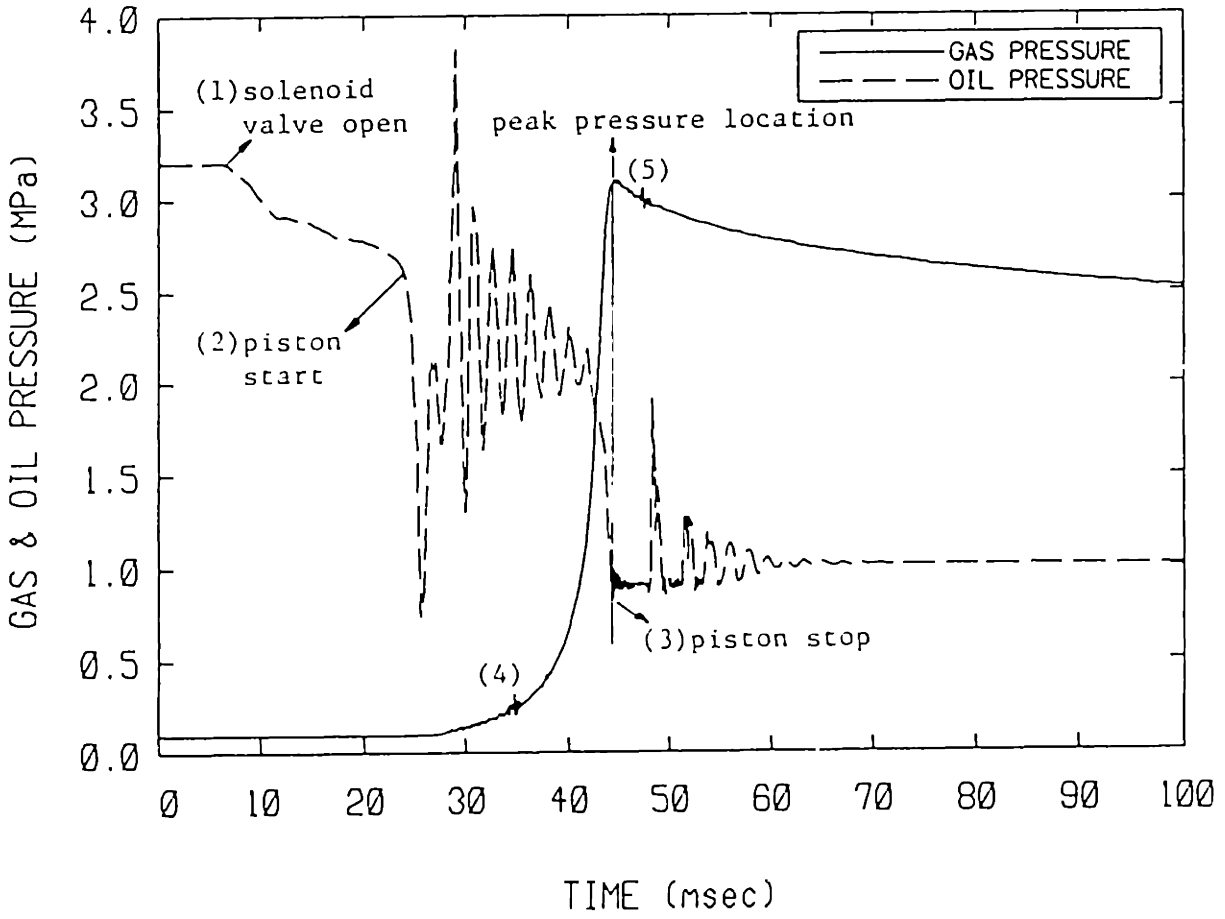

Figure 3.1 Typical Gas and Oil Pressure Records : Gas=N_2, P_i=720 torr, T_i=303 K, Driving Pressure=2.07 MPa, Stroke=7.84 cm, Clearance Height=0.6 cm, Speed Control Orifice Opening Area=6.81 cm^2, Piston Head with Crevice, Time 0 Shifted to Start of Experiment

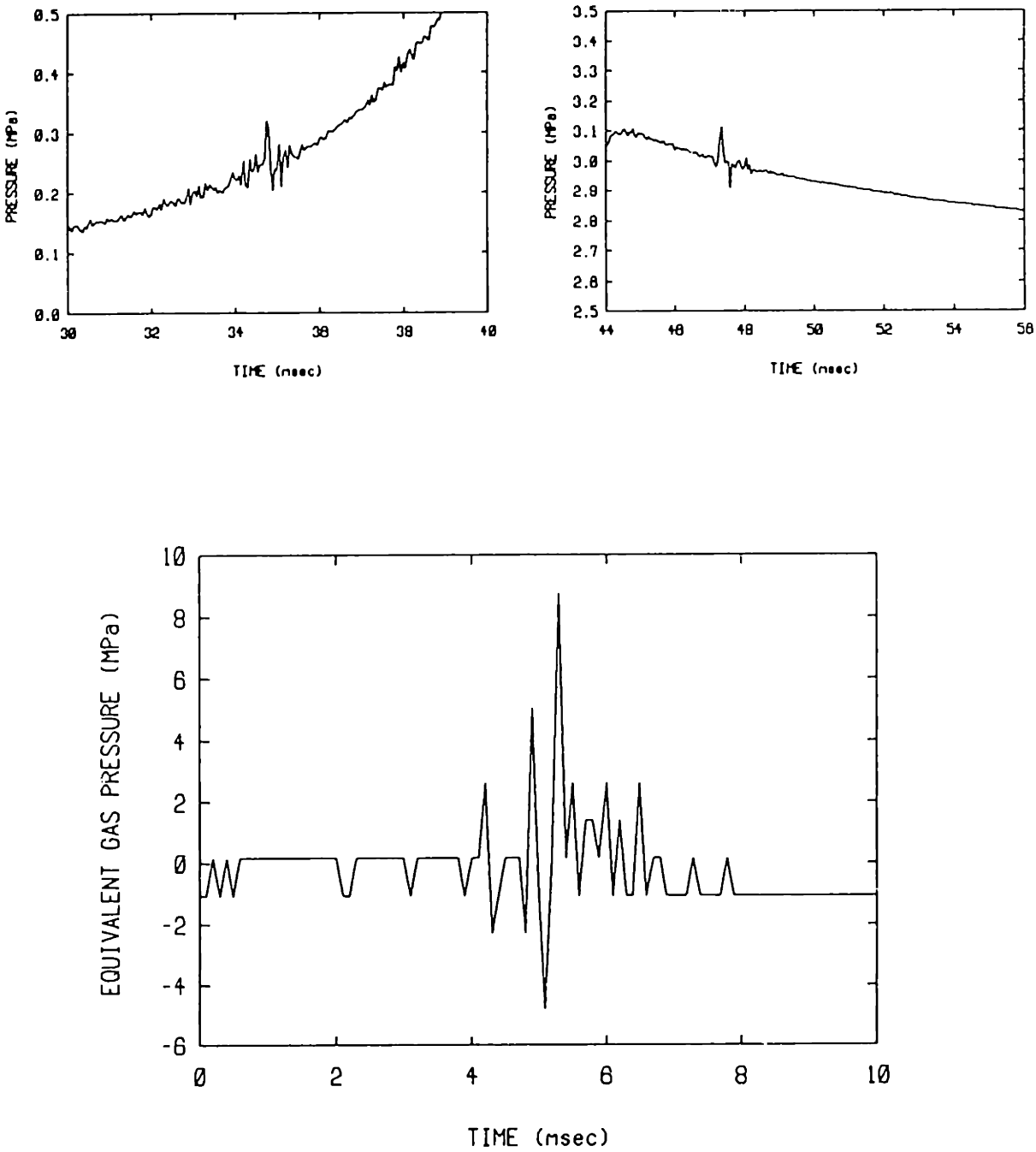

Figure 3.2 Mechanical Vibration Added to Gas Pressure : Top Left=Magnification of Location (4) in Fig. 3.1, Top Right=Magnification of Location (5) in Fig. 3.1, Bottom=Vibration Recorded from Gas Pressure Transducer When RCM Was Hit by a Hammer

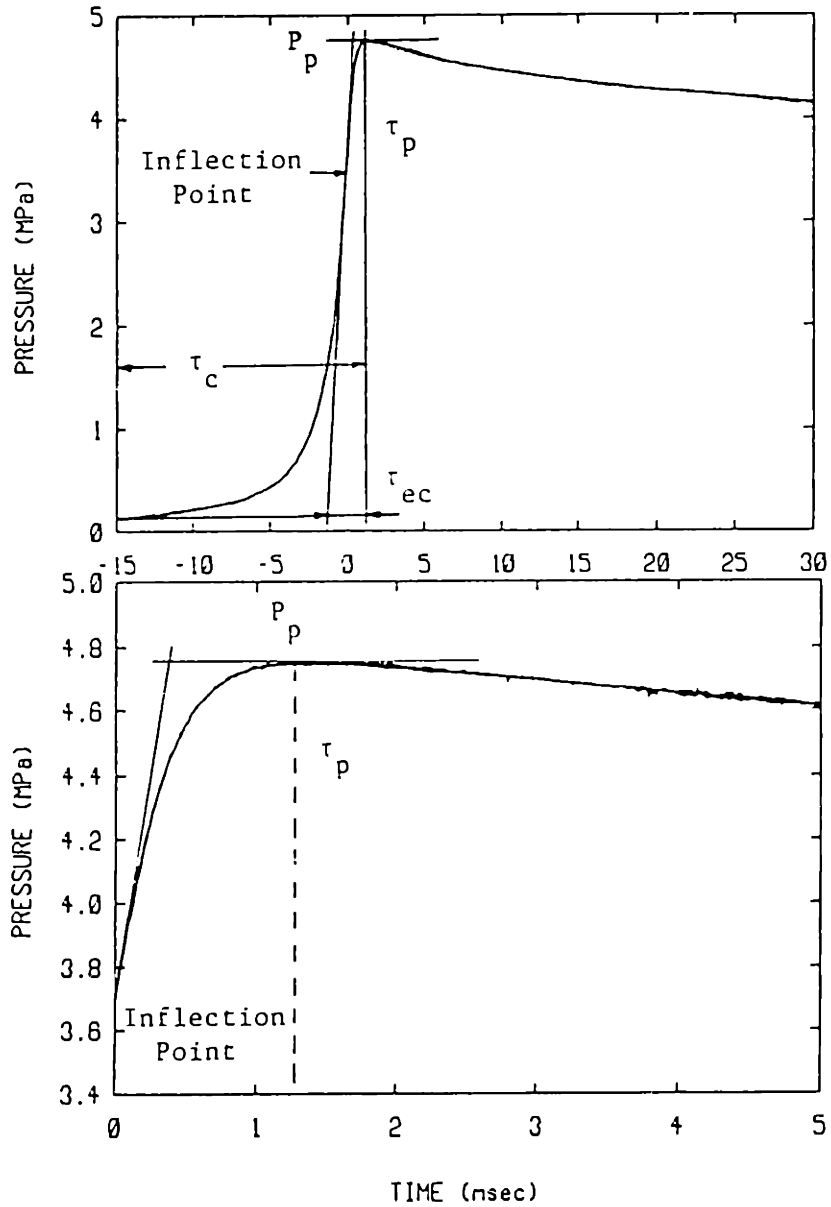

Figure 3.3 Typical Pressure Traces for Consecutive Runs with Pure N_2 at Identical Operating Conditions : P_i=1000 torr, T_i=294 K, Driving Pressure=2.07 MPa, Stroke=9.51 cm, Clearance Height=0.615 cm, Speed Control Orifice Opening Area=10.58 cm^2, Piston Head with Crevice, Time 0 Shifted to Steepest Slope

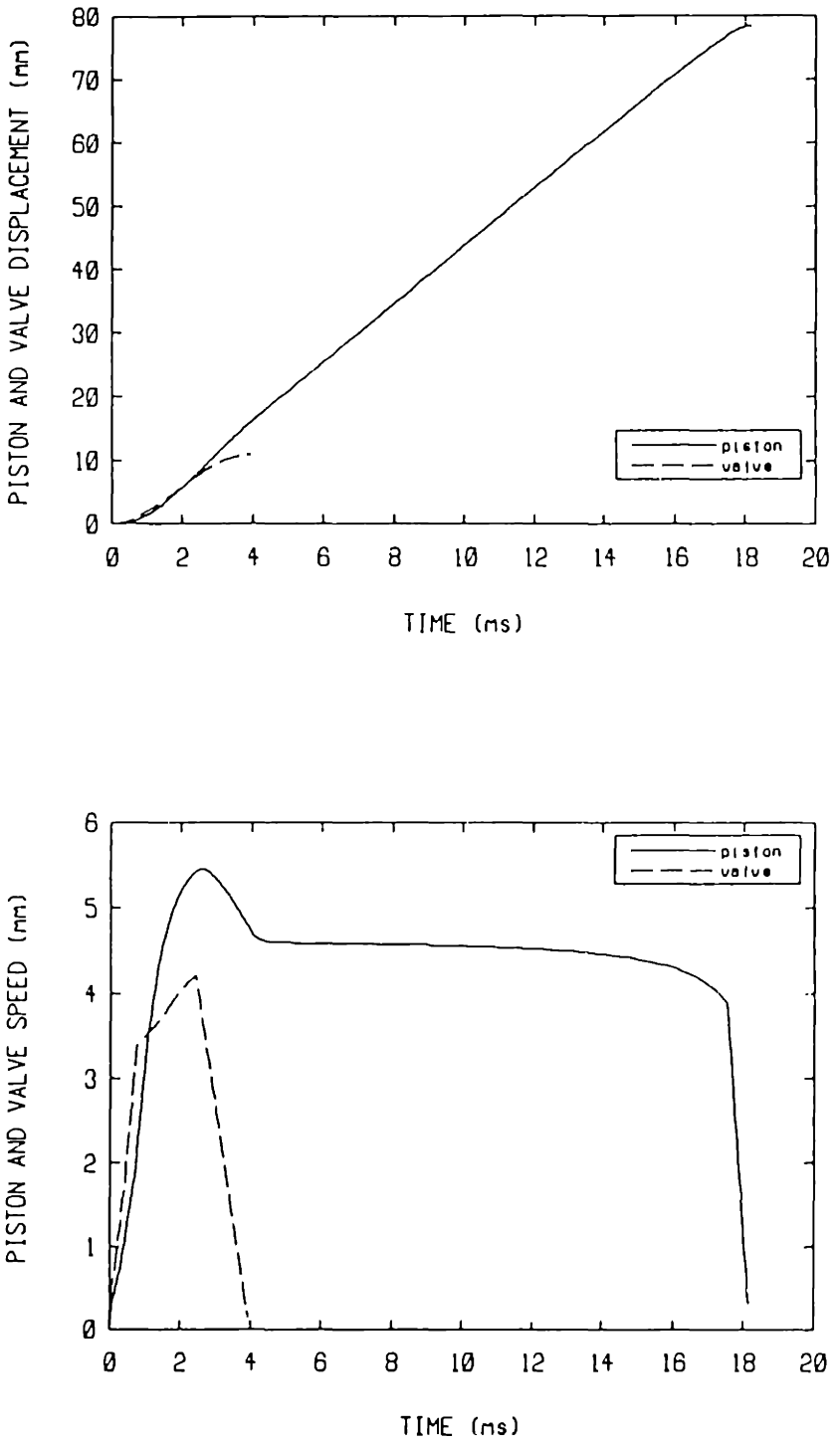

Figure 3.4 Piston and Fast-acting-valve Dynamics : Gas=N_2, P_1=720 torr, T_1=303 K, Driving Pressure=2.07 MPa, Stroke=7.84 cm, Clearance Height=0.6 cm, Speed Control Orifice Opening Area=6.81 cm^2, Piston Head with Crevice, C_{d3}=.65, C_{d4}=.75, k_1=150, k_2=.8x10^{-3}, k_3=50, Time 0 Shifted to Start of Compression

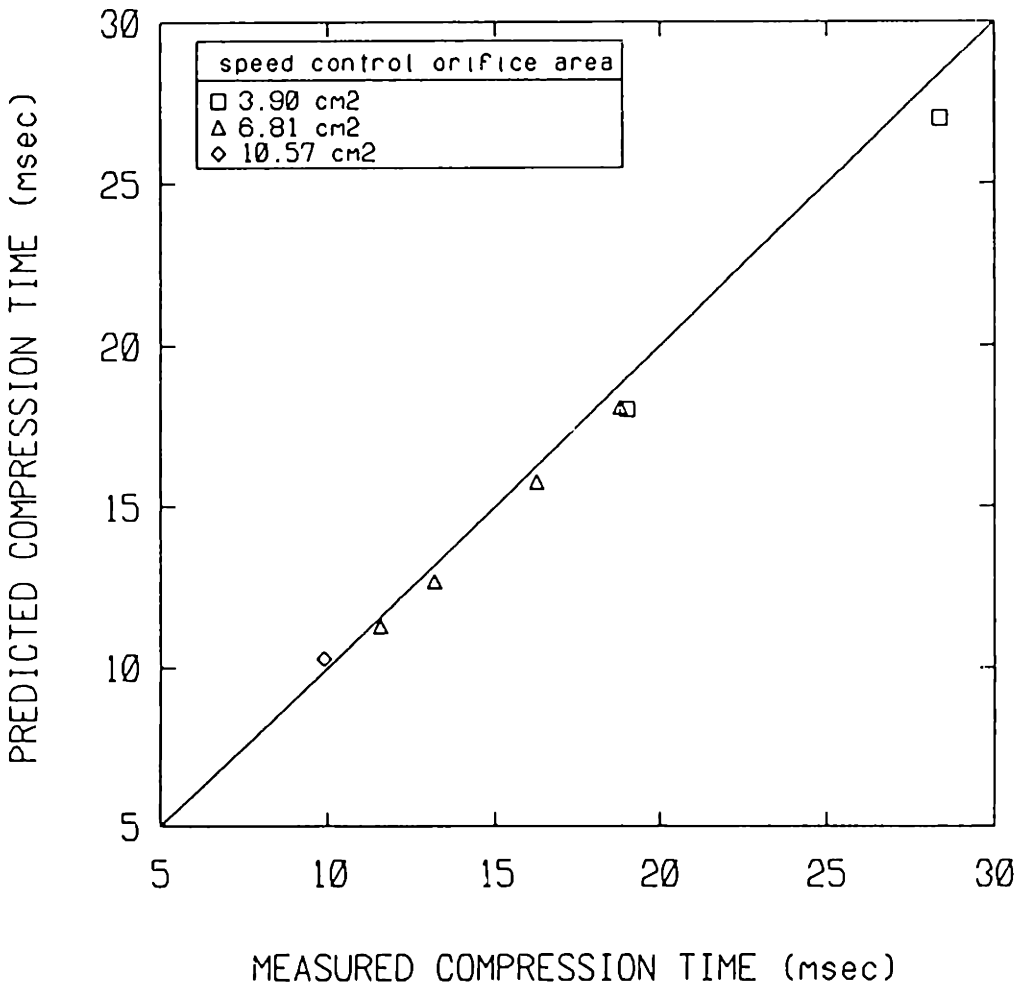

Figure 3.5 Comparison of Measured Compression Times with Predicted Compression Times from RCM Dynamic Simulation : C_{d3}=.65, C_{d4}=.75, k_1=150, k_2=.8x10^{-3}, k_3=50

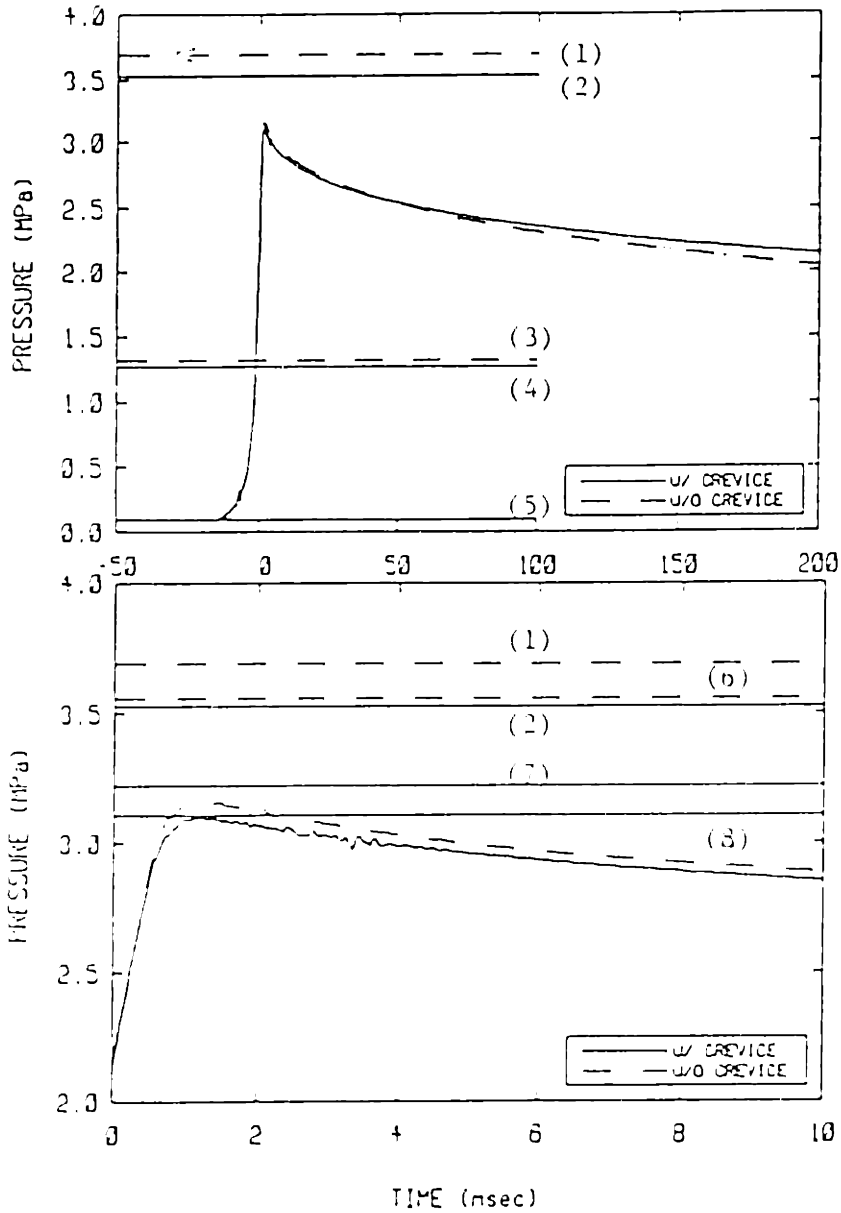

Figure 3.6 Comparison of Inert Gas Pressure Traces for Piston Head with and without Crevice : Initial Temperature=298 K, Crevice Volume=0.527 cm^3, Stroke=7.74 cm, Clearance Height=0.60 cm, Driving Pressure=2.07 MPa, Speed Control Orifice Area=6.81 cm^2, Measured Peak Pressure for Piston without Crevice=3.16 MPa, Measured Peak Pressure for Piston with Crevice=3.10 MPa, Compression Ratio for Piston without Crevice=13.9, Compression Ratio for Piston with Crevice=13.4, Time 0 Shifted to Steepest Slope, (1) Geometric Isentropic Pressure for Piston Head without Crevice=3.69 MPa, (2) Geometric Isentropic Pressure for Piston Head with Crevice=3.53 MPa, (3) Isothermal Pressure for Piston Head without Crevice=1.32 MPa, (4) Isothermal Pressure for Piston Head with Crevice=1.27 MPa, (5) Initial Pressure=95 KPa, (6) Isentropic Pressure assuming Laminar Boundary Layer for Piston without Crevice=3.56 MPa, (7) Isentropic Pressure assuming Isothermal Crevice for Piston with Crevice=3.22 MPa, (8) Isentropic Pressure assuming Isothermal Crevice and Laminar Boundary Layer for Piston with Crevice=3.11 MPa

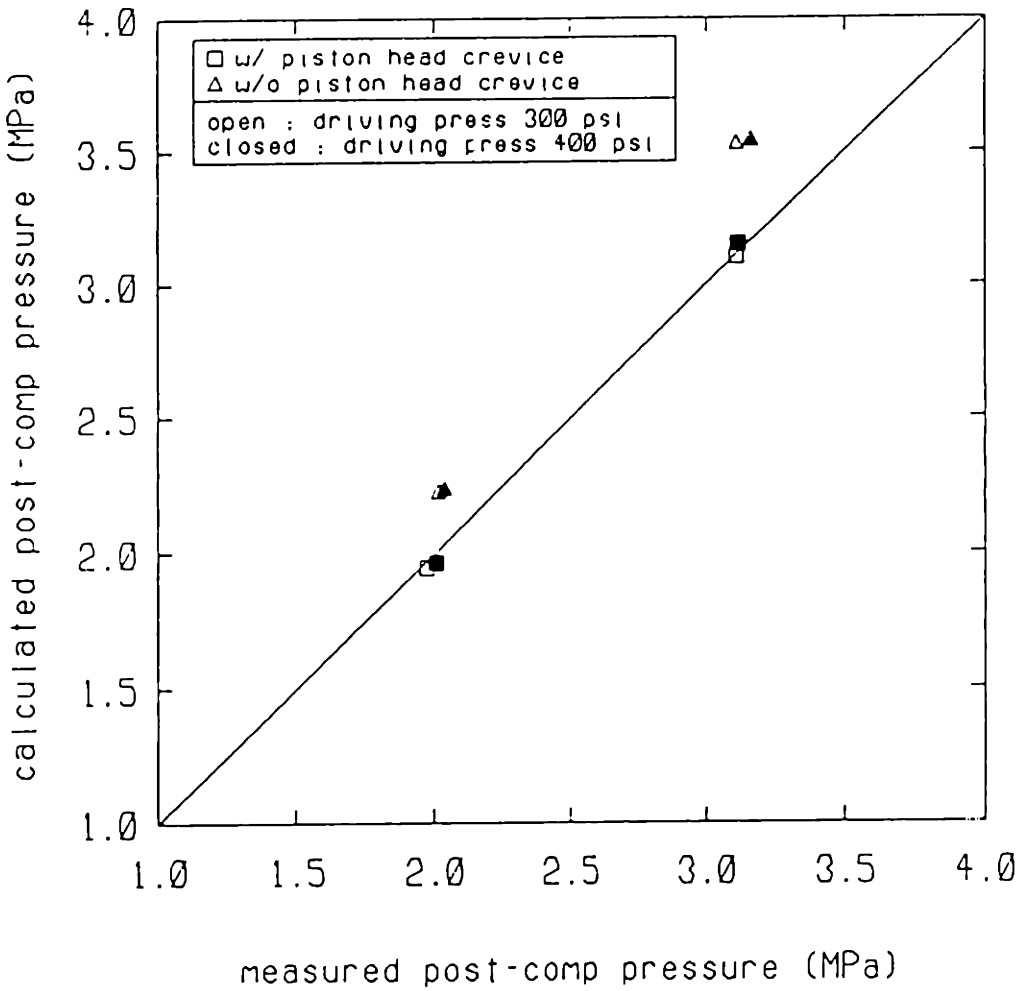

Figure 3.7 Comparison of Measured Post-compression Pressure with Calculated Post-compression Pressure from Laminar Theory : Gas=N_2, Clearance Height=0.6 cm, Speed Control Orifice Area=6.81 cm^2

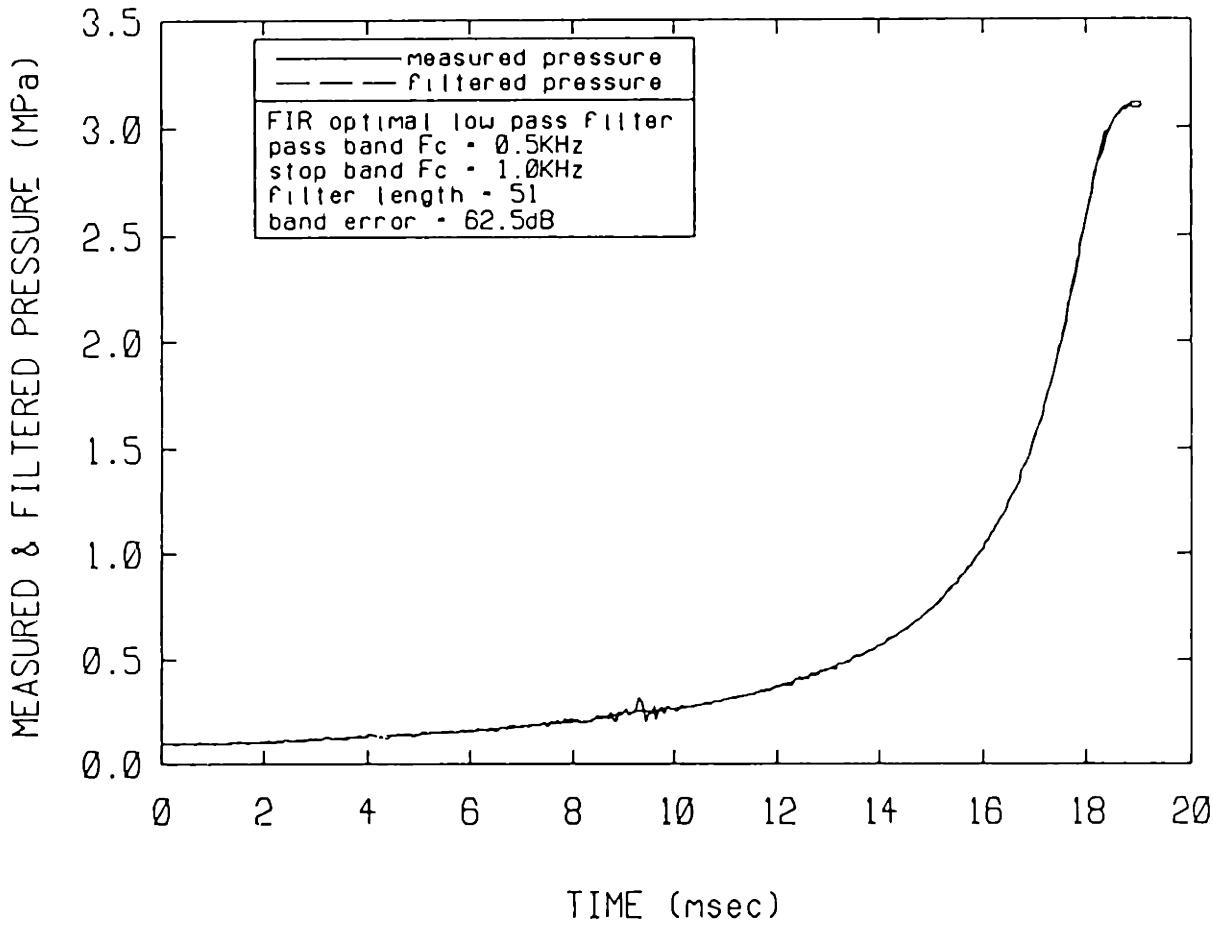

Figure 3.8 Raw Pressure and Filtered Pressure : FIR Optimal Low Pass Filter, Pass Band Cut-off Frequency=0.5 KHz, Stop Band Cut-off Frequency=1.0 KHz, Filter Length=51, Band Error=62.5 dB, Gas=N_2, P_i=720 torr, T_i=303 K, Driving Pressure=2.07 MPa, Stroke=7.84 cm, Clearance Height=0.6 cm, Speed Control Orifice Opening Area=6.81 cm^2, Piston Head with Crevice, Time 0 Shifted to Start of Compression

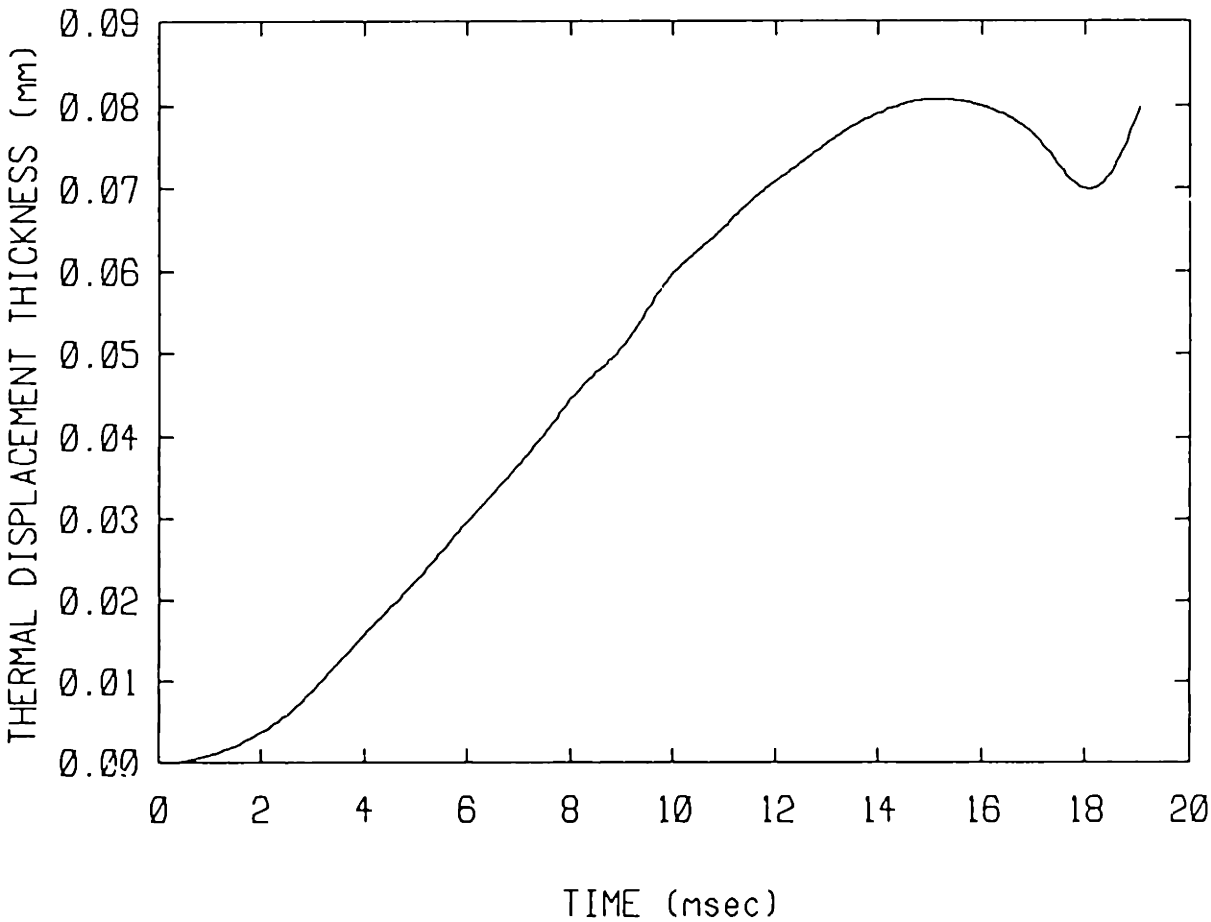

Figure 3.9 Thermal Displacement Thickness : Gas=N_2, P_1=720 torr, T_1=303 K, Driving Pressure=2.07 MPa, Stroke=7.84 cm, Clearance Height=0.6 cm, Speed Control Orifice Opening Area=6.81 cm^2, Piston Head with Crevice, α_o=2.253x10^{-5} m^2/s, Time 0 Shifted to Start of Compression

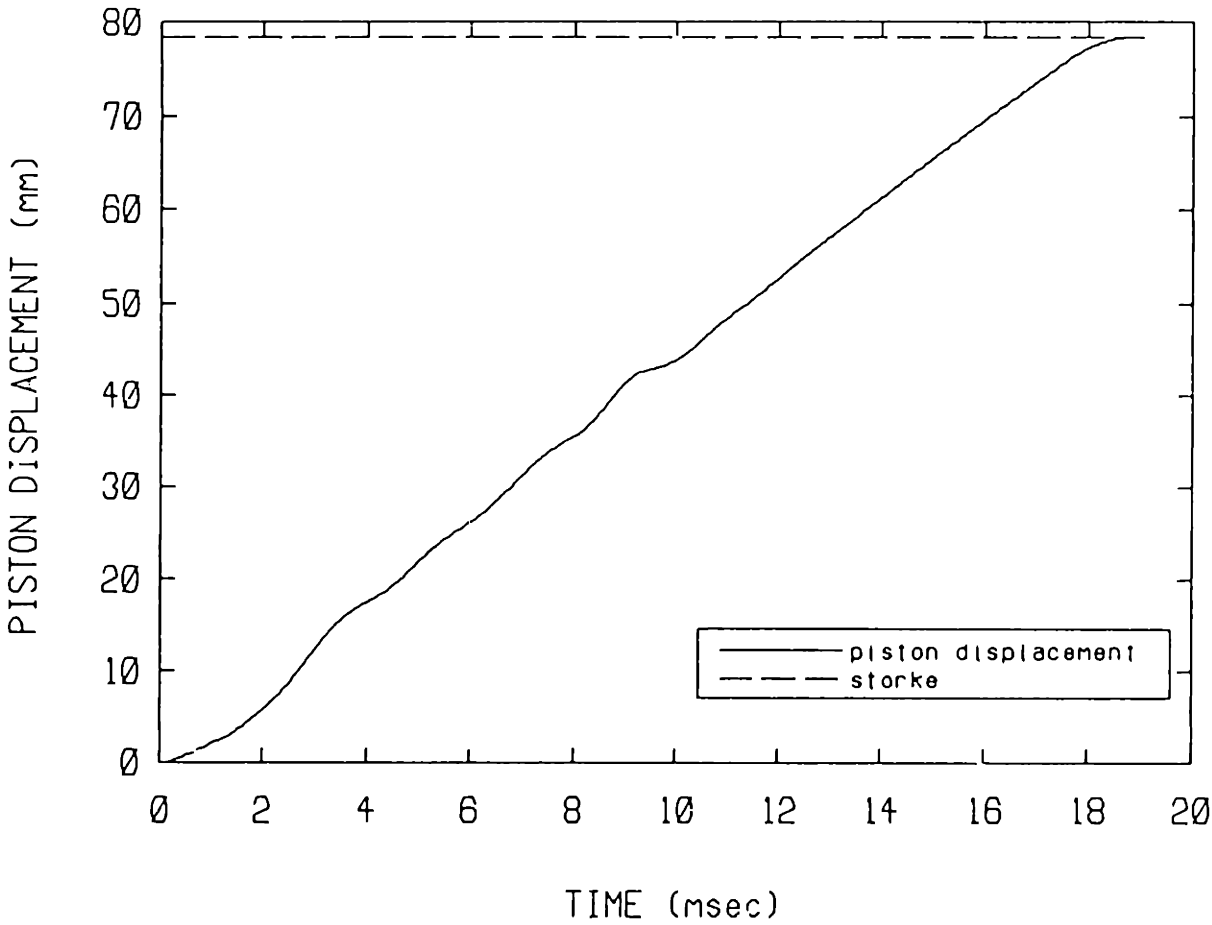

Figure 3.10 Piston Displacement Obtained from Heat Transfer Analysis : Gas=N_2, P_i=720 torr, T_i=303 K, Driving Pressure=2.07 MPa, Stroke=7.84 cm, Clearance Height=0.6 cm, Speed Control Orifice Opening Area=6.81 cm^2, Piston Head with Crevice, Time 0 Shifted to Start of Compression

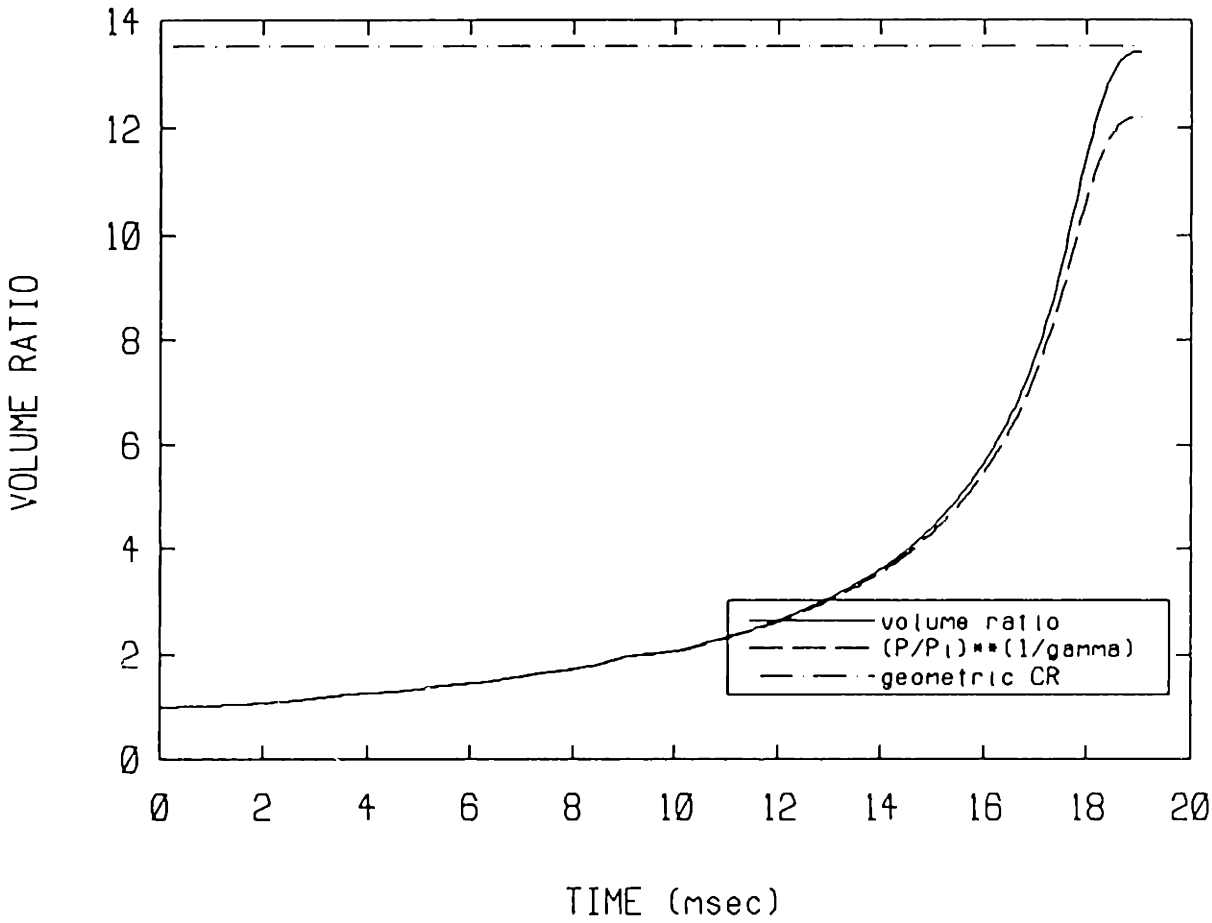

Figure 3.11 Volume Ratio Obtained from Heat Transfer Analysis : Gas=N_2, P_i=720 torr, T_i=303 K, Driving Pressure=2.07 MPa, Stroke=7.84 cm, Clearance Height=0.6 cm, Speed Control Orifice Opening Area=6.81 cm^2, Piston Head with Crevice, Time 0 Shifted to Start of Compression

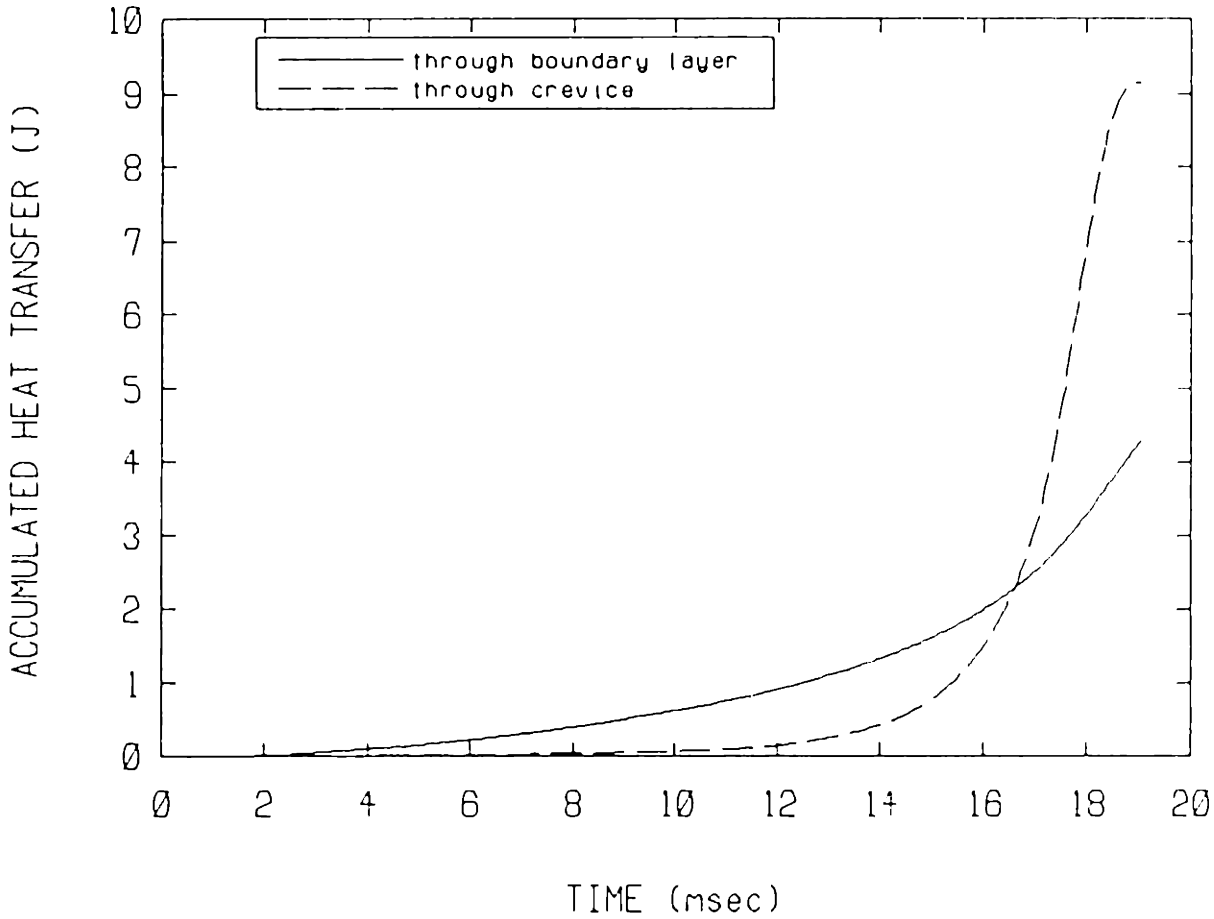

Figure 3.12 Accumulated Heat Transfer Obtained from Heat Transfer Analysis : Gas=N_2, P_i=720 torr, T_i=303 K, Driving Pressure=2.07 MPa, Stroke=7.84 cm, Clearance Height=0.6 cm, Speed Control Orifice Opening Area=6.81 cm^2, Piston Head with Crevice, Time 0 Shifted to Start of Compression

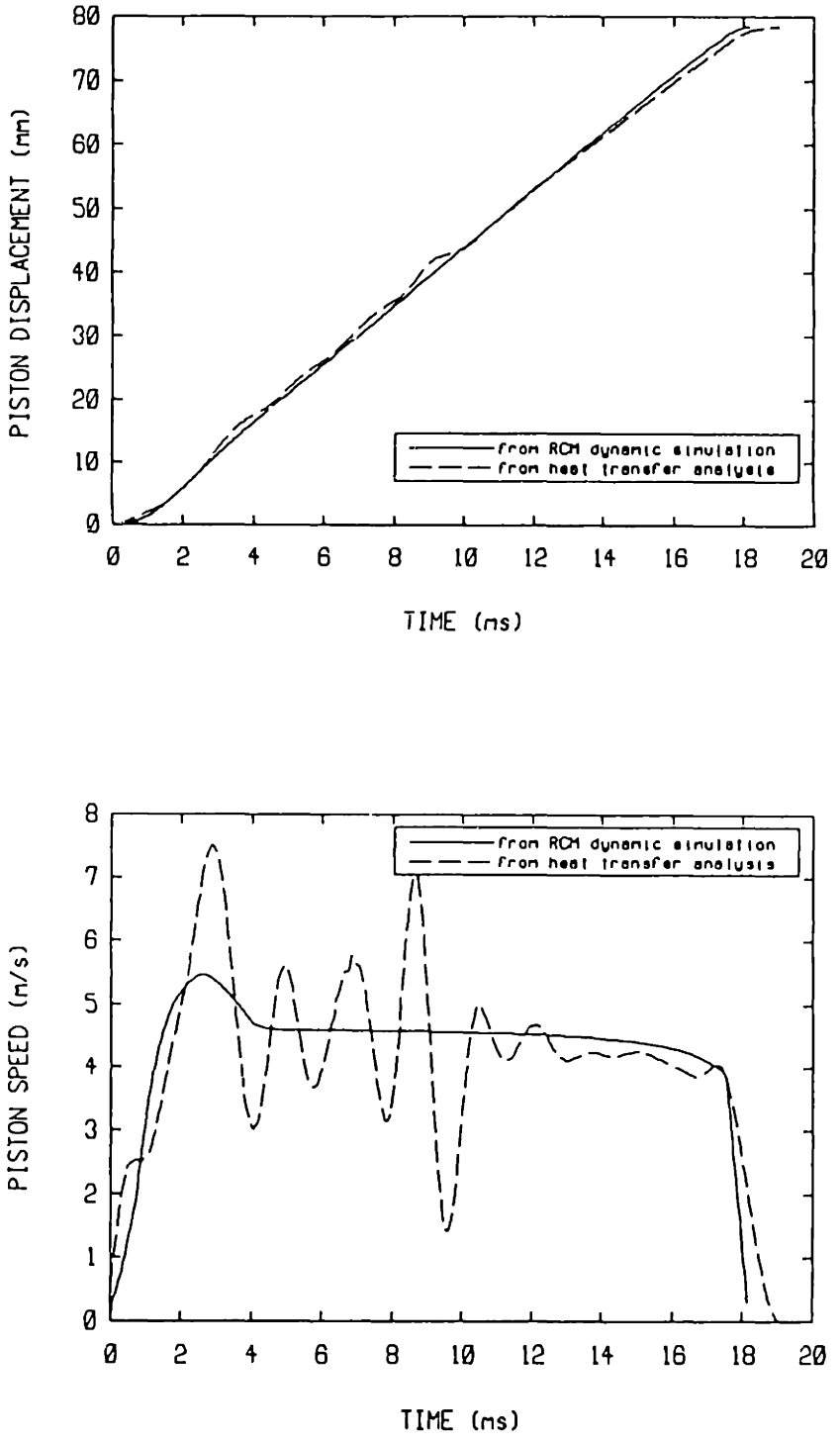

Figure 3.13 Piston Motions from RCM Dynamic Simulation and from Heat Transfer Analysis : Gas=N_2, P_i=720 torr, T_i=303 K, Driving Pressure=2.07 MPa, Stroke=7.84 cm, Clearance Height=0.6cm, Speed Control Orifice Opening Area=6.81 cm^2, Piston Head with Crevice, Time 0 Shifted to Start of Compression

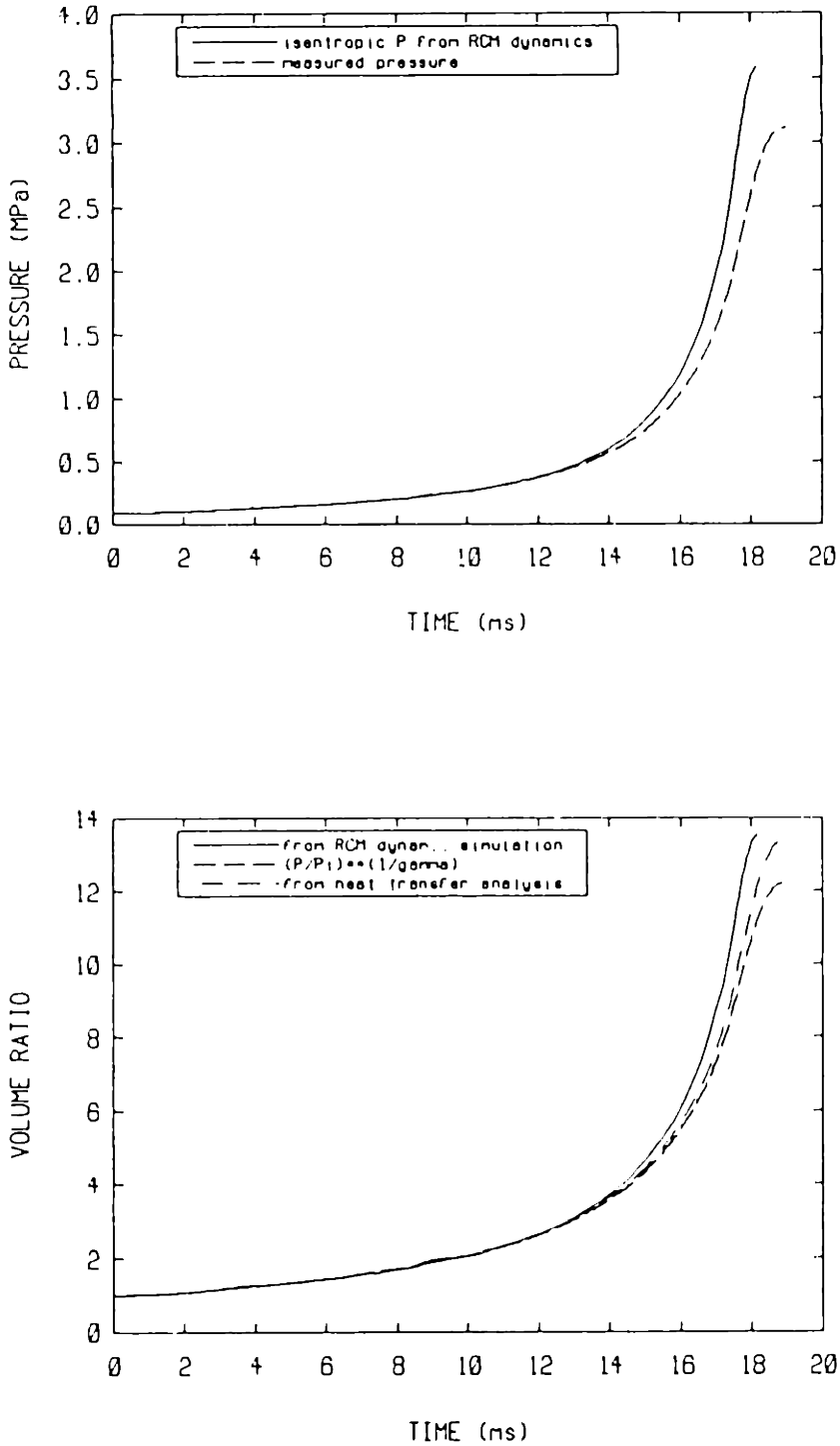

Figure 3.14 Pressure and Volume Ratio from RCM Dynamic Simulation and from Heat Transfer Analysis : Gas=N_2, P_i=720 torr, T_i=303 K, Driving Pressure=2.07 MPa, Stroke=7.84 cm, Clearance Height=0.6 cm, Speed Control Orifice Opening Area=6.81 cm^2, Piston Head with Crevice, Time 0 Shifted to Start of Compression

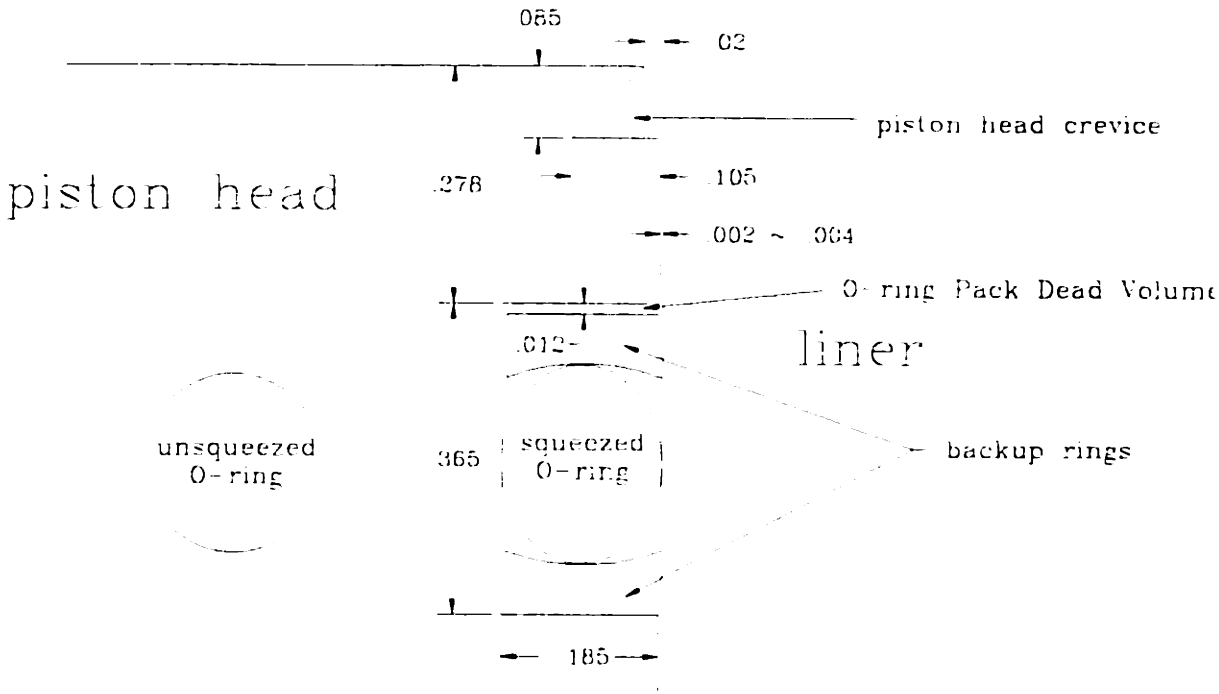

Liner Radius = 1.000 - .001 ~ .002 in
Piston Radius = 1.000 - .001 ~ .002 in
Piston Head Crevice Volume = 3.22E-2 in3
O-ring Pack Dead Volume = 1.53E-2 in3
(assumed the cross-section of compressed O-ring is an ellipse)

Figure 3.15 O-ring Pack and Dead Volume

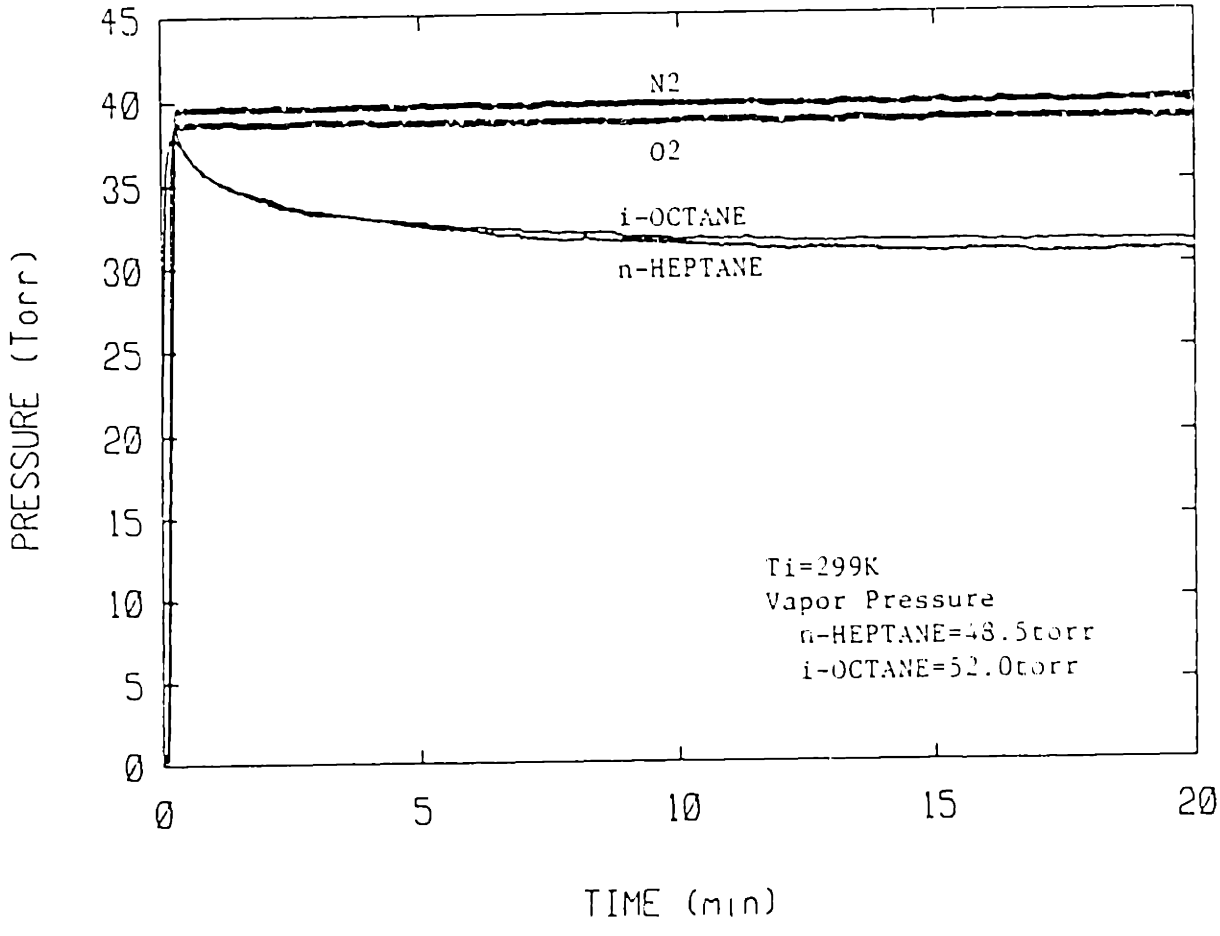

Figure 4.1 Pressure in Test Chamber and 300 cc Plenum as a Function of Time after Admission of i-C_8H_{18}, n-C_7H_{16}, N_2, and O_2 : Test Chamber Volume=205 cc, Plenum+Line Volume=345 cc, Amount of Fuel Injected=0.25 cc

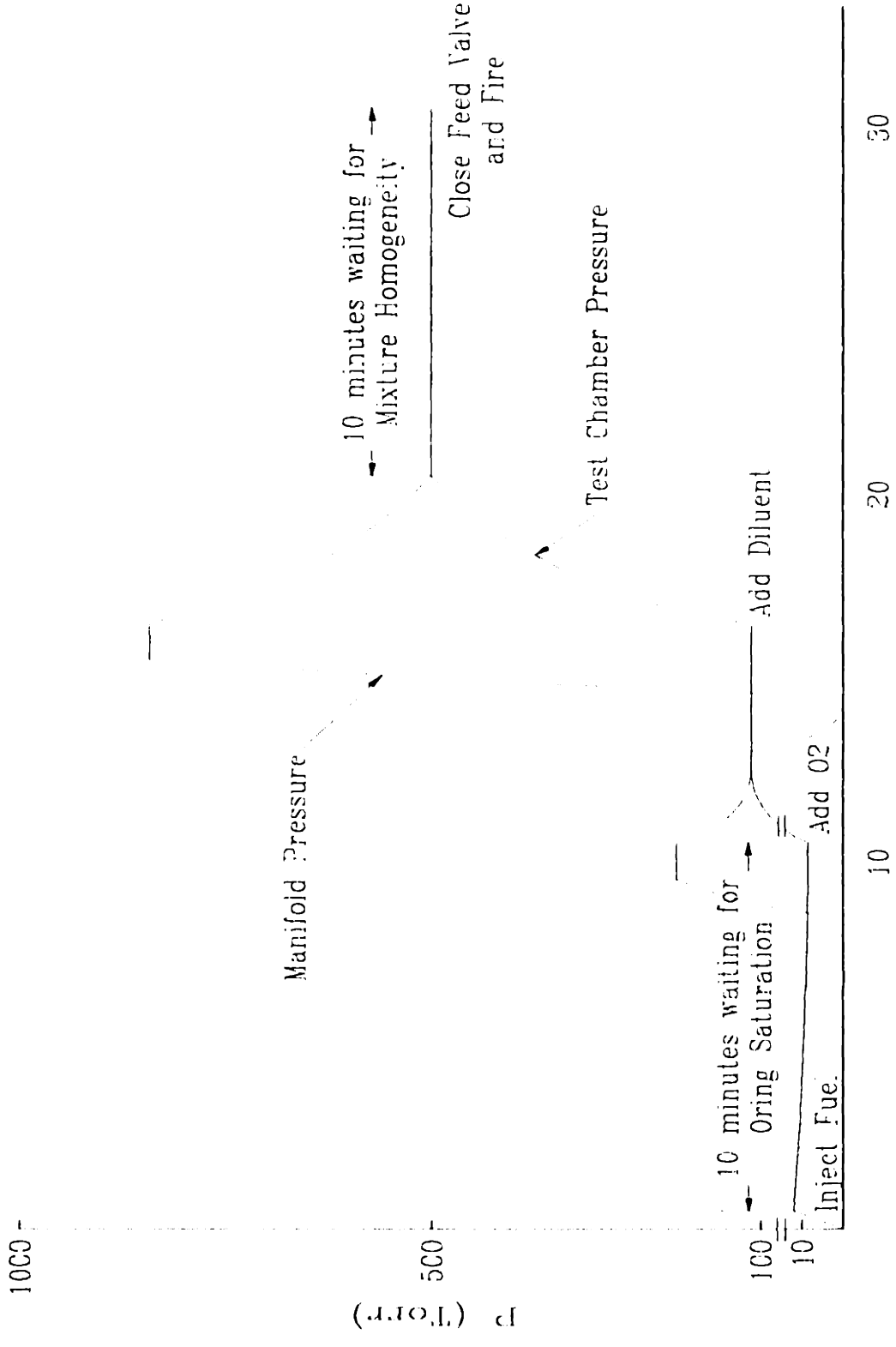

Figure 4.2 Primary Reference Fuel Mixture Feeding Procedure

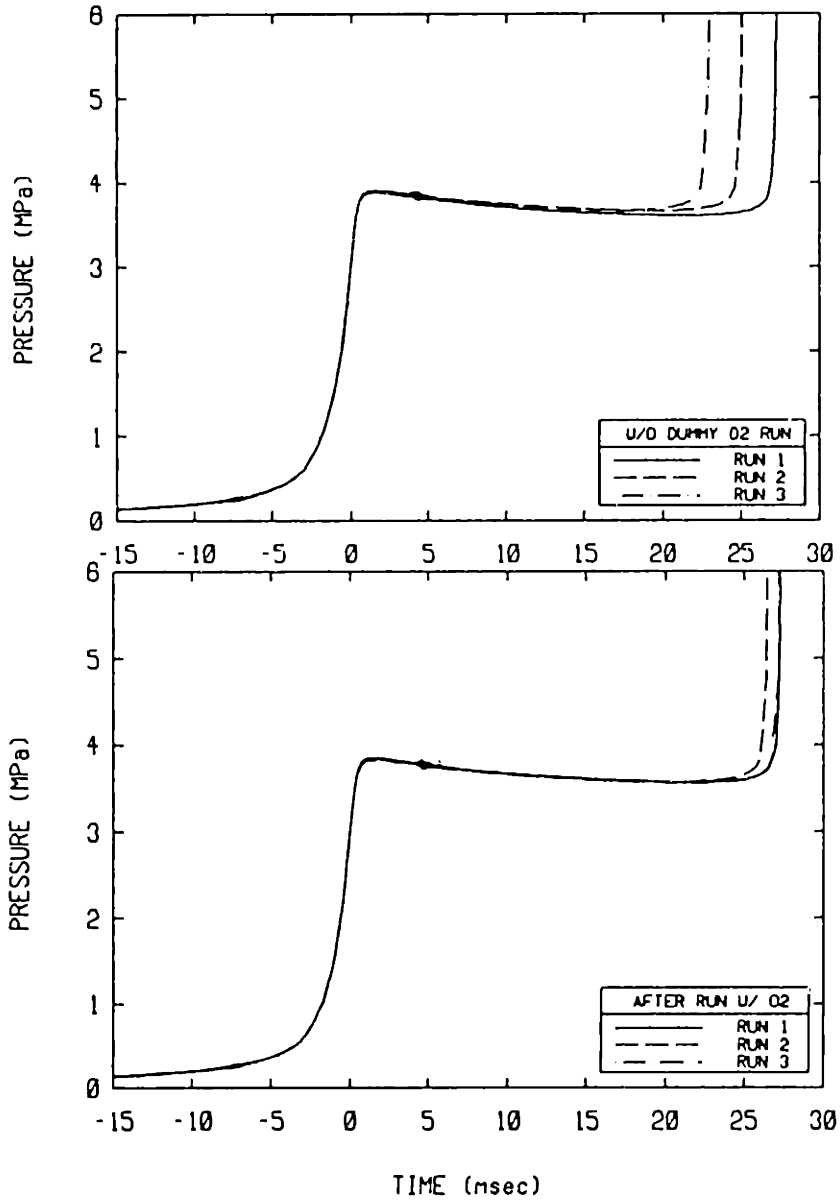

Figure 4.3 Effect of Preceding Pure O_2 Run on the Repeatability of Primary Reference Fuel Experiment : Equivalence Ratio=1, N_2/O_2 Ratio=3.77, P_i=1000 torr, T_i=293 K, CR=15.8, Time 0 Shifted to Steepest Slope

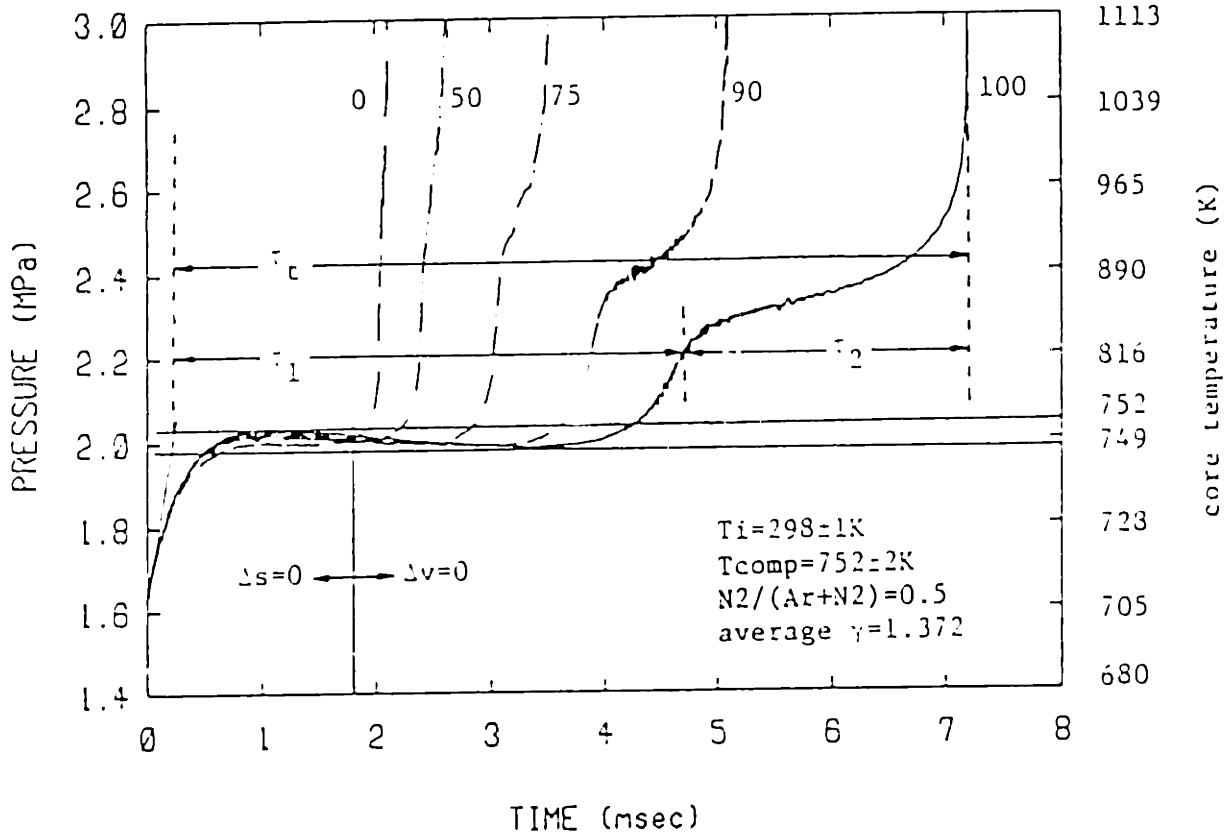

Figure 4.4 Pressure Records of Five Primary Reference Fuel Mixtures at P_i=500 torr : Equivalence Ratio=1, Diluents=N_2+Argon, Diluents/O_2 Ratio=3.77, N_2/Diluents=0.5, CR=15.8, Time 0 Shifted to Steepest Slope

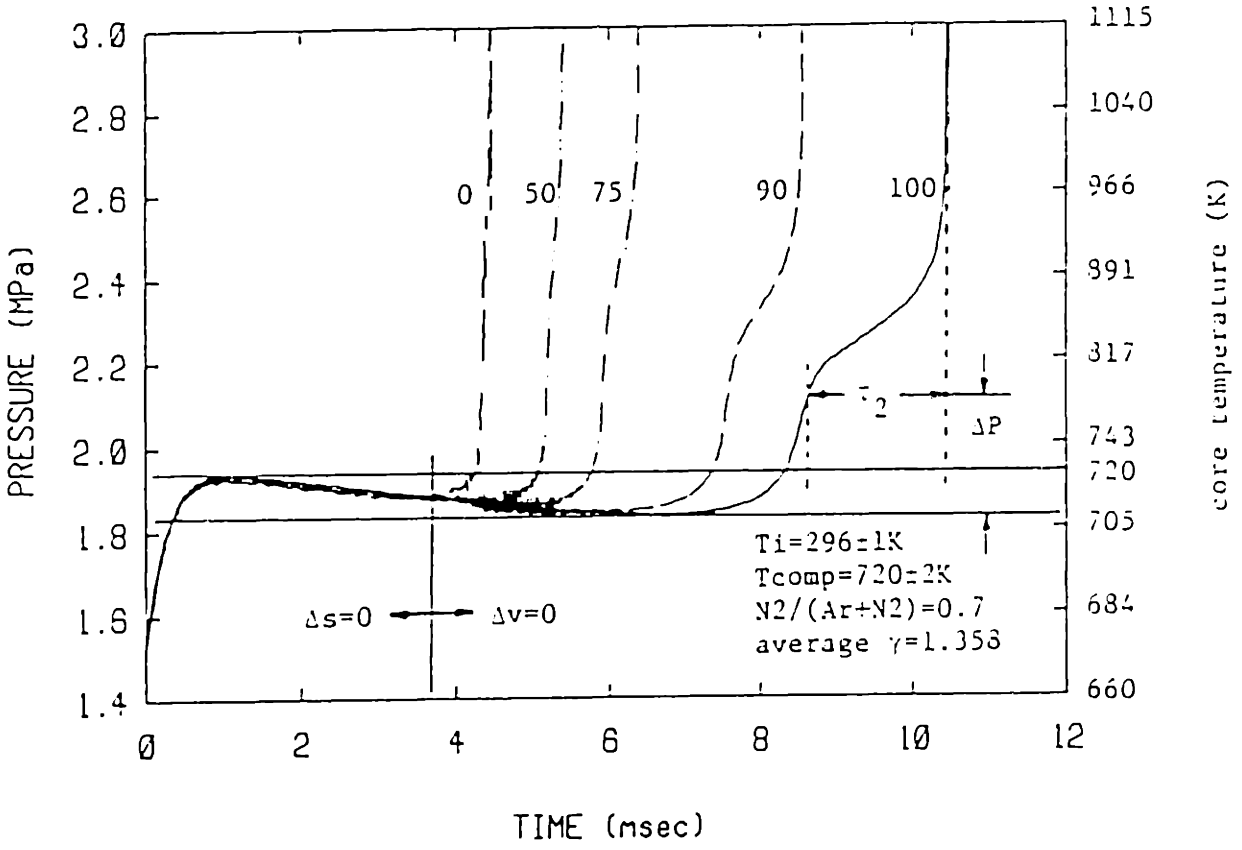

Figure 4.5 Pressure Records of Five Primary Reference Fuel Mixtures at P_i=500 torr : Equivalence Ratio=1, Diluents=N_2+Argon, Diluents/O_2 Ratio=3.77, N_2/Diluents=0.7, CR=15.8, Time 0 Shifted to Steepest Slope

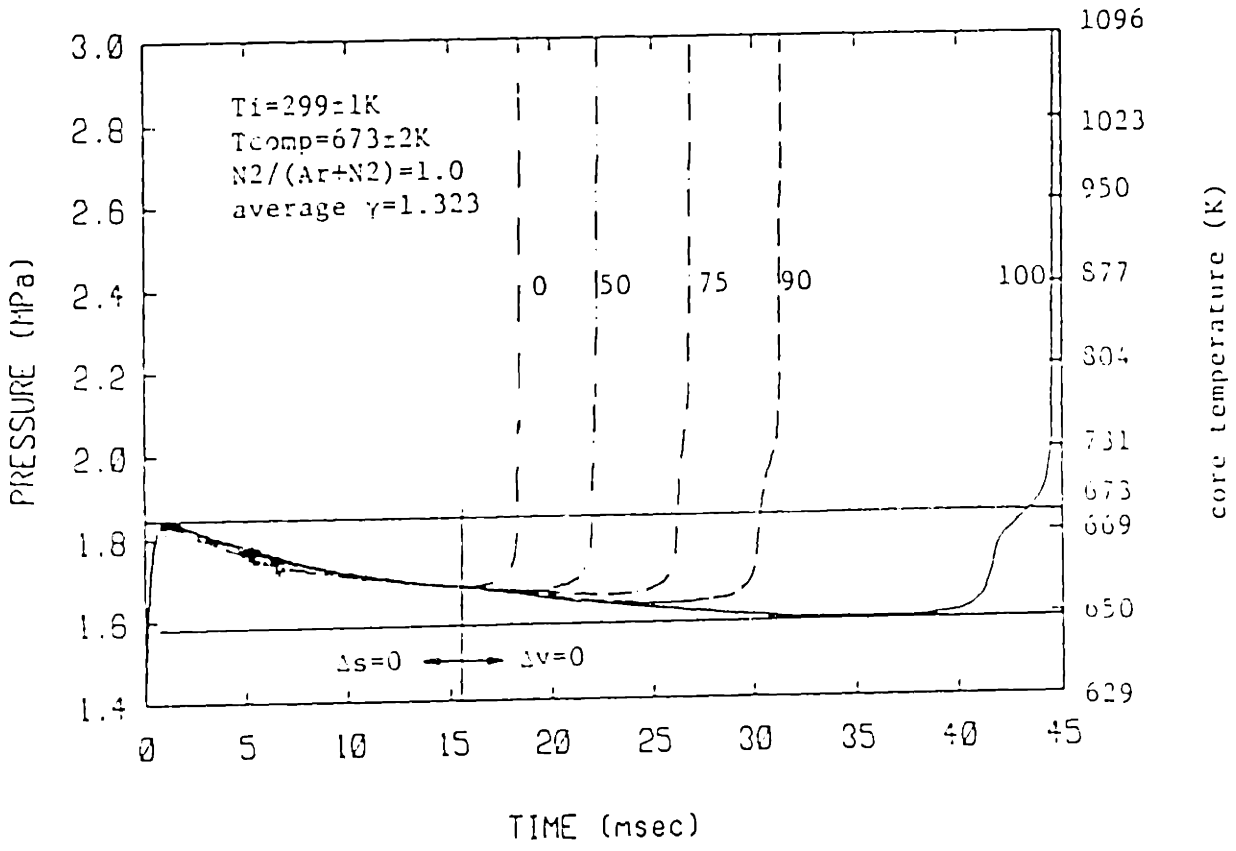

Figure 4.6 Pressure Records of Five Primary Reference Fuel Mixtures at P_i=500 torr : Equivalence Ratio=1, Diluents=N_2+Argon, Diluents/O_2 Ratio=3.77, N_2/Diluents=1.0, CR=15.8, Time 0 Shifted to Steepest Slope

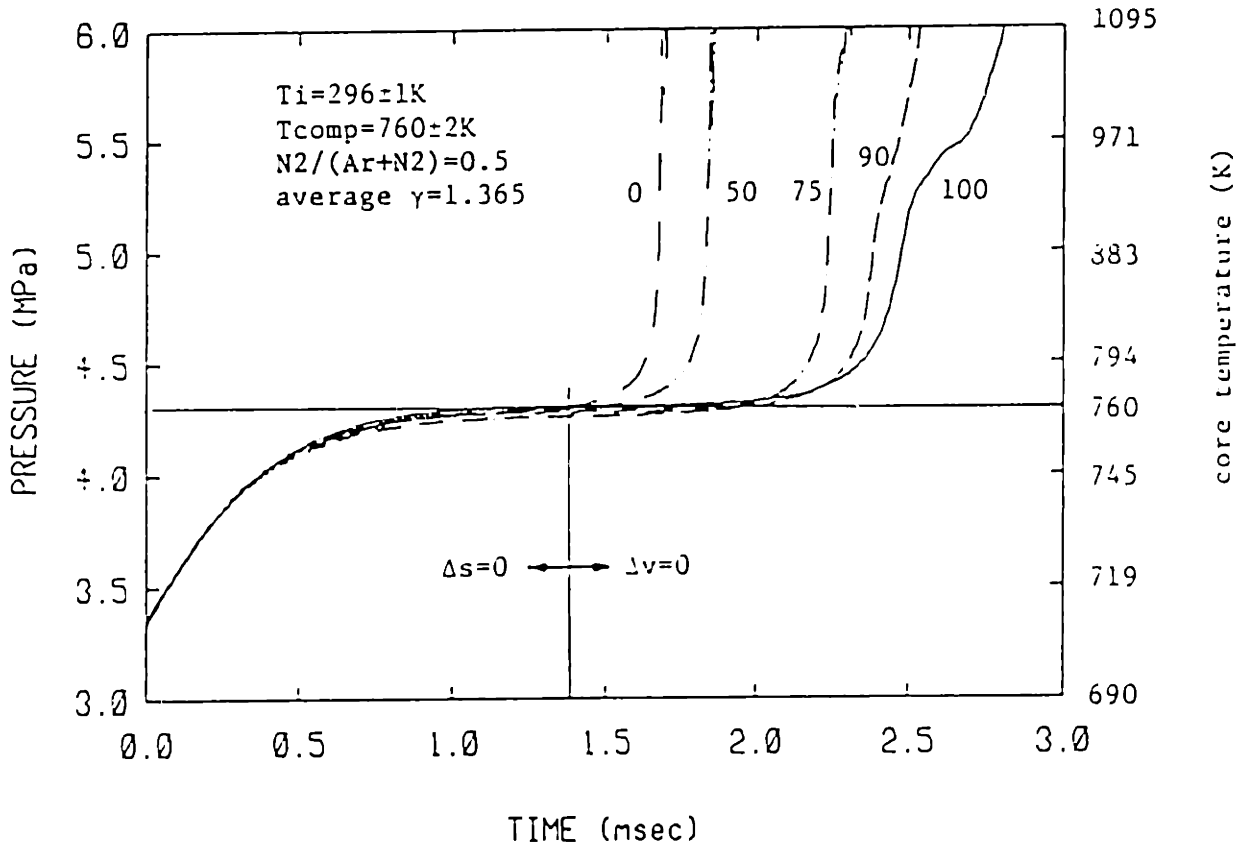

Figure 4.7 Pressure Records of Five Primary Reference Fuel Mixtures at P_i=1000 torr : Equivalence Ratio=1, Diluents=N_2+Argon, Diluents/O_2 Ratio=3.77, N_2/Diluents=0.5, CR=15.8, Time 0 Shifted to Steepest Slope

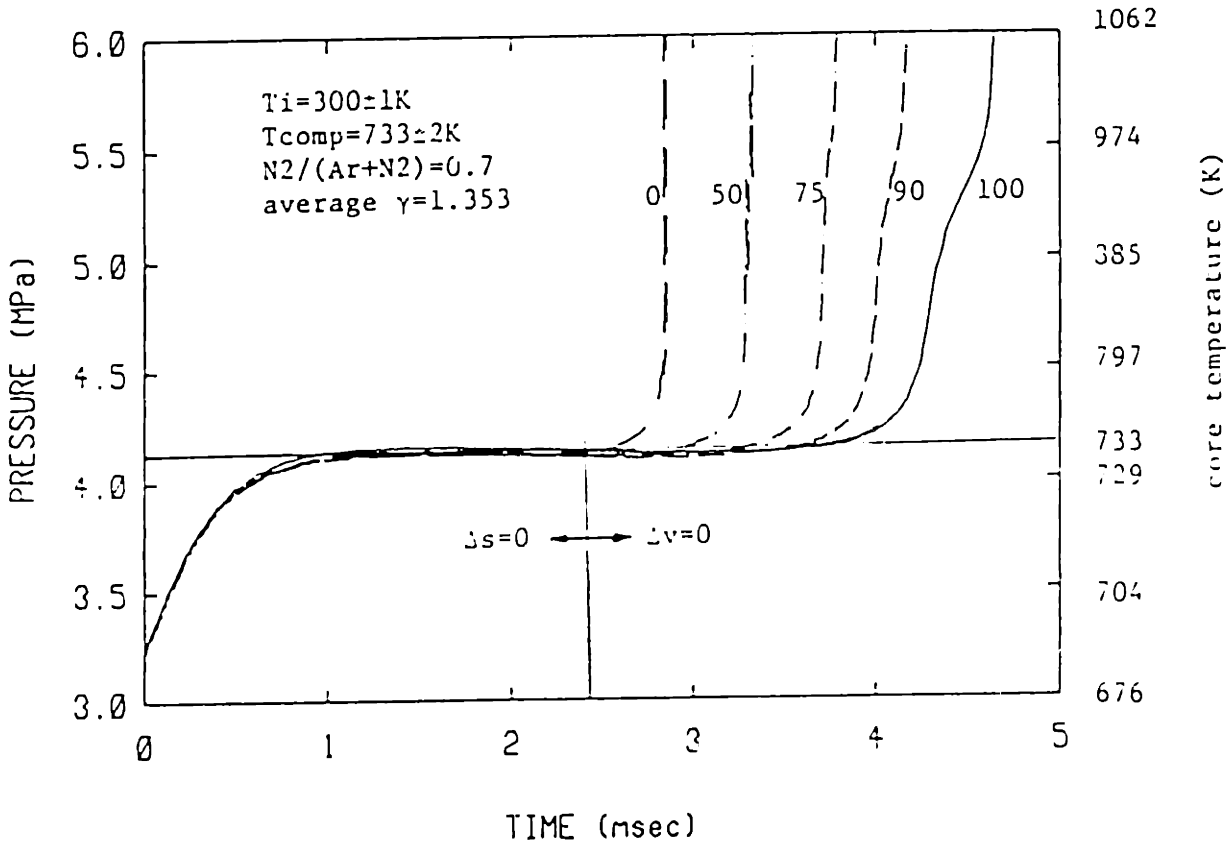

Figure 4.8 Pressure Records of Five Primary Reference Fuel Mixtures at P_i=1000 torr : Equivalence Ratio=1, Diluents=N_2+Argon, Diluents/O_2 Ratio=3.77, N_2/Diluents=0.7, CR=15.8, Time 0 Shifted to Steepest Slope

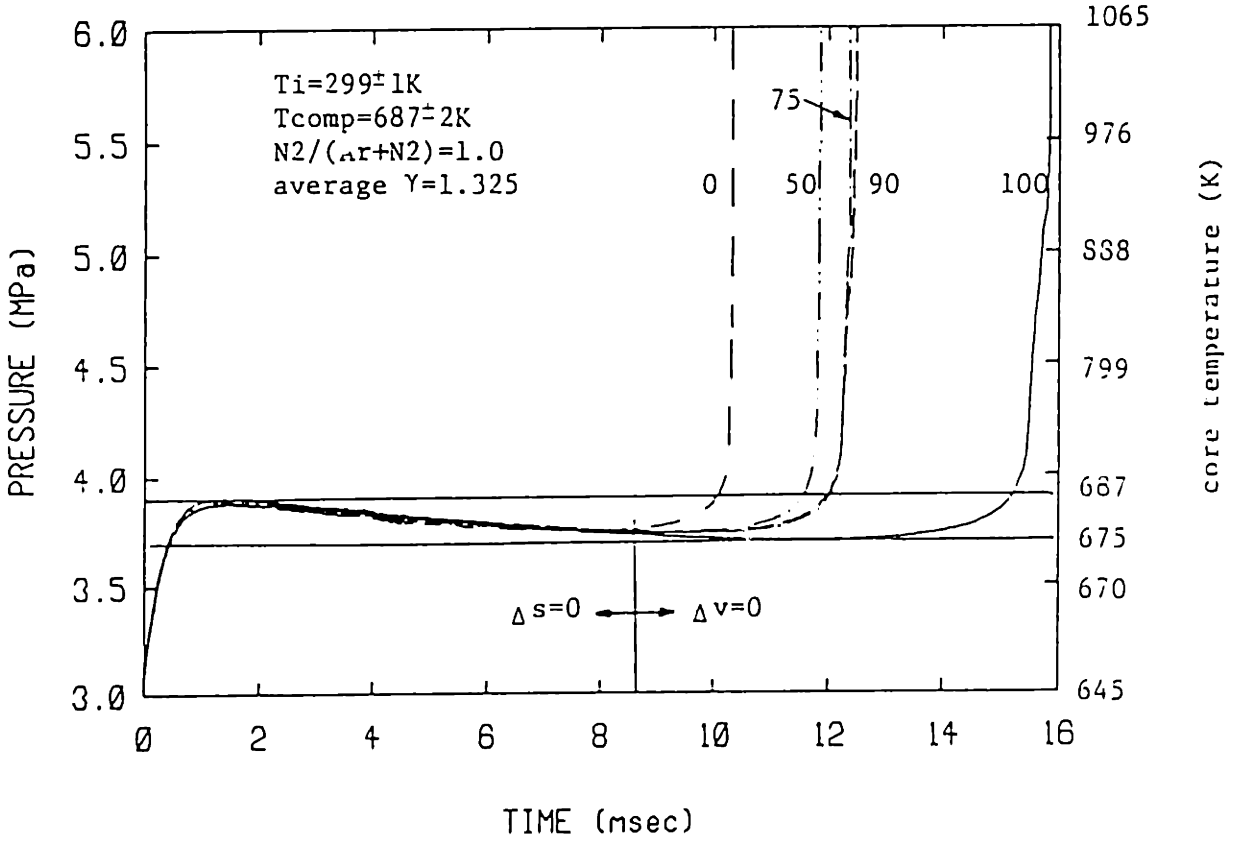

Figure 4.9 Pressure Records of Five Primary Reference Fuel Mixtures at P_i=1000 torr : Equivalence Ratio=1, Diluents=N_2+Argon, Diluents/O_2 Ratio=3.77, N_2/Diluents=1.0, CR=15.8, Time 0 Shifted to Steepest Slope

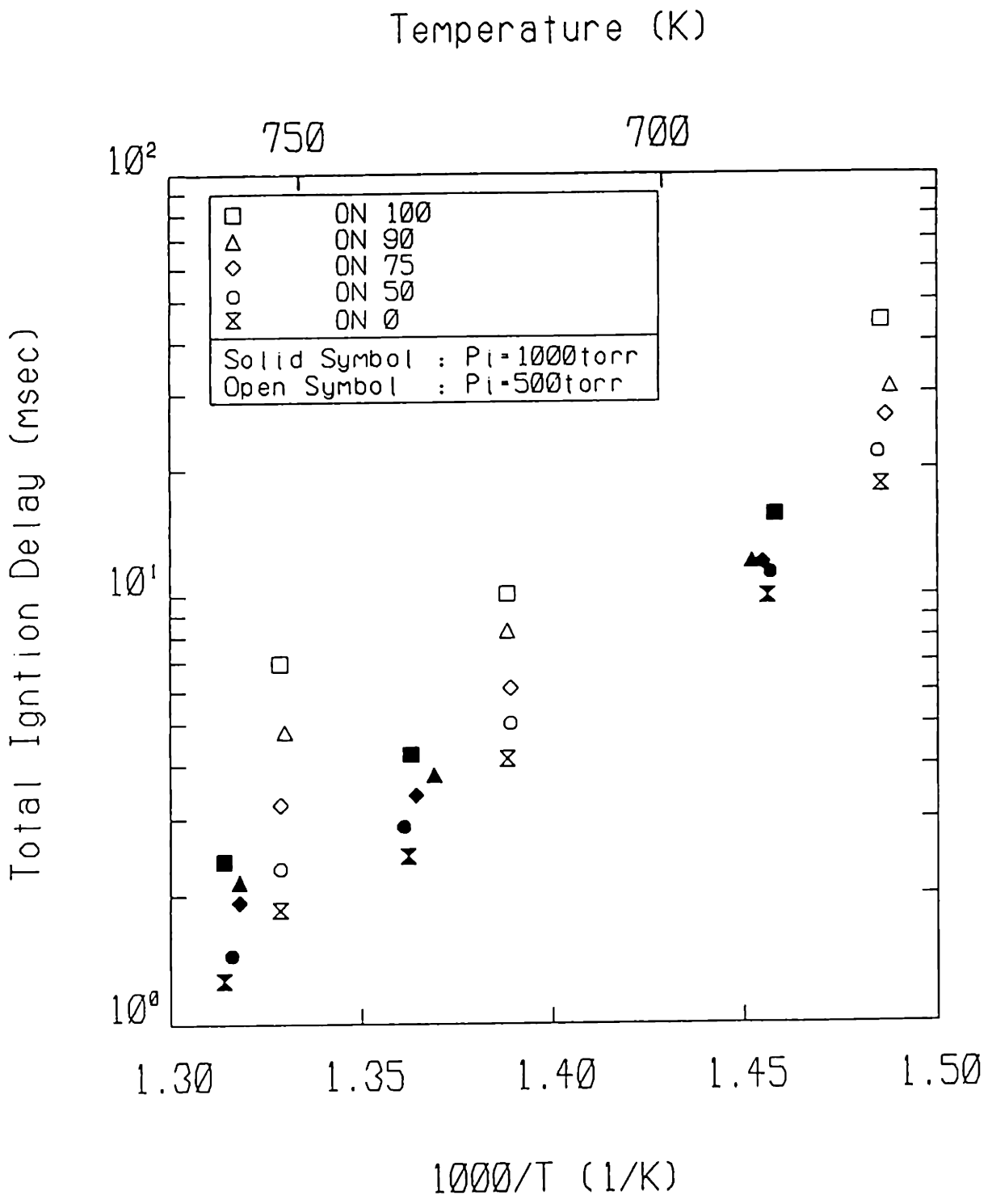

Figure 4.10 Measured Total Ignition Delay Times : Equivalence Ratio=1, Diluents=N_2+Argon, Diluents/O_2 Ratio=3.77

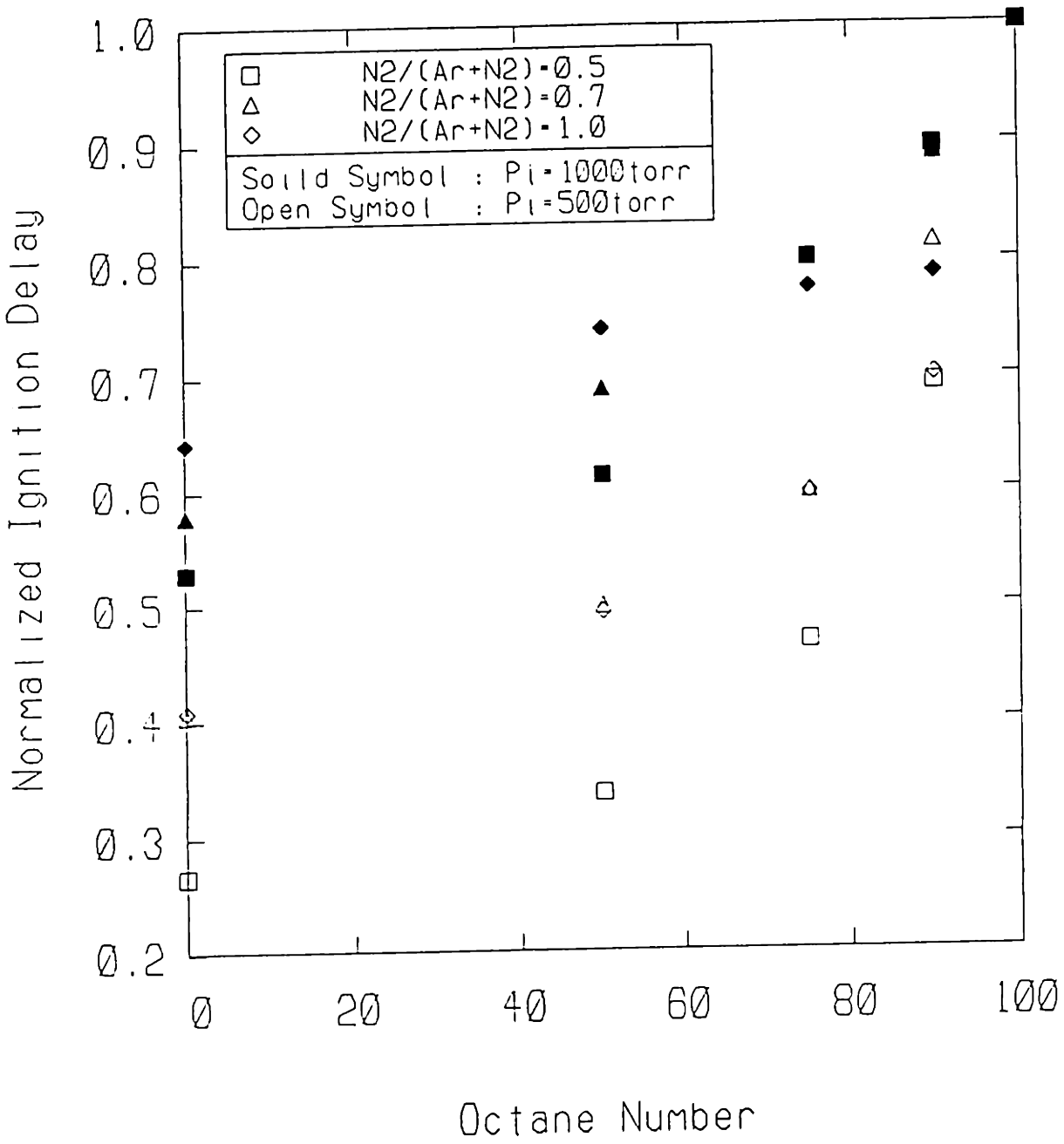

Figure 4.11 Normalized Total Ignition Delays : Equivalence Ratio=1, Diluents=N_2+Argon, Diluents/O_2 Ratio=3.77

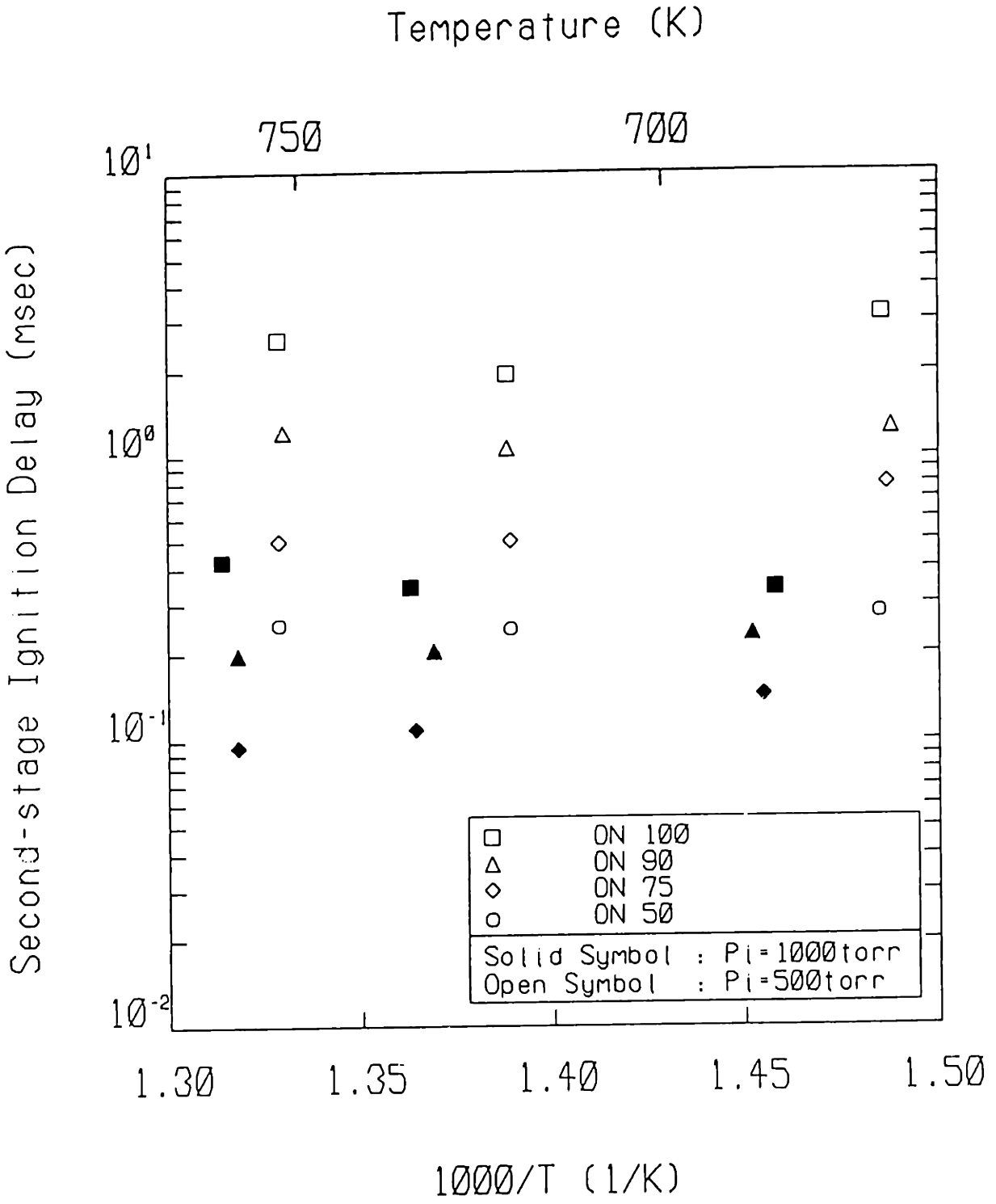

Figure 4.12 Second-stage Ignition Delay Times : Equivalence Ratio=1, Diluents=N_2+Argon, Diluents/O_2 Ratio=3.77

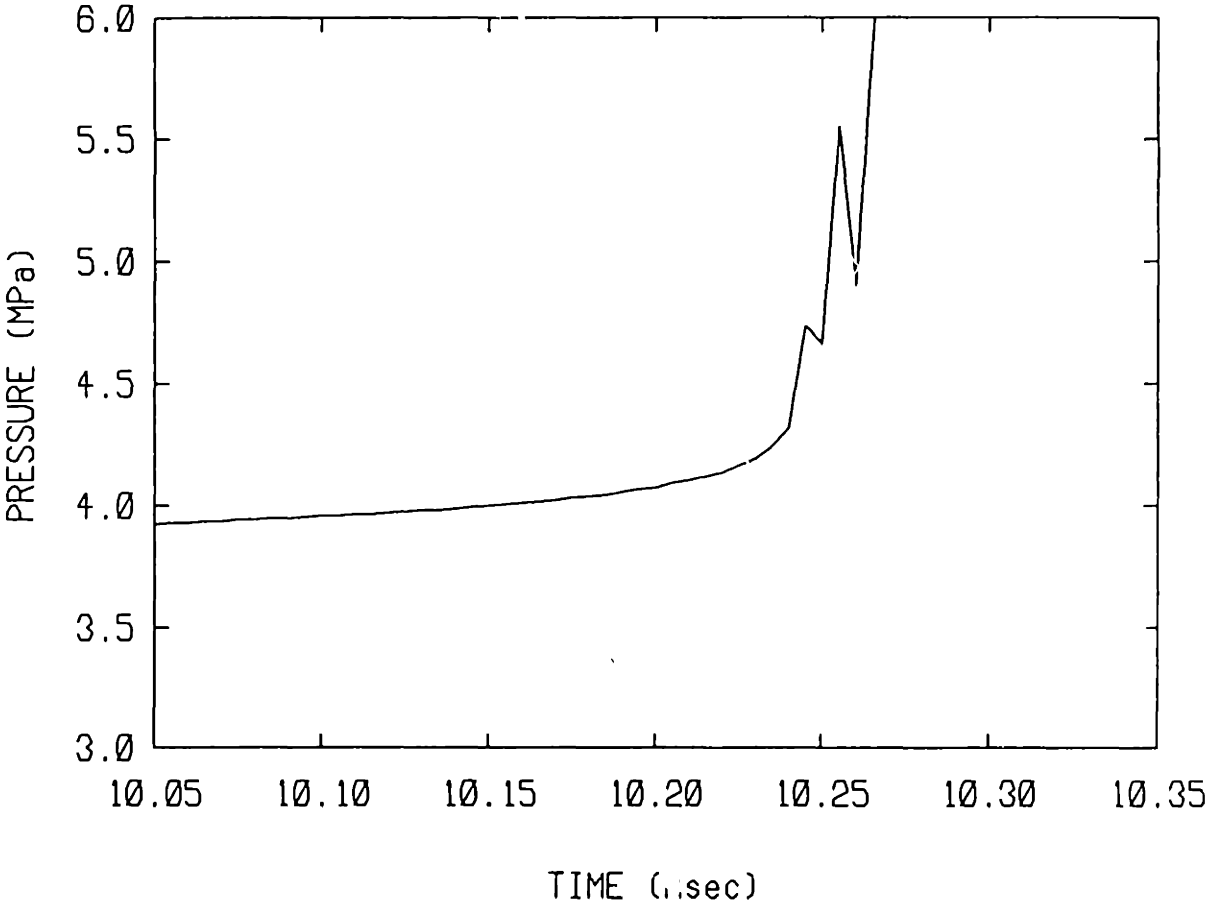

Figure 4.13 Pressure Record with Pressure Wave near Explosion : ON=0, P_i=1000Torr, Equivalence Ratio=1, Diluents=N_2+Argon, Diluents/O_2 Ratio=3.77, N_2/Diluents=1.0, CR=15.8, Time 0 Shifted to Steepest Slope

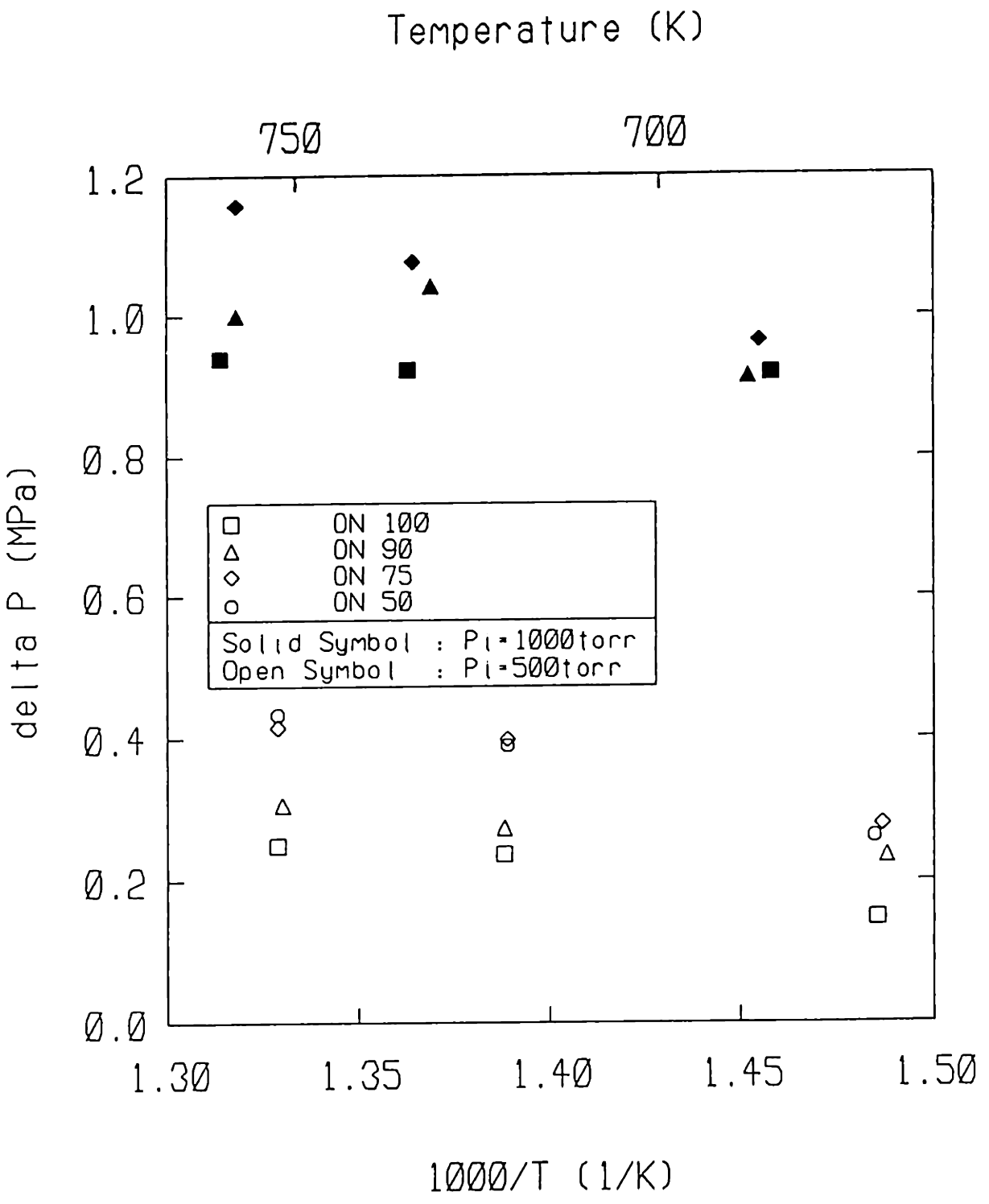

Figure 4.14 Pressure Rise During First-stage Ignition : Equivalence Ratio=1, Diluents=N_2+Argon, Diluents/O_2 Ratio=3.77

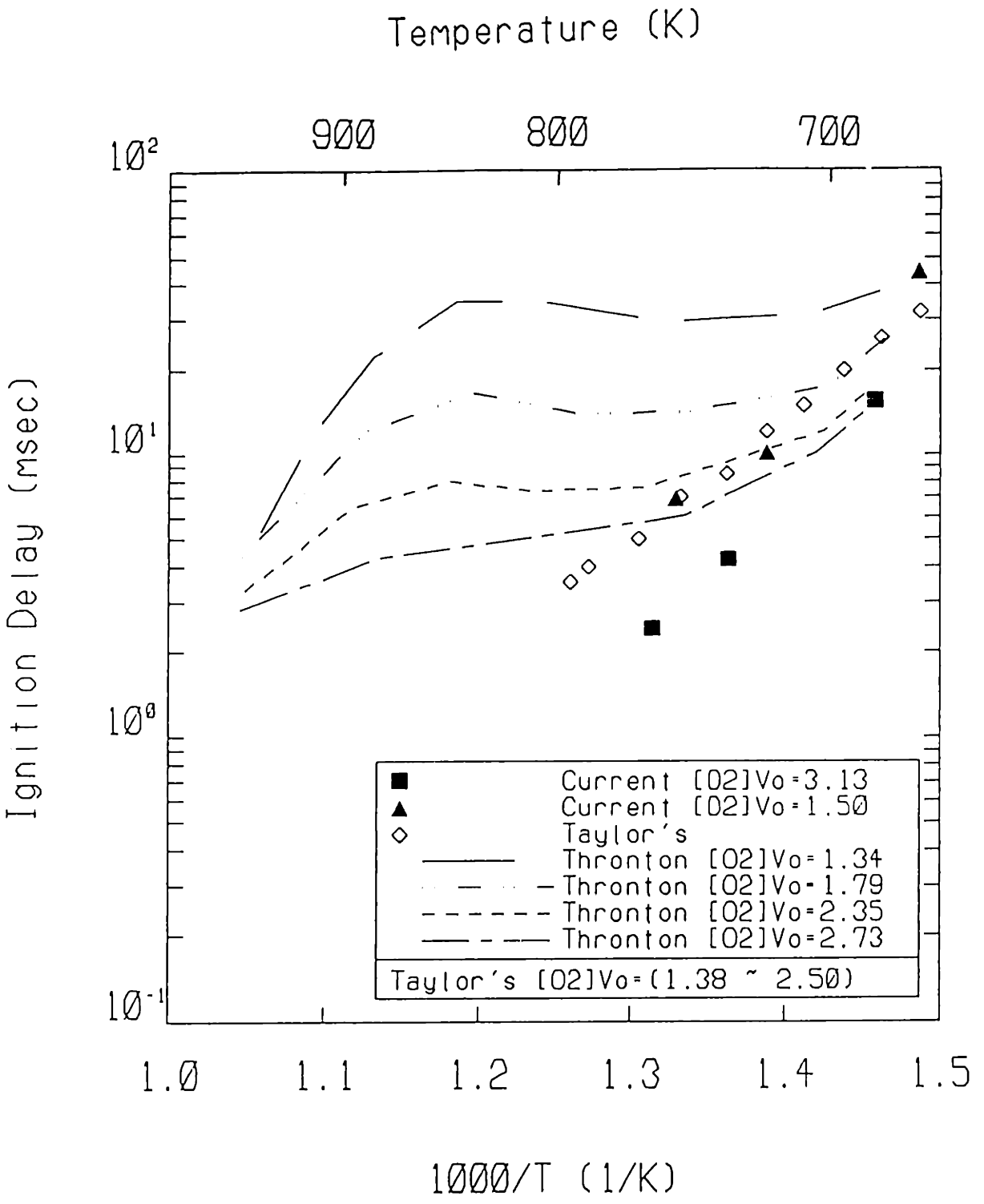

Figure 4.15 Comparison of Iso-octane Data with Existing Data : V_o=Standard Molar Volume (22400 cc/mole), $[O_2]$=Post-compression Core Oxygen Concentration

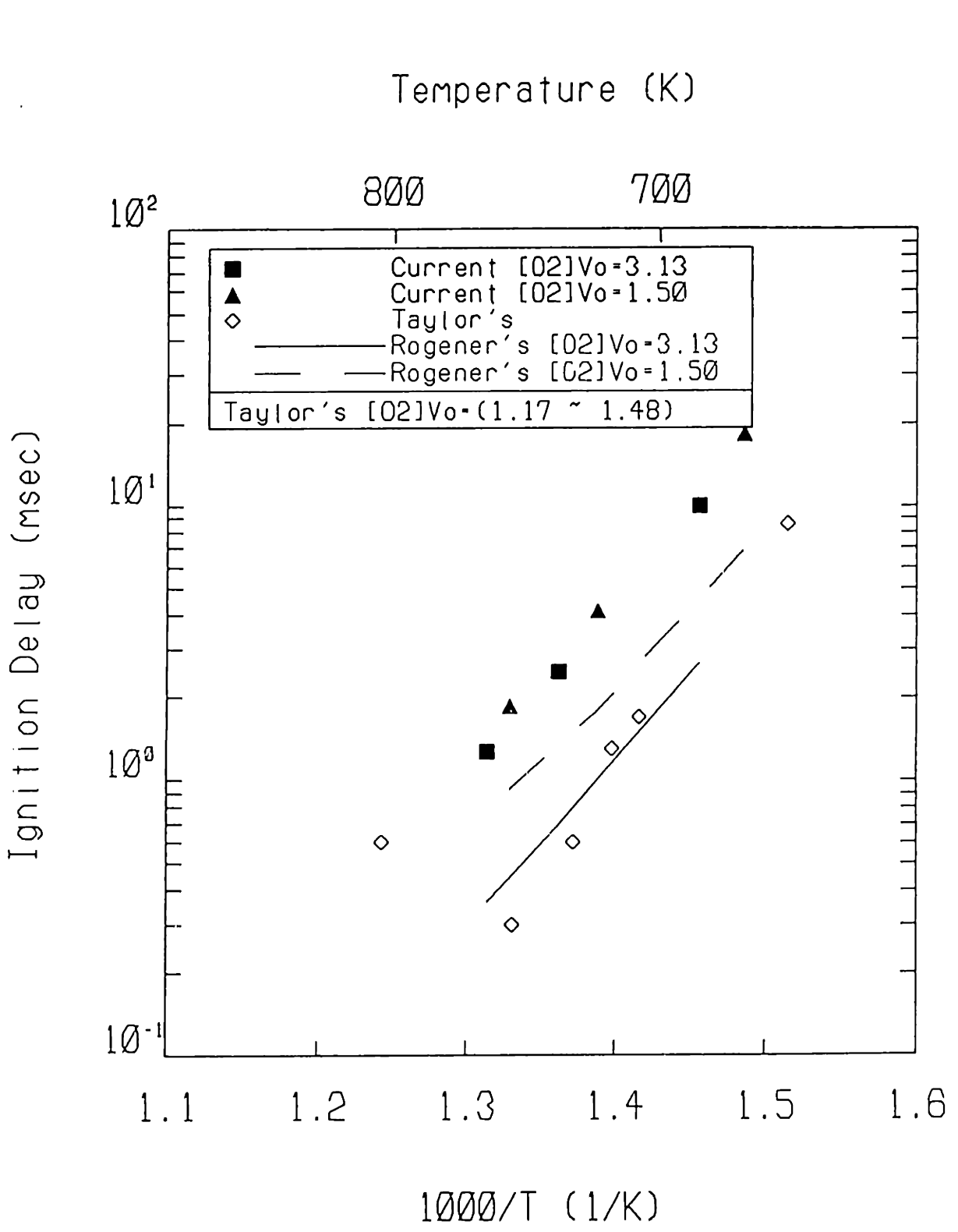

Figure 4.16 Comparison of Normal-heptane Data with Existing Data : V_o=Standard Molar Volume (22400 cc/mole), $[O_2]$=Post-compression Core Oxygen Concentration

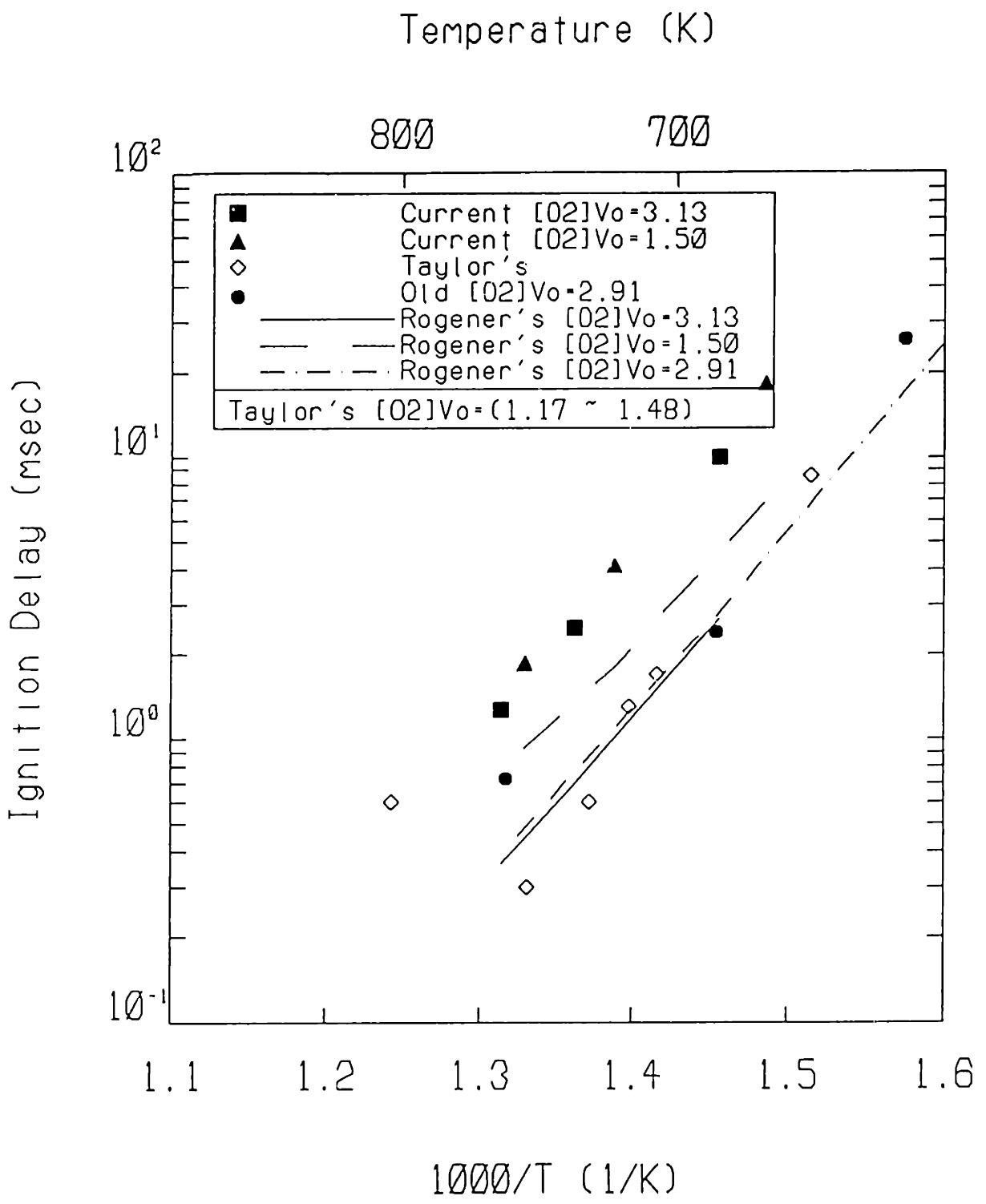

Figure 4.17 Comparison of Normal-heptane Data with Existing Data : Old Data=Data Taken from the Present RCM without O_2 Preceding Run, V_o=Standard Molar Volume (22400 cc/mole), $[O_2]$=Post-compression Core Oxygen Concentration

APPENDIX

A.1 Corner Vortex

Corner vortex is the rolled-up side wall boundary layer by a moving piston [9] as shown Fig. A.1, hence is a vigorous rotational flow which enhances mixing with the surrounding fluid. From the elementary entrainment theory [23], the differential equation governing the mass entrainment to the corner vortex is given by:

$$\frac{dm}{dt} = \rho_v \kappa \sqrt{\rho_v/\rho_c}\, A_v u_v \qquad (A1.1)$$

where m is the mass of the gas in the corner vortex, ρ_v is the density of the gas in the corner vortex, ρ_c is the density of the entraining core gas, A_v is the corner vortex entrainment area, u_v is the vortex average speed, and $\kappa = 0.1$ is a constant taken from the experiment with water [9].

When the temperature of the gas in the vortex is assumed to be the same as the wall temperature, the corner vortex density ρ_v and the corner vortex mass m are obtained from the ideal gas relation:

$$\rho_v = P/RT_w \qquad (A1.2)$$

$$m = PV/RT_w = \frac{\pi b P A}{RT_w} \qquad (A1.3)$$

where T_w is the wall temperature, b is the test chamber bore, and A is the cross-sectional area of corner vortex. When the vortex average speed u_v is assumed to be the same as the piston speed, and the core gas is assumed to follow the ideal isentropic relations, the following relations are obtained:

$$u_v = u_p \qquad (A1.4)$$

$$dt = dx/u_p \qquad (A1.5)$$

$$\rho_c = \frac{P}{RT} = \frac{P}{RT_w (P/P_i)^{(\gamma-1)/\gamma}}$$

$$= \frac{P^{1/\gamma}}{RT_w} P_i^{(\gamma-1)/\gamma} \qquad (A1.6)$$

$$A_v = \pi b\sqrt{\pi A} \qquad (A1.7)$$

where u_p is the piston speed, x is the piston displacement, γ is the specific heat ratio, and P_i is the initial pressure. Substitution of (A1.2) through (A1.7) into (A1.1) gives:

$$\frac{d(PA)}{dx} = \kappa\sqrt{\pi A}\, P_i^{(\gamma-1)/2\gamma} p^{(\gamma+1)/2\gamma} \qquad (A1.8)$$

Since it was assumed that the core gas follows ideal isentropic relation, the relation for the pressure can be approximated as:

$$P = P_i \left(\frac{S+h}{S+h-x}\right)^{\gamma} \qquad (A1.9)$$

where h is the clearance height, and S is the stroke. The final differential equation is obtained by combining (A1.8) and (A1.9) as:

$$\frac{dA}{dt} = \kappa\sqrt{\pi A}\left(\frac{S+h}{S+h-x}\right)^{-(\gamma-1)/2} - \frac{Ab}{2}\left(\frac{1}{S+h-x}\right) \qquad (A1.10)$$

The solution to the above differential equation with the initial condition A = 0 at x = 0 is given by:

$$A = 4\kappa^2\pi(S+h)^{-\gamma+1}(S+h-x)^{\gamma}\left[\sqrt{(S+h)} - \sqrt{(S+h-x)}\right]^2 \qquad (A1.11)$$

At the end of the compression when x = S = (CR-1)h, the corner vortex area is given by:

$$A = 4\kappa^2\pi CR^{-\gamma+1}(CR^{1/2}-1)^2\, h^2 \qquad (A1.12)$$

The vortex diameter d_v is obtained from (A1.12) as follows:

$$d_v = \sqrt{4A/\pi} = 4\kappa CR^{(-\gamma+1)/2}(CR^{1/2}-1)h \qquad (A1.13)$$

A.2 Characteristic Times

(1) Characteristic heating time (τ_{ch})

Characteristic heating time is defined as the reciprocal of the logarithmic temperature rise rate at the end of the compression, and is given by the following relation:

$$\frac{1}{\tau_{ch}} = \frac{d(\ln T)}{dt} = -\frac{\gamma-1}{V}\frac{dV}{dt} = (\gamma-1)\frac{u_p}{h}$$

$$\tau_{ch} = h/(\gamma-1)u_p \qquad (A2.1)$$

where T and V are the temperature and volume of the test gas, respectively, and u_p is the piston speed.

(2) Laminar cooling time (τ_{lc})

Laminar cooling time is defined as the time when the thermal boundary layer merges halfway, and is given by the following relation:

$$\frac{h}{2} = \sqrt{\alpha \tau_{lc}}$$

$$\tau_{lc} = \frac{h^2}{4\alpha} \qquad (A2.2)$$

where α is the thermal diffusivity of the test gas.

(3) Characteristic pre-reaction time (τ_{pr})

Characteristic pre-reaction time is defined as the ratio of the reaction that has completed during the compression to the reaction rate at the end of the compression when the reaction rate is represented by an Arrhenius form, i.e., $R = A \exp(-\beta\theta)$ where A is the pre-exponential factor, β is the reciprocal of absolute temperature, and θ is the activation energy.

It is assumed that the test gas is compressed isentropically; and that the piston maintains a constant speed during the compression and stops at a constant deceleration. From the first assumption, the reciprocal of absolute temperature β is given by:

$$\frac{\beta}{\beta_f} = \left(\frac{\zeta}{h}\right)^{\gamma-1} = 1 + (\gamma-1)\left(\frac{\zeta}{h} - 1\right) + \ldots \qquad (A2.3)$$

where ζ is the piston displacement. From the second assumption, the piston displacement is given by:

$$\zeta = h + \frac{1}{2}at^2 \qquad \text{for } -\frac{u_p}{a} < t < 0$$

$$= h + u_p\left(-t - \frac{u_p}{2a}\right) \qquad \text{for } t < -\frac{u_p}{a} \qquad (A2.4)$$

where a is the piston deceleration during the piston stopping, and time t is measured backward from the end of compression.

Substitution of the first order term of (A2.3) and (A2.4) to the reaction rate R and the integration of the reaction rate R with respect to $\tau = -t$ from 0 to ∞ give:

$$I/R_f = \int_0^{u_p/a} \exp\left[-(\gamma-1)\beta_f\theta\frac{a\tau^2}{2h}\right] d\tau$$

$$+ \int_{u_p/a}^{\infty} \exp\left[-(\gamma-1)\beta_f\theta\frac{u_p}{h}\left(\tau - \frac{u_p}{2a}\right)\right] d\tau$$

where R_f is the reaction rate at the end of compression. Under the assumption of $(\gamma-1)\beta_f\theta at^2/2/h < 1$, the above integration is carried out to give the characteristic heating time as follows:

$$\tau_{pr} = I/R_f = \left(\frac{u_p}{a} + \frac{h}{(\gamma-1)\beta_f\theta u_p}\right) - \ldots$$

$$\sim \left(\frac{u_p}{a} + \frac{h}{(\gamma-1)\beta_f\theta u_p}\right) \qquad (A2.5)$$

(4) Characteristic compression time (τ_c)

Characteristic compression time is defined as the time needed for the piston to compress the test gas, and is given by the following relation:

$$\tau_c = \frac{S}{u_p} = \frac{(CR-1)h}{u_p} \qquad (A2.6)$$

(5) Measured and calculated cooling time (τ_{mc} and τ_{cc})

Cooling times are defined as the reciprocal of the logarithmic pressure drop rate after the compression. Measured one is determined from the measured pressure trace as:

$$\tau_{mc} = P/(dP/dt)|_{t=\tau_c}$$
$$\sim P_p/[(P_p - P(\tau_c+\Delta t))/\Delta t] \qquad (A2.7)$$

where P_p is the post-compression pressure. Calculated one is determined from the laminar cooling time as:

$$\tau_{cc} = h\Delta t \;/\; 2\sqrt{\alpha(\tau_c+\Delta t)} \qquad (A2.8)$$

where Δt is taken as 50 msec.

(6) Mechanical stopping time (τ_{ms})

Mechanical stopping time is defined as the time needed for the piston to stop, and is given by:

$$\tau_{ms} = \frac{u_p}{a} \qquad (A2.9)$$

where a is the piston deceleration during the piston stopping.

(7) Temperature stopping time (τ_{ts})

Temperature stopping time is defined as a duration from the time where the temperature is peak at the end of compression to the time where the core temperature of the gas begins to roll off at the end of the compression due to the piston deceleration, and is given by:

$$\tau_{ts} = \sqrt{\frac{2h}{(2\gamma+1)a}} \qquad \text{for } u_p > \sqrt{\frac{2}{1+2\gamma}}\, ah$$

$$= \frac{u_p}{a} \qquad \text{for } u_p < \sqrt{\frac{2}{1+2\gamma}}\, ah \qquad \text{(A2.10)}$$

A.3 RCM Dynamics

The governing equations for the coupled dynamics of the piston and the fast-acting-valve were derived using an one-dimensional incompressible fluid model. To accommodate viscous behavior of hydraulic fluid, lumped parameters such as velocity coefficients (C_v), contraction coefficients (C_c), and loss coefficients (k) were used. In Fig. A.2, the variables used in the derivation and the important numbers used in the calculation were summarized. The derivation was divided into four regions.

(1) $0 < y \leqslant \delta$

The piston motion is governed by the Newton's second law of motion:

$$M_p D^2 x = A_d P_d - A_p P_1 - A_t P_t \qquad (A3.1)$$

where D(·) is d(·)/dt, P_d is the driving pressure, and P_t is the test chamber pressure, which is assumed to follow ideal isentropic relation as follows:

$$P_t = P_{to} \left(\frac{\pi r_0^2 (S+h) + V_{cr}}{\pi r_0^2 (S+h-x) + V_{cr}} \right)^{\gamma} \qquad (A3.2)$$

where S is the stroke, h is the clearance height, V_{cr} is the corner vortex containment volume, and P_{to} is the initial test chamber pressure. The fast-acting-valve motion is also governed by the Newton's second law of motion:

$$M_v D^2 y = A_v P_2' - A_v P_a - \pi (r_4^2 - r_3^2)(P_5 + \rho D y^2/2) + \pi (r_4^2 - r_3^2) P_3 \qquad (A3.3)$$

where $\rho = 840$ Kg/m^3 is the density of hydraulic oil. The piston displacement x and the valve displacement y are related from the continuity consideration as follows:

$$A_p x = A_v y \qquad (A3.4)$$

An application of the Bernoulli equation from the location (1) to (2) in Fig. A.2 gives the following relation:

$$P_1 + \frac{\rho}{2}Dx^2 = \rho D^2x(S-x) + \rho\frac{2A_p}{3\pi d}\ln(r_2/r_1)D^2x + P_2 + \frac{\rho}{2}\left(\frac{2A_p}{3\pi r_2 d}\right)^2 Dx^2 + k_1\frac{\rho}{2}D^2x \qquad (A3.5)$$

where k_1 is the loss coefficient between the locations (1) and (2). The relation between P_2 and P_2' is obtained as follows:

$$P_2 = P_2' + k_2\frac{\rho Dx^2}{2(y+\epsilon)^2} \qquad (A3.6)$$

where k_2 is the loss coefficient at the inlet of the valve area A_v, and $\epsilon = 0.005"$ is the O-ring gap between the fast-acting-valve and the base as shown in Fig. A.2.

Combining the relations (A3.1) to (A3.6) with the assumption of $P_3 = P_5 = P_a$ gives the final governing equations for the region $y \leqslant \delta$ as follows:

$$x = A_v/A_p\, y \qquad (A3.7)$$

$$D^2y = \left[\frac{\rho Dy^2}{2}\{A_v^3/A_p^2\{1-(2A_p/3\pi r_2 d)^2 - k_1 - k_2/(y+\epsilon)^2\} - \pi(r_4^2 - r_3^2)\} + A_v/A_p(A_dP_d - A_pP_a - A_tP_t)\right] \qquad (A3.8)$$

$$/\left[M_v + A_v^2/A_p^2\{M_p + \rho A_p(S + \frac{2A_p}{3\pi d}\ln(\frac{r_2}{r_1})\} - \rho A_v^3/A_p^2 y\right]$$

(2) $\delta < y \leqslant d$

The piston motion and the fast-acting-valve motion are again governed by (A3.1) and (A3.3), respectively. The relation (A3.5) and (A3.6) can be also used again to relate oil pressures P_1, P_2, and P_2'. Since the fast-acting valve opens an area of $2\pi r_3(y-\delta)$ and the pressure is relieved through this area when $y > \delta$, the continuity relation become:

$$A_pDx = A_vDy + C_{c3}2\pi r_3(y-\delta)v_3$$

$$= A_v Dy + C_{c4} A_o v_4 \qquad (A3.9)$$

where C_{c3} and C_{c4} are the contraction coefficients, and v_3 and v_4 are the speeds of hydraulic oil at the location (3) and (4) respectively in Fig. A.2. From the Bernoulli equation, the P_3 and P_2' are given by:

$$P_3 = P_a + \frac{\rho}{2} v_4^2 + \left(\frac{1}{C_{v4}^2} - 1\right)\frac{\rho}{2} v_4^2$$

$$= P_a + \frac{\rho (A_p Dx - A_v Dy)^2}{2 A_o^2 C_{d4}^2} \qquad (A3.10)$$

$$P_2' = P_3 + (1+k_3)\frac{\rho}{2} v_3^2 + \left(\frac{1}{C_{v3}^2} - 1\right)\frac{\rho}{2} v_3^2 \qquad (A3.11)$$

$$= P_a + \frac{\rho}{2}(A_p Dx^2 - A_v Dy^2)\left[\frac{1 + k_3}{C_{d3}^2 (2\pi r_3 (y-\delta))^2} + \frac{1}{C_{d4}^2 A_o^2}\right]$$

where $C_{d3} = C_{v3}\, C_{c3}$ and $C_{d4} = C_{v4}\, C_{c4}$ are the discharge coefficients, and k_3 is the loss coefficient at the location (3). Combining (A3.1), (A3.3), (A3.5), (A3.6), (A3.9), (A3.10), and (A3.11) gives:

$$D^2 x = \Big[(A_d P_d - A_p P_a - A_t P_t) - \frac{\rho A_p}{2}\Big\{\Big(\frac{2A_p}{3\pi r_{2d}}\Big)^2 + k_1 - 1\Big\} Dx^2$$

$$+ k_2 Dx^2/(y+\epsilon)^2$$

$$+ (A_p Dx - A_v Dy)^2 \Big\{\frac{1+k_3}{C_{d3}^2 (2\pi r_3 (y-\delta))^2} + \frac{1}{C_{d4}^2 A_o^2}\Big\}\Big\}\Big]$$

$$/\Big[M_p + \rho A_p \Big\{S + \frac{2A_p}{3\pi d} \ln(r_2/r_1)\Big\} - \rho A_p x\Big] \qquad (A3.12)$$

$$D^2 y = \frac{\rho}{2M_v}\Big[A_v (A_p Dx - A_v Dy)^2 \Big\{\frac{1+k_3}{C_{d3}^2 (2\pi r_3 (y-\delta))^2} + \frac{1}{C_{d4}^2 A_o^2}\Big\}$$

$$- \pi (r_4^2 - r_3^2) Dy^2\Big] \qquad (A3.13)$$

where P_5 is assumed to be the same as P_3.

(3) $x \leqslant$ S-lsp and $d < y \leqslant d+lsv$

The piston motion is still governed by (A3.12), and the fast-acting-valve motion is governed by the following relation:

$$M_v D^2 y = A_v P_2' - A_v P_a - \pi(r_4^2 - r_3^2)(P_5 + \rho D y^2/2) + \pi(r_4^2 - r_3^2)P_3 - F_{sv} \qquad (A3.14)$$

where F_{sv} is the valve stopping force exerted by the pin and groove stopping mechanism of the valve. The details of the fast-acting-valve stopping pin and groove are shown in Fig. A.3. When the flow field is transformed using Gallilean transformation, i.e., the fast-acting-valve (or the pin) is stationary and the groove moves at the speed of Dz on the negative y direction, the oil speed $v(z)$ through the gap between the pin and the groove is obtained from the continuity consideration as:

$$v(z) = A_{sv} / A_s(z)\, Dz \qquad (A3.15)$$

where $z = y-d$, and A_{sv} and $A_s(z)$ are shown in Fig. A.3. An application of the Bernoulli equation through the gap between the pin and the groove gives the following relation:

$$P_5 + \frac{\rho}{2}v(z)^2 + \rho\int_0^z Dv(\zeta)\, d\zeta = P_s$$

$$P_s - P_5 = \frac{\rho}{2}\left(\frac{A_{sv}}{A_s(z)}\right)^2 Dz^2 + \frac{\rho A_{sv}}{\pi}D^2 z \int_0^z \frac{1}{r_4^2 - r(\zeta)^2}\, d\zeta$$

$$F_{sv} = A_{sv}(P_s - P_5) \qquad (A3.16)$$

$$= A_{sv}\frac{\rho}{2}Dz^2\left(\frac{A_{sv}}{A_s(z)}\right)^2 + \frac{\rho A_{sv}^2 D^2 z}{\pi}\int_0^z \frac{1}{r_4^2 - r(\zeta)^2}\, d\zeta$$

The relations (A3.14) and (A3.16) were used to calculated the optimal valve stopping pin shape, which gives a constant deceleration of the fast-acting-valve. As before, P_5 is assumed to be the same as P_3 in the calculation.

(4) S-lsp < x ≤ S

Since the valve has already come to rest, the piston motion is governed by setting y = d+lsv and Dy = 0 in (A3.12) and by adding the piston stopping force F_{sp} exerted by the pin and groove to (A3.12) as follows:

$$D^2x = [(A_dP_d - A_pP_a - A_tP_t) - \frac{\rho A_p}{2}\{\{(\frac{2A_p}{3\pi r_2 d})^2 + k_1 - 1\}Dx^2 + \frac{k_2 Dx^2}{(lsv+d+\epsilon)^2} - F_{sp} + A_p^2 Dx^2\{\frac{1+k_3}{C_{d3}^2(2r_3\pi(d+lsv-\delta))^2} + \frac{1}{C_{d4}^2 A_o^2}\}\}]$$
$$/[M_p + \rho A_p\{S+\frac{2A_p}{3\pi d}\ln(r_2/r_1)\} - \rho A_p x] \qquad (A3.17)$$

where F_{sp} is the piston stopping force exerted by the pin and groove stopping mechanism of the piston. The details of the piston stopping pin and groove are shown in Fig. A.4. Due to high deceleration, i.e., highly negative value of D^2x, the hydraulic oil cavitates. When the oil cavitates, P_1 is set to the vapor pressure of the oil and the governing equation (A3.17) is simplified as:

$$M_pDx^2 = A_dP_d - A_pP_v - A_tP_t - F_{sp} \qquad (A3.18)$$

where P_v is the vapor pressure of the hydraulic oil. From the continuity consideration, the oil speed v(z) through the gap between the pin and the groove is given by:

$$v(z) = A_{sp} / A_s(z)\, Dz \qquad (A3.19)$$

where $z = x-S+lsp$, and A_{sp} and $A_s(z)$ are shown in Fig. A.4. An application of the Bernoulli equation through the gap between the pin and the groove gives the following relation:

$$P_1 + \frac{\rho}{2}v(z)^2 + \rho\int_0^z Dv(\zeta)\, d\zeta = P_s$$

$$P_s - P_1 = \frac{\rho}{2}\left(\frac{A_{sp}}{A_s(z)}\right)^2 Dz^2 + \frac{\rho A_{sp}}{\pi}D^2 z \int_0^z \frac{1}{r(\zeta)^2 - r_0^2}\, d\zeta$$

$$F_{sp} = A_{sp}(P_s - P_1) \qquad \text{(A3.20)}$$

$$= A_{sp}\frac{\rho}{2}Dz^2\left(\frac{A_{sp}}{A_s(z)}\right)^2 + \frac{\rho A_{sp}^2 D^2 z}{\pi}\int_0^z \frac{1}{r(\zeta)^2 - r_0^2}\, d\zeta$$

The relations (A3.18), (A3.19), and (A3.20) were used to calculated the optimal piston stopping pin shape.

A.4 Laminar Heat Transfer Model for Inert Gas

Laminar heat transfer model for inert gas experiments with the piston head with the crevice was developed based on the following assumptions:

1. the test gas obeys the ideal gas relation of state;
2. flow is laminar;
3. the corner vortex is captured in the piston head crevice;
4. there exists a well-defined core temperature region;
5. the temperature of gas captured in the piston head crevice is given by;

$$T_{cr} = T_i * Y + T_{core} * (1-Y)$$

where T_{cr} is the gas temperature in the piston head crevice, T_i is the initial temperature, T_{core} is the core gas temperature, and Y is the temperature ratio which ranges from 1 to 0 (throughout this thesis, Y is assumed to be 1).

For a gas subject to time-dependent pressure, the displacement thickness, δ, and the heat flux through the wall, dq/dt, were investigated by J.C. Keck [22], and they are given by:

$$\begin{aligned}
\delta &= \int_0^\infty \left(\frac{\rho}{\rho_{core}} - 1 \right) dx \\
&= \left(\frac{\alpha_o}{\pi}\right)^{.5} \left(\frac{P_i}{P}\right)^{1/\gamma} \int_0^t \left[\int_\xi^t \frac{P}{P_i}\, d\zeta \right]^{-.5} \left[\frac{P}{P_i} - \left(\frac{P}{P_i}\right)^{1/\gamma} \right] d\xi \\
&= \frac{2(\gamma-1)}{\gamma} \left(\frac{\alpha_o}{\pi}\right)^{.5} \left(\frac{P_i}{P}\right)^{1/\gamma} \\
&\quad \times \int_0^t \left[\int_\xi^t \frac{P}{P_i}\, d\zeta \right] \left[\frac{P}{P_i}\right]^{1/\gamma - 2} \frac{d}{d\xi} \left[\frac{P}{P_i}\right] d\xi \qquad \text{(A4.1)}
\end{aligned}$$

$$\begin{aligned}
dq/dt &= C_p T_{core} \frac{d}{dt} [\rho_{core} \delta] \\
&= \frac{d}{dt} \left[\frac{P\delta}{\gamma - 1} \right] + P \frac{d\delta}{dt} \qquad \text{(A4.2)}
\end{aligned}$$

where P_i is the initial pressure of gas, α_0 is the thermal diffusivity at the initial temperature and pressure, and C_p is the constant pressure specific heat.

From mass conservation, the following equation is obtained [30]:

$$\frac{P_i (V_i + V_{cr})}{R\ T_i} = \frac{PV}{RT_{core}} + \rho_{core} A\delta + \frac{PV_{cr}}{RT_{cr}} \qquad (A4.3)$$

where the subscript $_i$ represents initial states, the subscript $_{core}$ represents states of the core temperature region, the subscript $_{cr}$ represents states in the piston head crevice, and A is the heat transfer area. Since the displacement thickness δ and the pressure P are given as a function of time from (A4.1) and the measured pressure record respectively, and the test chamber volume V and the heat transfer area A are given as a function of piston displacement, the piston displacement can be obtained as a function of time from (A4.3). By differentiating this piston displacement obtained from (A4.3) with respect to time, the piston speed and the piston acceleration can be also obtained.

The consideration of energy conservation gives the following relation [30]:

$$E_i - Q_{tbl} - Q_{cr} + W_p \qquad (A4.4)$$

$$= e_{core} \frac{P}{RT_{core}} (A\delta + V) + e_{cr} \frac{PV_{cr}}{RT_{cr}} - \frac{AP\delta}{\gamma - 1}$$

$$Q_{tbl} = \int_0^t \frac{dq}{d\zeta} A\ d\zeta = \frac{1}{\gamma - 1} \int_0^t \left[\frac{dP}{d\xi}\delta + \gamma \frac{d\delta}{d\xi} P \right] A\ d\xi$$

where Q_{tbl} is the heat transfer through the boundary layer, W_p is the work done by the piston, E_i is the initial internal energy of gas, and e is the specific internal energy. Since the test chamber volume V and the heat transfer area A has been obtained by (A3.3), the heat transfer through thermal boundary layer and that through the piston head crevice can be obtained from the above equation.

A.5 Interpretation of the Oil Pressure Oscillation

During the piston motion, the oil pressure oscillates at 500 Hz as shown earlier in Fig. 3.1. To check whether this oil pressure oscillation affect the piston motion, the piston speed and the piston acceleration calculated from the measured gas pressure using the laminar heat transfer model are superimposed with the measured oil pressure in Fig. A.5. Two independent measurements show the same frequencies, and the maximum peak of the oil pressure is in phase with the minimum peak of the piston deceleration as shown in the bottom graph of Fig. A.5. This indicates that the piston motion is affected by the oil pressure oscillation.

Since the peak-to-peak amplitude of the oil pressure oscillation, ΔP, is of the order of 1 MPa, the oil pressure area, A_p, is 6×10^{-3} m^3, and the piston mass, M_p, is around 1 Kg, the piston acceleration due to oil pressure oscillation is estimated by the following relation:

$$a = \Delta P \, A_p / M_p \qquad (A5.1)$$

where a is piston acceleration. The calculated piston acceleration is around 6 Km/sec^2, and this number is the same order as the peak-to-peak oscillation of the piston acceleration in the bottom graph of Fig. A.5.

When the oil pressure oscillation is assumed to follow a typical linear second-order vibrational equation [31] as in (A5.2), the natural angular frequency $\omega_n = 2\pi f$ and the damping ratio ζ are related as:

$$\frac{d^2P}{dt^2} + 2\zeta\omega_n \frac{dP}{dt} + \omega_n^2 P = fn(t) \qquad (A5.2)$$

$$\omega_d = \omega_n \sqrt{1-\zeta^2} \qquad (A5.3)$$

$$\ln(P_{peak,i}/P_{peak,i+1}) = 2\pi\zeta/\sqrt{1-\zeta^2} \qquad (A5.4)$$

where fn(t) is a function of time, ω_d is apparent angular frequency, and $P_{peak,i}$ is i-th maximum peak pressure. From the logarithmic decrement relation of (A5.4) the damping ration is found to be 5.7×10^{-2}, and from (A5.3) the natural angular frequency is found to be 3148 Hz.

An explanation of this oil pressure oscillation is that the oil acts as a spring in this high pressure situation. This oil spring was not included in the RCM dynamic simulation model derived in Appendix A.3, and this is why the piston speed from the RCM dynamic simulation does not show any oscillation while that from the heat transfer analysis shows oscillation as shown in the bottom graph of Fig. 3.13.

To check whether the above explanation is the right physics, a linearized order of magnitude analysis is carried out, in which the oil is modeled as a lumped spring, the piston as a mass, and the speed control orifice as a flow resistance. The schematic of the simple model used is shown in Fig. A.6 with the typical numbers used. The spring constants K_1 and K_2 are obtained from the isentropic bulk modulus of elasticity as follows:

$$E_s = -V \left(\frac{\partial P}{\partial V}\right)_s = -A_p(S-x) \frac{d(F/A_p)}{d[A_p(S-x)]} = \frac{(S-x)}{A_p} \frac{dF}{dx}$$

$$K_1 = \frac{dF}{dx} \sim \frac{E_s A_p}{S} \qquad \text{(A5.5)}$$

$$E_s = -A_r L \frac{d(F/A_r)}{d[A_p y]} = -\frac{L}{A_r} \frac{dF}{dy}$$

$$K_2 = -\frac{dF}{dy} \sim \frac{E_s A_r}{L} \qquad \text{(A5.6)}$$

where $E_s = 1.51 \times 10^9 N/m^2$ is the isentropic bulk modulus of elasticity of hydraulic oil, and S is the stroke. From the Newton's second law of motion, the relation for piston motion is given by:

$$M_p D^2 x = F_d - P_1 A_p \qquad \text{(A5.7)}$$

where M_p is piston mass, F_d is driving force, and D(.) is d(.)/dt as defined earlier in Appendix A.3. From continuity consideration, the relation between x and y is given by:

$$A_r y = A_p x \qquad (A5.8)$$

The linearized relation between P_1 and P_2 and between P_4 and P_a are obtained from Bernoulli equation as:

$$(P_1-P_2)A_p = \rho A_p(S-x)D^2x + K_1x$$

$$\sim \rho A_p S D^2x + K_1x \qquad (A5.9)$$

$$(P_4-P_a)A_r = \rho A_r L D^2y - K_2y \qquad (A5.10)$$

where K_1 and K_2 are spring constants of the hydraulic oil obtained by (A5.5) and (A5.6) respectively, and P_a is the atmospheric pressure. The linearized relation between P_2 and P_4 are also obtained as follows:

$$(P_2-P_4)A_o = \frac{\rho}{2}\left(\frac{A_p}{A_o}Dx\right)^2\left(\frac{1}{C_d^2}-1\right)A_o + \rho L_2 \frac{A_p}{A_o} D^2x$$

$$\sim \frac{\rho}{2}\left(\frac{A_p}{A_o}\right)^2\left(\frac{1}{C_d^2}-1\right)A_o u_p Dx + \rho L_2 \frac{A_p}{A_o} D^2x \qquad (A5.11)$$

where $C_d \sim 0.5$ is discharge coefficient of the speed control orifice. Combining (A5.7) through (A5.11) gives the final linearized governing equation of the form (A5.2) as follows:

$$\left[\frac{M_p}{A_p} + \frac{\rho L A_p}{A_r} + \frac{\rho L_2 A_p}{A_o} + \rho S\right] D^2x + \frac{\rho}{2} u_p \left(\frac{A_p}{A_o}\right)^2\left(\frac{1}{C_d^2}-1\right)Dx$$

$$+ \left[\frac{K_1}{A_p} - \frac{K_2 A_p}{A_r^2}\right]x = \frac{F_d}{A_p} - Pa \qquad (A5.12)$$

Comparison of (A5.12) with (A5.2) gives the relations for natural angular frequency ω_n and damping ratio ζ. When typical numbers given in Fig. A.6 are used for

these relations, oscillation frequency f and damping ration are obtained as 576 Hz and 0.092 respectively. These numbers are close to the measured numbers from oil pressure of 500 Hz and 0.057 respectively, considering the linearized order of magnitude analysis was used to obtain the oscillation frequency.

A.6 Detailed Description of Electronic Circuit

General layout of the timing circuit that synchronizes the start of the data acquisition and the opening of the solenoid valve is shown earlier in Fig. 2.10. In this section of Appendix, the detailed circuit diagrams of each component of the timing circuit are given in Fig. A.7 through Fig. A.11 except the commercially available DCI counter.

The TTL converter shown in Fig. A.7 converts a 120 VAC sinusoidal wave to an ±5 V sinusoidal wave using a series of resistors, then the LN 311 comparator converts this ±5 V sinusoidal wave to a TTL square wave. To send a firing signal to the logic circuit, the debounce switch is used as shown in Fig. A.8, which removes the contact oscillation of the mechanical switch. The logic circuit shown in Fig. A.9 consists of AND and OR gates, and it controls signals coming from various components of the timing circuit. The relay circuit shown in Fig. A.10 drives the solenoid valve when a RENABL signal from the logic circuit goes high, and the MOV 970-1 in the relay circuit protects the circuit from the electric spike when the solenoid is activated.

In Fig. A.11 is shown the external clock circuit. The LED should be on when the clock is reset using a reset switch before firing the RCM. When a CENABL signal goes high, the clock is activated and sends the TTL clock signal through a CLK port. The clock speed can be adjusted using DIP switches connected to pins 2 through 7 of the PXO-1000 chip. The pin settings and the corresponding clock speed are given in Table A.1.

Table A.1 DIP Switch Setting and Clock Speed

program pin setting		pin 7	0	0	0	0	1	1	1	1
		pin 6	0	0	1	1	0	0	1	1
pin		5	0	1	0	1	0	1	0	1
4	3	2								
0	0	0	1M	100K	10K	1K	100	10	1	0.1
0	0	1	100K	10K	1K	100	10	1	0.1	0.01
0	1	0	500K	50K	5K	500	50	5	0.5	0.05
0	1	1	333.3K	33.3K	3.3K	333.3	33.3	3.3	0.33	0.033
1	0	0	250K	25K	2.5K	250	25	2.5	0.25	0.025
1	0	1	200K	20K	2K	200	20	2	0.2	0.02
1	1	0	166.6K	16.6K	1.6K	166.6	16.6	1.66	0.16	0.016
1	1	1	83.3K	8.3K	833.3	83.3	8.3	0.83	0.083	0.0083

0 for on and 1 for off

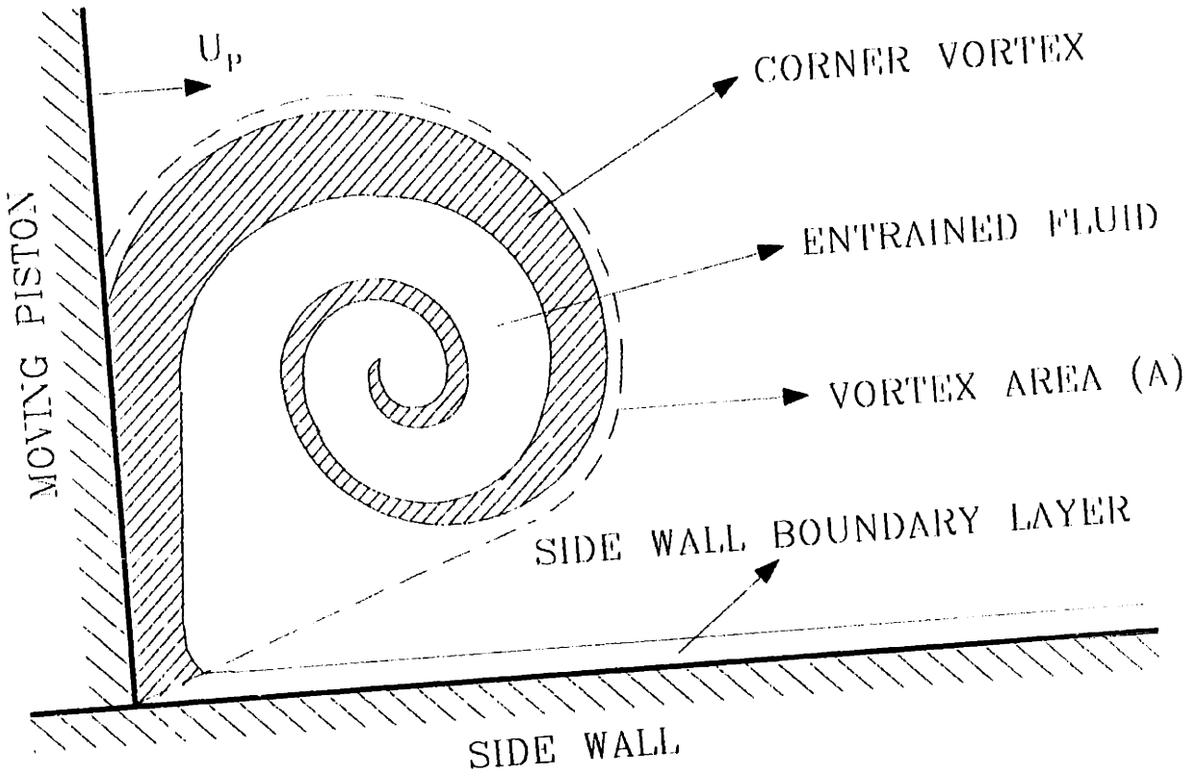

Figure A.1 Sketch of Corner Vortex

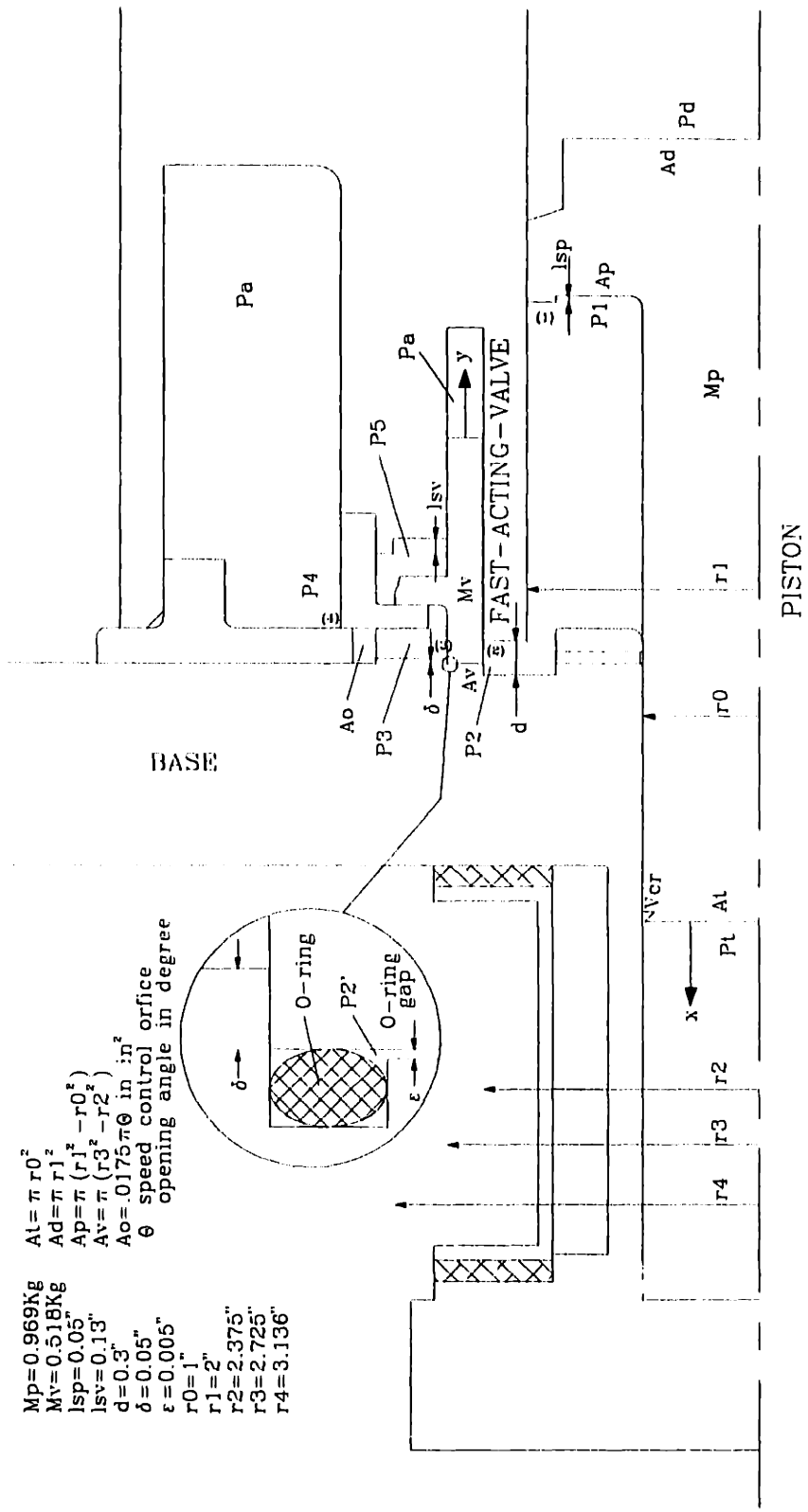

Figure A.2 RCM Dynamic Simulation and Important Dimensions

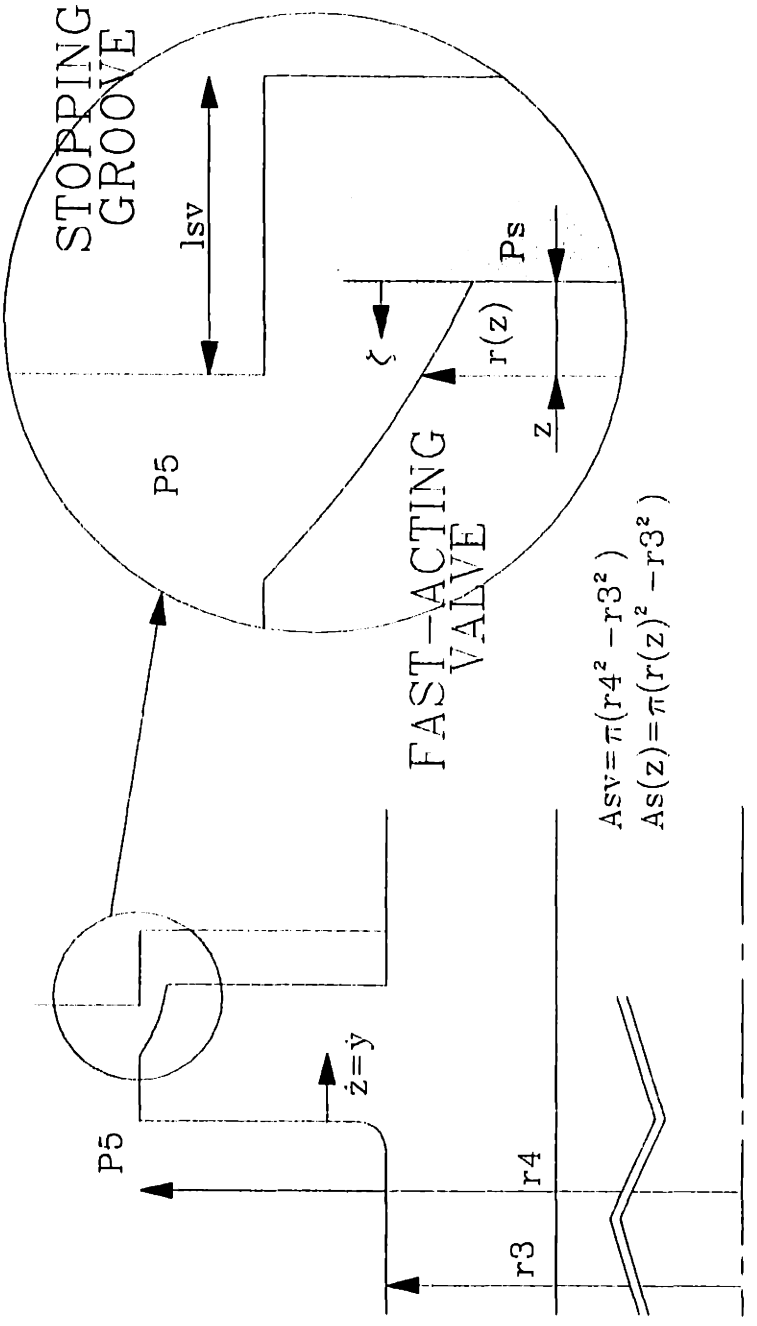

Figure A.3 Valve Stopping Pin Dynamics

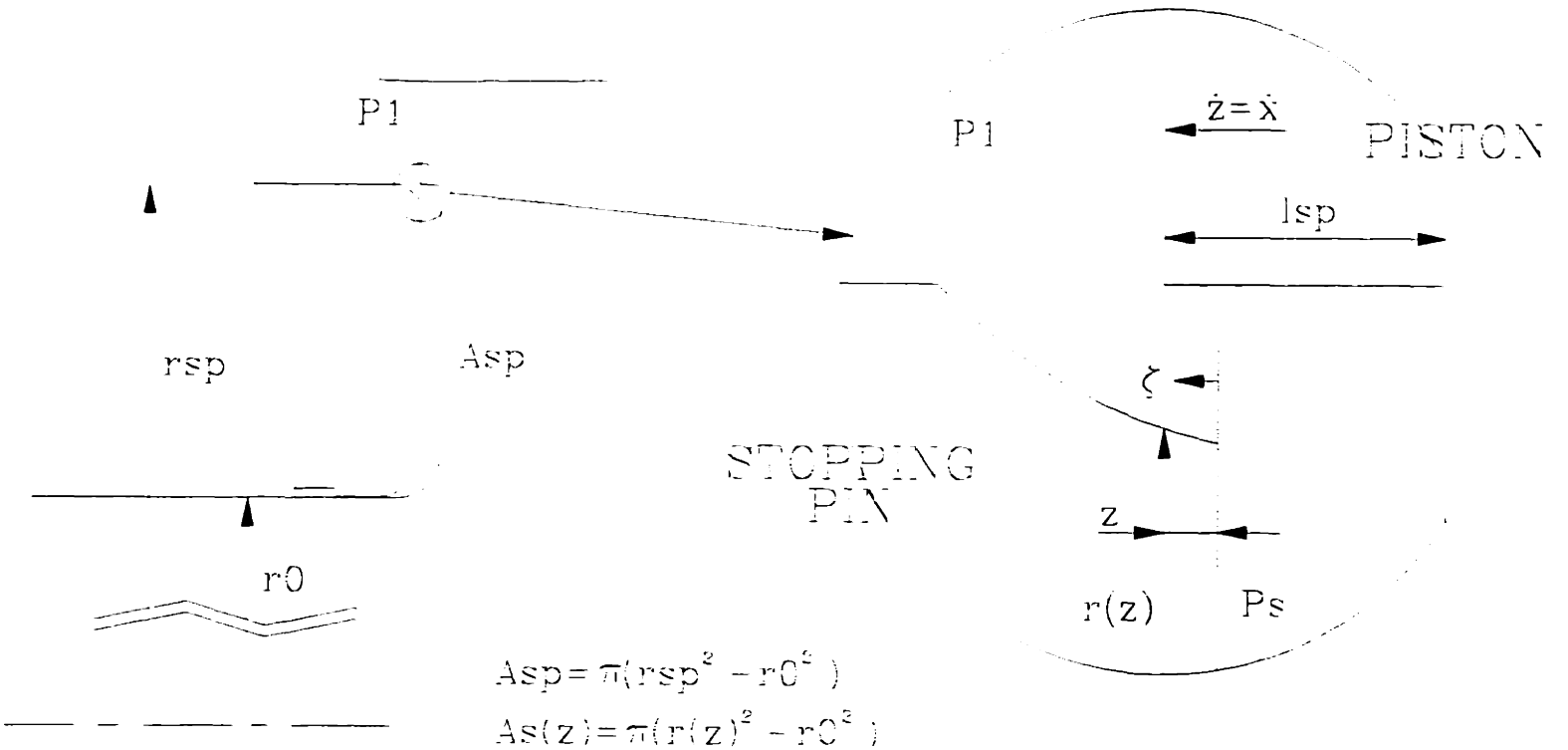

Figure A.4 Piston Stopping Pin Dynamics

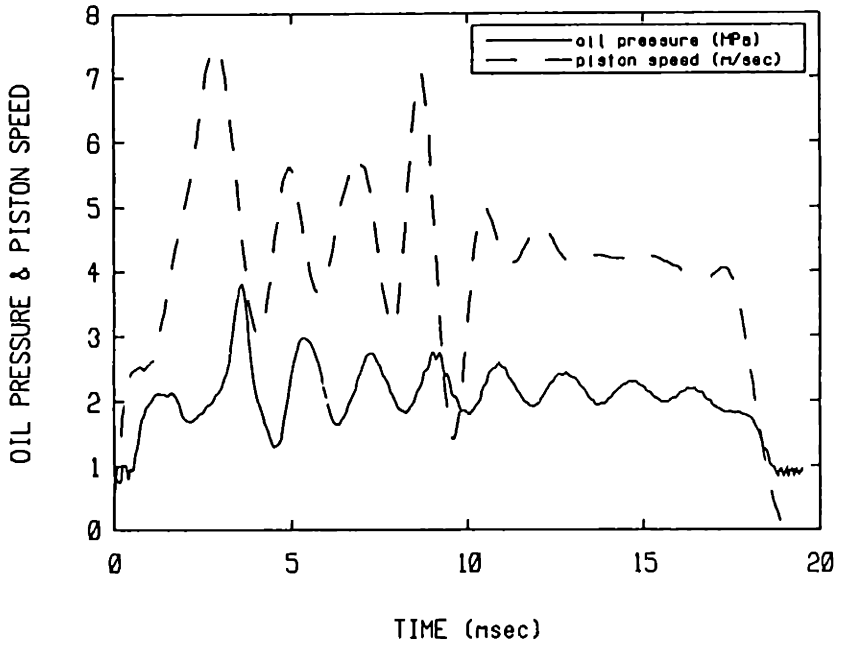

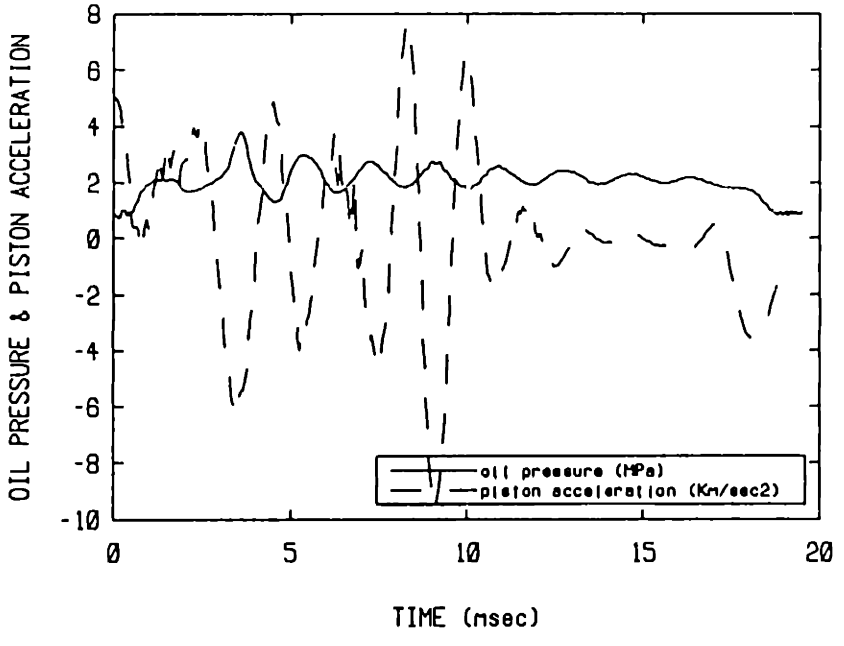

Figure A.5 Measured Oil Pressure and Piston Motion from Heat Transfer Analysis : Gas=N_2, P_i=720 torr, T_i=303 K, Driving Pressure=2.07 MPa, Stroke=7.84 cm, Clearance Height=0.6 cm, Speed Control Orifice Opening Area=6.81 cm^2, Piston Head with Crevice, Time 0 Shifted to Start of Compression

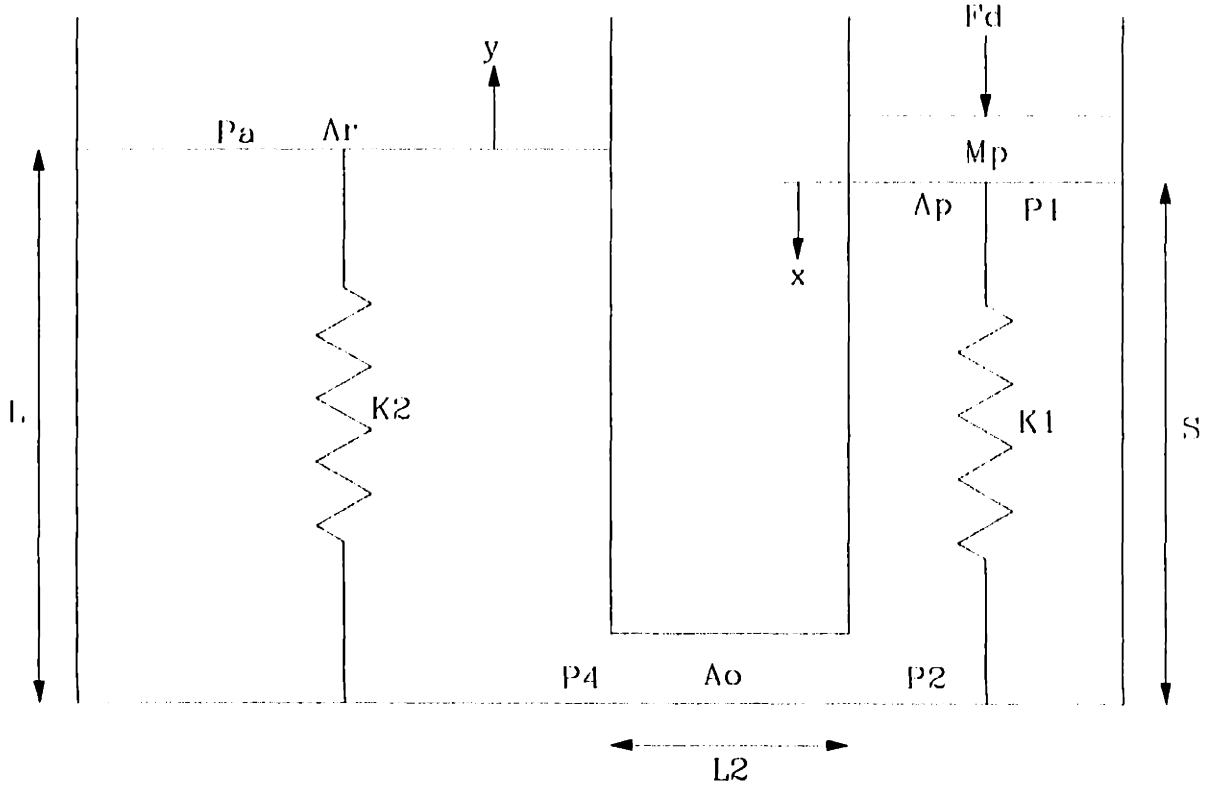

Figure A.6 Oil Pressure Oscillation Model : A_p=60.8 cm^2, A_r=269.4 cm^2, A_o=6.81 cm^2, L=10 cm, L_2=5 cm, S=10 cm, ρ=840 Kg/m^3, E_e=1.51 GN/m^2, K_1=91.8 MN/m, K_2=406.8 MN/m, C_d=0.5, M_p=1 Kg, u_p=5 m/sec

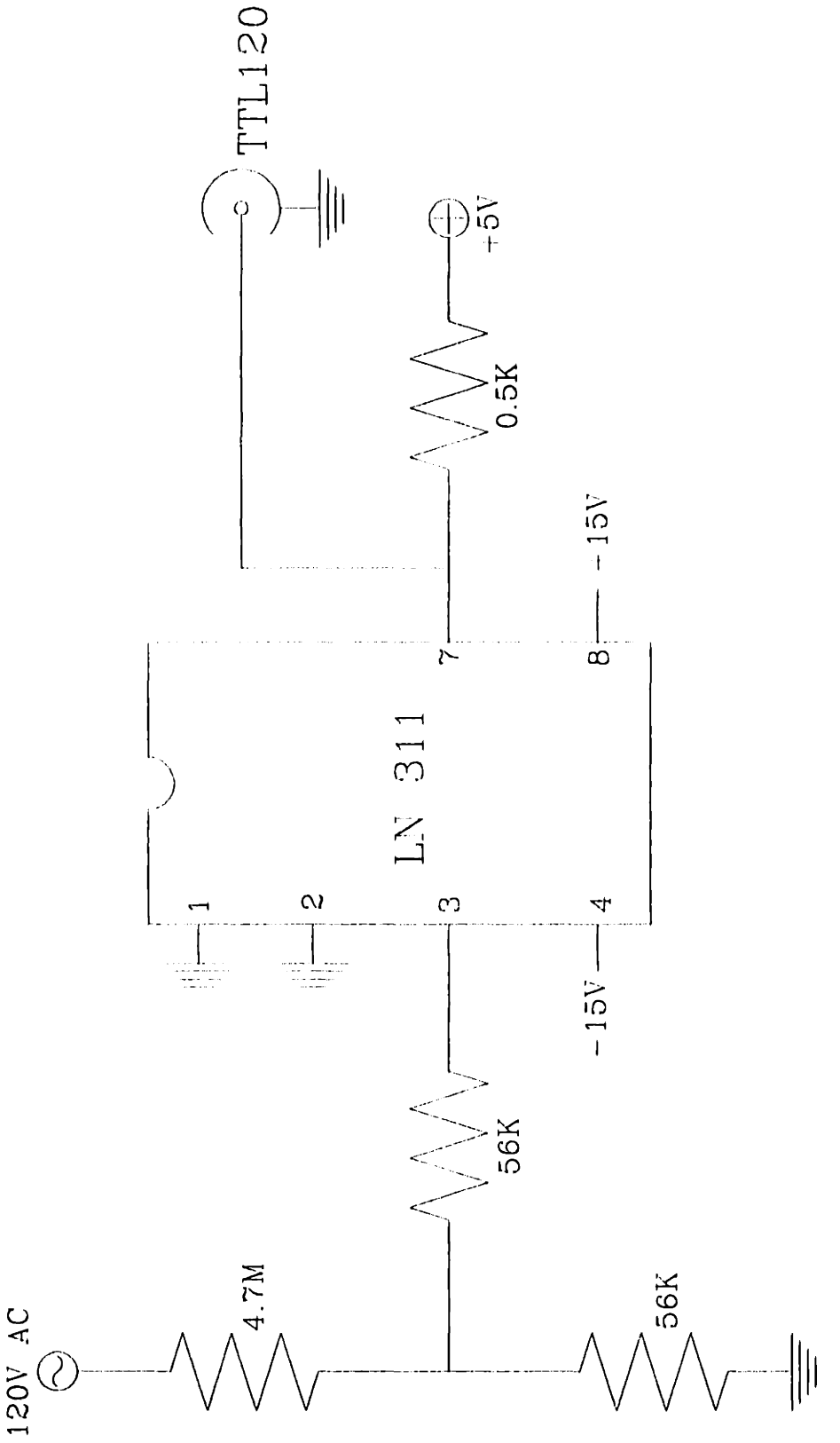

Figure A.7 Circuit Converting 120 VAC to TTL Square Wave

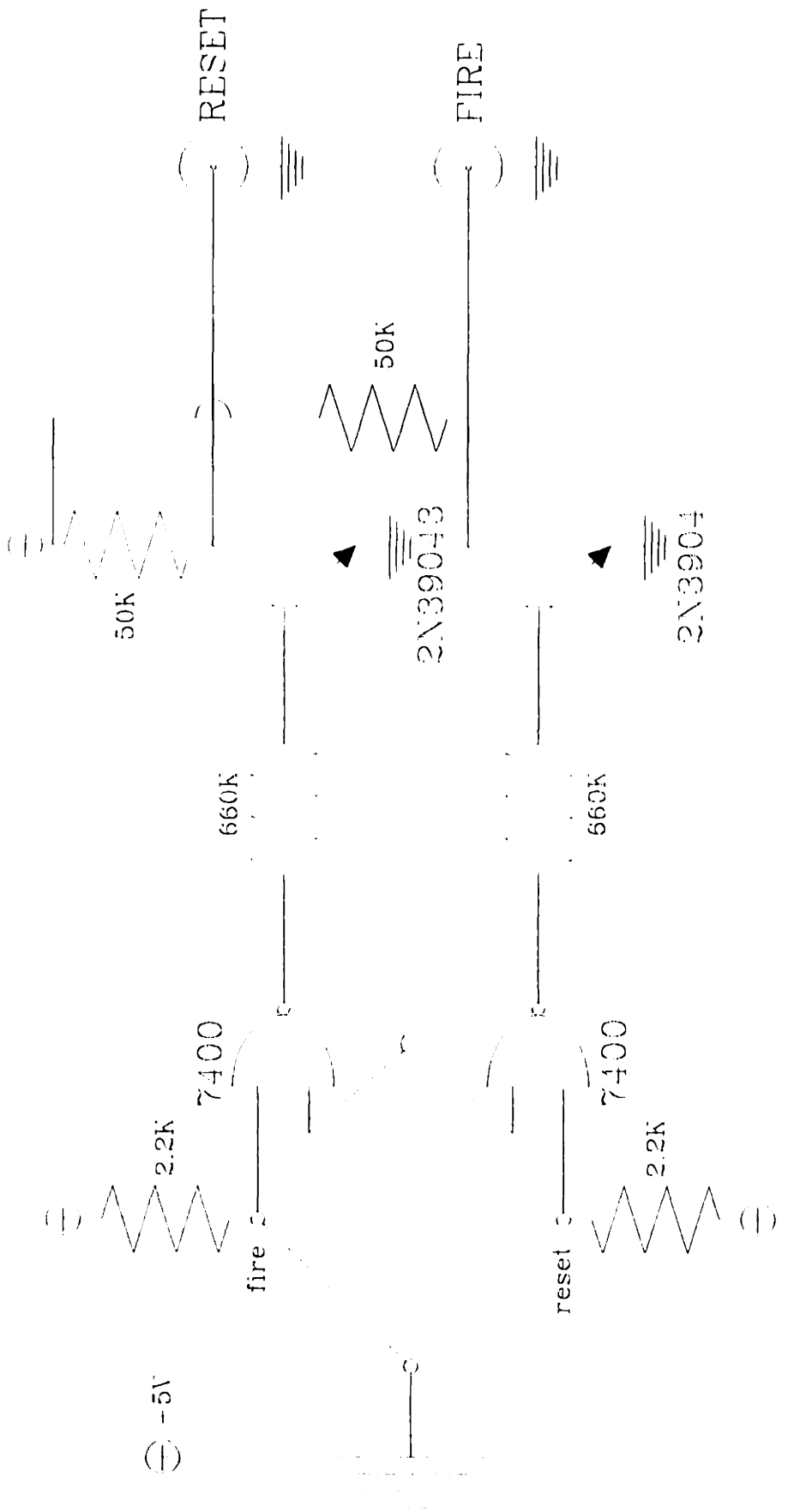

Figure A.8 Debounce Switch

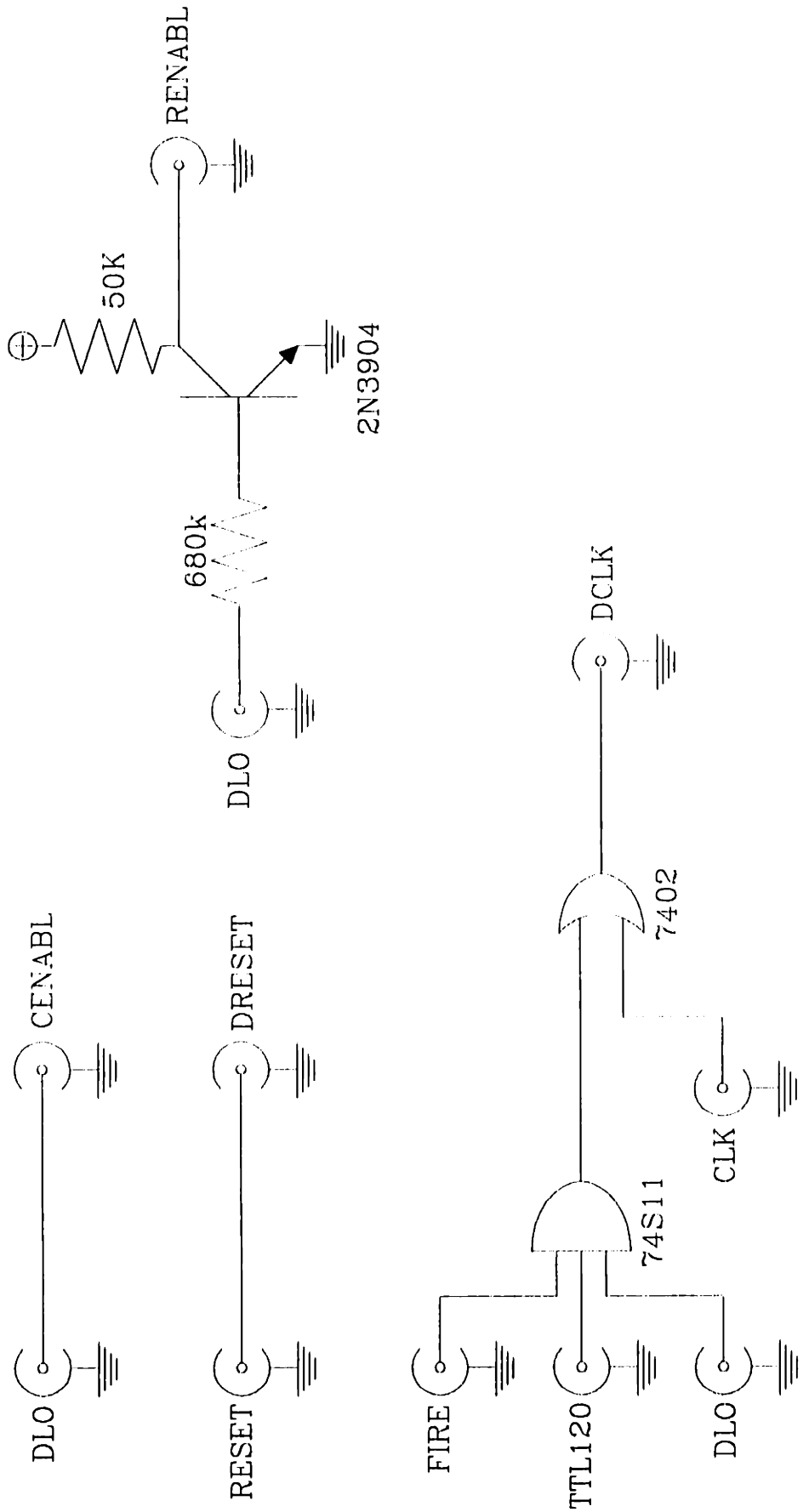

Figure A.9 Logic Circuit

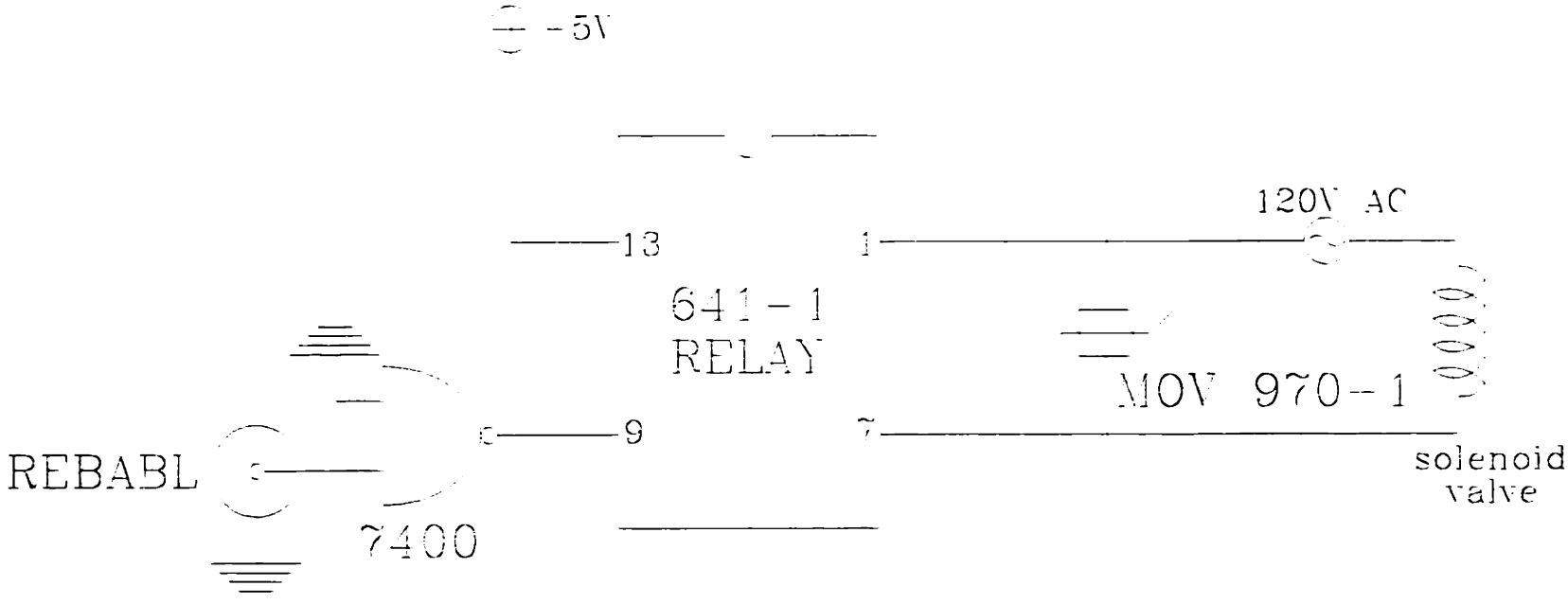

Figure A.10 Relay Circuit

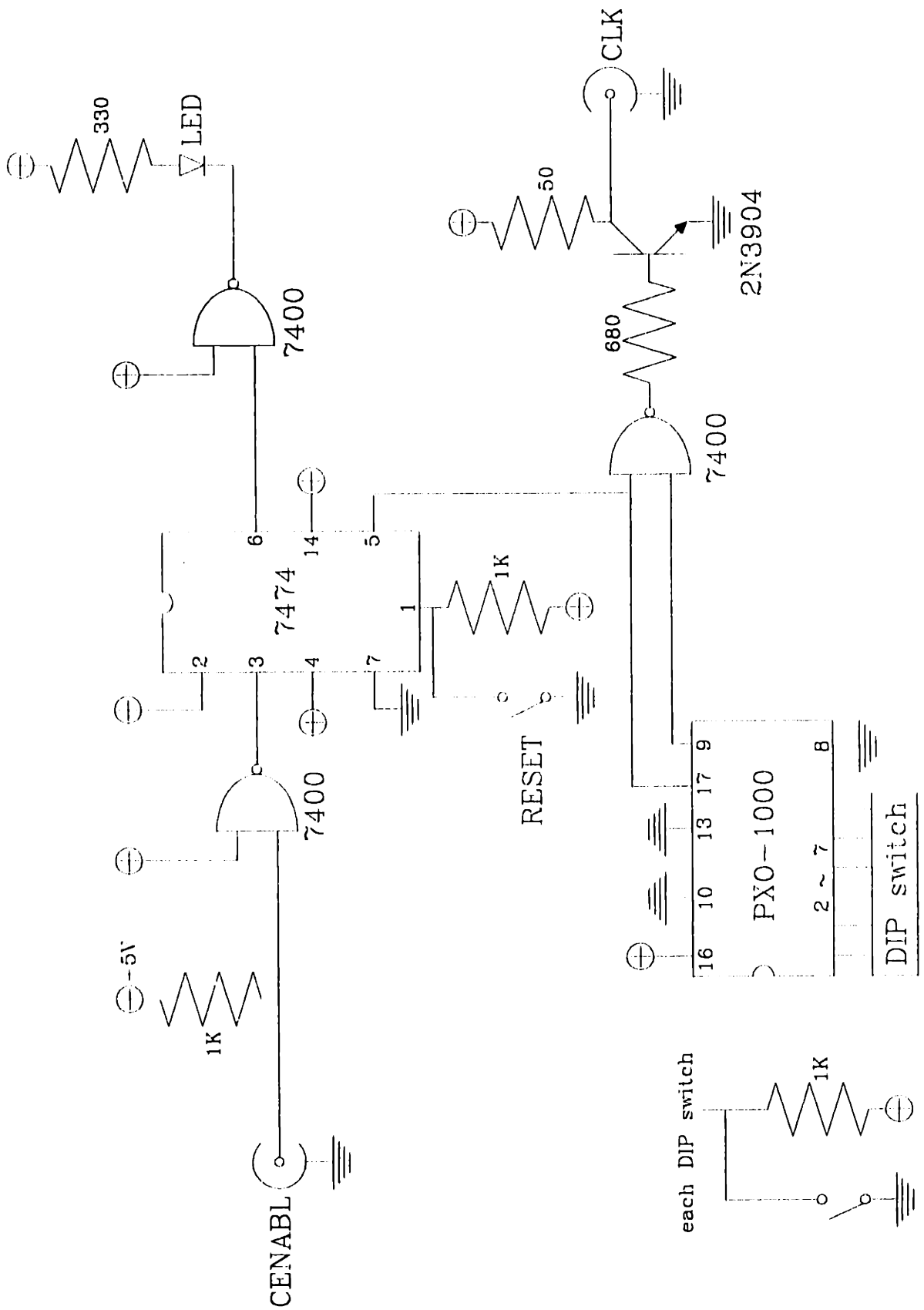

Figure A.11 External Clock Circuit